

INVESTIGATION OF MISSILES WITH STRAKE FINS AND REDUCTION OF
AERODYNAMIC CROSS COUPLING EFFECTS BY OPTIMIZATION

A THESIS SUBMITTED TO
THE GRADUATE SCHOOL OF NATURAL AND APPLIED SCIENCES
OF
MIDDLE EAST TECHNICAL UNIVERSITY

BY

ENGIN USTA

IN PARTIAL FULFILLMENT OF THE REQUIREMENTS
FOR
THE DEGREE OF MASTER OF SCIENCE
IN
AEROSPACE ENGINEERING

NOVEMBER 2015

Approval of the thesis

INVESTIGATION OF MISSILES WITH STRAKE FINS AND REDUCTION OF AERODYNAMIC CROSS COUPLING EFFECTS BY OPTIMIZATION

submitted by **ENGIN USTA** in partial fulfillment of the requirements for the degree of **Master of Science in Aerospace Engineering Department, Middle East Technical University** by,

Prof. Dr. Gülbin Dural
Dean, Graduate School of **Natural and Applied Sciences**

Prof. Dr. Ozan Tekinalp
Head of Department, **Aerospace Engineering**

Prof. Dr. İsmail Hakkı Tuncer
Supervisor, **Aerospace Engineering Dept., METU**

Examining Committee Members:

Assoc. Prof. Dr. Sinan Eyi
Aerospace Engineering Dept., METU

Prof. Dr. İsmail Hakkı Tuncer
Aerospace Engineering Dept., METU

Prof. Dr. Hüseyin Nafiz ALEMDAROĞLU
Department of Airframe and Powerplant Maintenance.,
Atılım Uni.

Assoc. Prof. Dr. M. Metin Yavuz
Mechanical Engineering Dept., METU

Asst. Prof. Dr. Harika Senem Kahveci
Aerospace Engineering Dept., METU

Date: 12/11/2015

I hereby declare that all the information in this document has been obtained and presented in accordance with academic rules and ethical conduct. I also declare that, as required by these rules and conduct, I have fully cited and referenced all material and results that are not original to this work.

Name, Last name : Engin USTA

Signature :

ABSTRACT

INVESTIGATION OF MISSILES WITH STRAKE FINS AND REDUCTION OF AERODYNAMIC CROSS COUPLING EFFECTS BY OPTIMIZATION

Usta, Engin
M.S., Department of Aerospace Engineering
Supervisor: Prof. Dr. İsmail Hakkı Tuncer

November 2015, 90 Pages

Missiles with very low aspect ratio fins (also called strakes) are generally difficult to model by using engineering level aerodynamic methods and linear theories break due to complex nature of the flow adjacent to the mutual interference of the body and fin. Since fast prediction methods cannot accurately model vortex development along and downstream of very low aspect ratio fins, they have limited success for application to missiles with strake fins. Moreover, there is limited number of CFD studies for investigating aerodynamics of very low aspect ratio fins. In this thesis, a generic test model is selected and CFD analyses are performed to estimate the normal force and center of pressure of the strake unit with varying angle of attack at supersonic Mach numbers for two different roll orientations. The CFD results are compared with fast prediction methods (Missile DATCOM and White's method) and wind tunnel data. By the comparative validation study, CFD analyses are proven to be reliable and robust for application to missiles with very low aspect ratio fins. In

addition, a limited goal CFD based optimization study to design strake planform geometry is performed for alleviating the cross coupling effect on the pitching moment from sideslip angle while keeping static margin in a constant range. The geometrical parameters varying during the optimization problem consist of the leading edge location, chord length and span length of the strake planform. Since the configuration is monotype consisting of a body with strake and tail, automatic meshing scheme is developed and the whole processes from grid generation to CFD solutions are fully automated. For optimization problem, firstly a gradient based method is tested and then a stochastic optimization method is employed to guarantee global optimization instead of finding local minimum. Particle Swarm Optimization Method (PSO) is selected as a suitable population based stochastic optimization method for this study. The gradient based optimization method namely the steepest descent with line search is also applied for the same problem to investigate the applicability of gradient based optimization methods. It was observed that at the end of the PSO iterations, a small chord, short span strake comes out. However, it was also observed that the gradient solution ends with a short span, long chord strake geometry. Apparently, the gradient based optimization method is trapped in the local minimum. By the PSO optimization study, the cross coupling on the pitching moment from sideslip is decreased to one third of the initial value from baseline to optimum configuration while static margin is kept in a particular range.

Keywords: Very Low Aspect Ratio Fins, Particle Swarm Optimization, Strake Planform Optimization, Computational Fluid Dynamics, Engineering Level Aerodynamic Prediction Methods

ÖZ

ÇOK KÜÇÜK KANAT AÇIKLIK ORANINA SAHİP SABİT KANATLI FÜZELERİN İNCELENMESİ VE AERODİNAMİK ÇARPRAZ ETKİLEŞİM ETKİLERİNİN OPTİMİZASYON KULLANILARAK EN AZA İNDİRİLMESİ

Usta, Engin

Yüksek Lisans , Havacılık ve Uzay Mühendisliği Bölümü
Tez Yöneticisi: Prof. Dr. İsmail Hakkı Tuncer

Kasım 2015, 90 Pages

Çok küçük kanat açıklık oranına sahip kanatçıklara sahip füzeleri mühendislik seviyesi yöntemlerle modellemek zordur. Çünkü akışın karmaşık yapısından dolayı doğrusal teoriler yeterli olmamaktadır. Çok küçük kanat açıklık oranına sahip kanat kenarlarında oluşan vorteksler ile devamında akış yönünde oluşan vortekslerin kontrol yüzeyleri üzerindeki etkisini modellemede hızlı tahmin yöntemleri yetersiz kalmaktadır. Çok küçük kanat açıklık oranına sahip füzeler için literatürde sınırlı sayıda HAD (Hesaplama Akışkanlar Dinamiği) çalışmasının bulunduğu görülmüştür. Bu tezde çok küçük kanat açıklık oranına sahip jenerik bir denek taşı füze için süpersonik hızlarda farklı yuvarlanma açılarında HAD analizleri gerçekleştirilmiştir. Bu analizlerde normal kuvvet ve basınç merkezi değerleri elde edilmiştir. CFD sonuçları Missile DATCOM ve White yönteminden elde edilen sonuçlar ile karşılaştırılmış olup, çok küçük kanat açıklık oranına sahip problemlerde

CFD metodunun uygulanabilir olduđu doğrulanmıştır Ayrıca statik marjini sabit bir aralıkta tutmaya çalışarak yunuslama momenti üzerinde yanal sapma açısından kaynaklanan çarpaz etkileşim etkilerini azaltmak için kanatçık geometrisi tasarımına yönelik CFD tabanlı optimizasyon çalışması gerçekleştirilmiştir. Çok küçük kanat açıklık oranına sahip kanatçık tasarımında veter uzunluğu, kanat açıklığı ve gövde üzerinde hücum kenarı yerleşimi optimizasyon probleminin girdi geometrik parametrelerini oluşturmaktadır. Bu çalışmadaki grid oluşturmada Hesaplamalı Akışkanlar çözümüne kadar olan süreç tamamen otomatik hale getirilmiştir. Kanatçık geometrisinin değiştirilerek performans parametrelerinin optimize edilmesi çalışmasında öncelikle gradyen tabanlı bir optimizasyon yöntemi denenmiş olup, ayrıca global çözüme ulaşmak için stokastik bir optimizasyon yöntemi de kullanılmıştır. Parçacık Sürü Optimizasyonu (PSO) yöntemi popülasyon tabanlı verimli bir stokastik optimizasyon yöntemi olup bu çalışma için uygun bulunmuştur. Gradyen tabanlı bir optimizasyon yöntemi olan hat arama ile dik iniş yöntemi de aynı problem için uygulanmıştır. PSO yöntemi sonunda kısa bir veter uzunluğu ile birlikte düşük bir kanat açıklığı elde edildiği görülmüştür. Ancak gradyen tabanlı optimizasyon sonucunda düşük kanat açıklığı yanında uzun bir veter uzunluğu elde edilmiştir. Aslında gradyen tabanlı çözüm, tuzak bir sonuçta takılı kalmıştır. Sonuç olarak, PSO çalışması sonunda statik marjin belirli bir aralıkta tutulurken yunuslama momenti üzerinde yanal sapma açısından kaynaklanan çarpaz etkileşim etkisi başlangıç noktasının üçte birine düşürülmüştür.

Anahtar Kelimeler: Çok Küçük Açıklık Oranına Sahip Kanatçıklar, Parçacık Sürü Optimizasyon Yöntemi, Çok Küçük Açıklık Oranına Sahip Kanatçıkların Boyutlarının Optimizasyonu, Hesaplamalı Akışkanlar Dinamiği, Mühendislik Seviyesi Aerodinamik Kestirim Araçları

To My Family

ACKNOWLEDGEMENTS

I wish to express my deep gratitude to my supervisor Prof. Dr. İsmail Hakkı Tuncer for his advice, guidance, criticism and encouragement throughout the thesis.

I would like to thank my manager Mr. Ali Akgül for guidance and support during this thesis. I also would like to thank all of my colleagues in Aerodynamics Division of ROKETSAN for their help and motivation during the thesis.

I also wish to express my sincere thanks to my colleagues Oral Akman, Erkut Başkut and Emrah Gülay for sharing their expertise and criticism.

I am very thankful to my wife Mrs. Yeliz Usta, and my parents Mr. Kemal Usta, Mrs. Melihat Usta for their help and motivation. Without them, this thesis would not be completed.

I want to express my best wishes to Mr. Kıvanç Arslan and Mr. Ertan Demirel for their valuable friendship and support during this study.

TABLE OF CONTENTS

ABSTRACT	5
ÖZ	7
ACKNOWLEDGEMENTS	10
TABLE OF CONTENTS	11
LIST OF FIGURES	13
LIST OF TABLES	17
INTRODUCTION	1
1.1 Missiles with very low aspect ratio fins	2
1.2 Aerodynamic Loads Acting on the Missile.....	4
1.3 Aerodynamic Performance Parameters	5
1.3.1 Static Stability	5
1.3.2 Aerodynamic Trim and Control Effectiveness	6
1.3.3 Trim Load Factor	7
1.3.4 Pitching Moment due to Sideslip Angle and Vortex Breakdown	7
1.4 Considerations of Missile Design Analysis	10
1.5 Literature Survey.....	10
1.6 Aim of the Thesis	14
METHODOLOGY	17
2.1 The Aerodynamic Estimation Tools	17
2.1.1 The CFD Solver	17
2.1.1.1 Reynolds Averaged Navier Stokes Equations.....	18
2.1.1.2 Turbulence Model Selection	20
2.1.1.3 Development of an Automatic Grid Generation Tool.....	21

2.1.2	The Missile DATCOM.....	23
2.1.3	The White’s Method.....	24
2.2	Optimization Methods.....	24
2.2.1	Particle Swarm Optimization Method.....	24
2.2.1.1	The Details of the PSO Algorithm	25
2.2.1.2	An Application of the PSO algorithm	28
2.2.2	Gradient Based Optimization	31
RESULTS AND DISCUSSION.....		33
3.1	Aerodynamic Validation Study with D57 Missile Configuration.....	33
3.1.1	Computational Grid.....	35
3.1.2	Comparison of the Aerodynamic Loads.....	37
3.2	Optimization Studies	47
3.2.1	Aerodynamic Performance Optimization Problem	47
3.2.2	Gradient based Optimization.....	50
3.2.2.1	Variation of the Objective Function in Gradient Based Optimization.....	50
3.2.2.2	Variation of the Configuration in Gradient Based Optimization Iterations	52
3.2.3	Particle Swarm Optimization	54
3.2.3.1	Variation of the Objective Function in PSO Iterations	55
3.2.3.2	Variation of the Configuration in PSO Iterations.....	55
3.2.3.3	Variation of the Performance Parameters in PSO Iterations.....	59
3.2.4	Comparison of the PSO with Gradient Optimization.....	61
3.2.5	Comparison of the Optimum and Baseline Configurations	62
3.2.6	Comparison of the Optimum and a Classical Configuration	74
CONCLUSION.....		77
REFERENCES		81
APPENDICES		
A. GRADIENT OPTIMIZATION CALCULATIONS		85
B. THE PSO OPTIMIZATION STUDY BY USING MISSILE DATCOM		87

LIST OF FIGURES

FIGURES

Figure 1.1 Raytheon RIM-161 Standard SM-3	3
Figure 1.2 MBDA MICA	3
Figure 1.3 Astra.....	3
Figure 1.4 IRIS-T SL	3
Figure 1.5 RIM-162 Evolved Sea Sparrow Missile.....	3
Figure 1.6 AGM-78 Standart arm	4
Figure 1.7 Aerodynamic Moment and Forces Acting On the missile.....	4
Figure 1.8 Static stability and pitching moment with angle of attack curve relation...	6
Figure 1.9 Tail control deflection for aerodynamic trim condition	7
Figure 1.10 Vortex breakdown sketch for delta wings	8
Figure 1.11 Cross sectional aerodynamic flow patterns	9
Figure 1.12 Vortex shedding from the strake panels	9
Figure 2.1 Density based solution methodology	18
Figure 2.2 Mesh generation regions for the body-strake-tail configuration	21
Figure 2.3 y^+ Distribution over wall surfaces.....	22
Figure 2.4 Simulation of the individual behavior in motion of flocks of birds	25
Figure 2.5 The Particle Swarm Optimization Method New Position Calculation.....	27
Figure 2.6 Flowchart for the Optimization of Strake Planform Geometry with Particle Swarm Optimization	27
Figure 2.7 Contour plot of “Eggholder” function	28
Figure 2.8 Number of iterations and number of function calls during iterations by..	29
Figure 2.9 The movement of the particles in search space during PSO iterations (Former iterations are shown by blue-square and latter ones by pink-diamond.).....	30
Figure 3.1 Geometric Details of the test case Missile Body and placement of D57 Strake.....	35
Figure 3.2 Geometric Details of D57 Strake Panels	35

Figure 3.3 A detailed view of Surface and Volume Grid.....	35
Figure 3.4 Boundary Conditions and Detailed View of the Strake Panel Grid	36
Figure 3.5 The pressure contours slices along the body alone and body-(D57) strake configuration	38
Figure 3.6 Normal Force coefficient of the Strake Unit (D57) with Angle of Attack (Mach=2.01, $\phi=0^\circ$)	39
Figure 3.7 Center of Pressure of the Strake Unit (D57) with angle of attack (Mach=2.01, $\phi=0^\circ$)	39
Figure 3.8 Normal Force coefficient of the Strake Unit (D57) with Angle of Attack (Mach=2.8, $\phi=0^\circ$).....	40
Figure 3.9 Center of Pressure of the Strake Unit (D57) with angle of attack (Mach=2.8, $\phi=0^\circ$).....	40
Figure 3.10 Normal Force coefficient of the Strake Unit (D57) with Angle of Attack (Mach=3.98, $\phi=0^\circ$).....	41
Figure 3.11 Center of Pressure of the Strake Unit (D57) with angle of attack (Mach=3.98, $\phi=0^\circ$).....	41
Figure 3.12 Normal Force coefficient of the Strake Unit (D57) with Angle of Attack (Mach=2.01, $\phi=45^\circ$).....	42
Figure 3.13 Center of Pressure of the Strake Unit (D57) with angle of attack (Mach=2.01, $\phi=45^\circ$).....	42
Figure 3.14 Normal Force Coefficient of the Strake Unit (D57) with Angle of Attack (Mach=2.8, $\phi=45^\circ$).....	43
Figure 3.15 Center of Pressure of the Strake Unit (D57) with angle of attack (Mach=2.8, $\phi=45^\circ$).....	43
Figure 3.16 Normal Force Coefficient of the Strake Unit (D57) with angle of attack (Mach=3.98, $\phi=45^\circ$).....	44
Figure 3.17 Center of Pressure of the Strake Unit (D57) with angle of attack (Mach=3.98, $\phi=45^\circ$).....	44
Figure 3.18 The breakdown of the Interference and Component Normal Forces.....	46
Figure 3.19 Strake planform and location parameters (+ view).....	48

Figure 3.20 Baseline missile geometry (+ view)	50
Figure 3.21 Variation of the objective function during line search in iteration 1	51
Figure 3.22 Variation of the objective function during line search in iteration 2	51
Figure 3.23 Variation of geometrical parameters during line search in iteration1 ...	53
Figure 3.24 Variation of geometrical parameters during line search in iteration 2 ...	53
Figure 3.25 The optimum strake planform geometry and placement obtained by gradient optimization (+ view).....	54
Figure 3.26 Objective function during PSO iterations.....	55
Figure 3.27 Variation of leading edge location of the strake during PSO iterations .	57
Figure 3.28 Variation of the chord length of the strake during PSO iterations	58
Figure 3.29 Variation of span length of the strake during PSO iterations	58
Figure 3.30 Variation of the static margin of the current configuration during PSO iterations.....	59
Figure 3.31 Variation of the load factor of the current configuration during PSO iterations.....	60
Figure 3.32 Variation of the pitching moment differential with sideslip angle of the current configuration during PSO iterations	60
Figure 3.33 Optimum missile strake geometry (+ view)	62
Figure 3.34 Comparison of the optimum and baseline missile body-strake geometries (isometric view)	62
Figure 3.35 The change of the pitching moment coefficient with sideslip angle for the optimum and baseline missile configurations	63
Figure 3.36 The change of the normal force coefficient with sideslip angle for the optimum and baseline missile configurations	63
Figure 3.37 The change of the static margin with sideslip angle for the optimum and baseline missile configurations	64
Figure 3.38 The change of the panel normal force of the tail with sideslip angle for the optimum and baseline missile configurations	64
Figure 3.39 The pressure distribution over the baseline missile configuration at Mach 2.01, angle of attack 8° , sideslip angle 10° (45° rotated view).....	66

Figure 3.40 The pressure distribution over the baseline missile configuration at Mach 2.01, angle of attack 8° , sideslip angle 10° (side view).....	66
Figure 3.41 The pressure distribution over the optimum missile configuration at Mach 2.01, angle of attack 8° , sideslip angle 10° (45° rotated view).....	67
Figure 3.42 The pressure distribution over the optimum missile configuration at Mach 2.01, angle of attack 8° , sideslip angle 10° (side view).....	67
Figure 3.43 The Mach Number Contour Around the Baseline Missile Configuration at Mach 2.01, angle of attack 8° , sideslip angle 10° (side view).....	68
Figure 3.44 The Mach Number Contour Around the Optimum Missile Configuration at Mach 2.01, angle of attack 8° , sideslip angle 10° (side view).....	69
Figure 3.45 The velocity vector plots on slices along the x-axis of the optimum configuration at Mach 2.01, angle of attack 8° , sideslip angle 10°	70
Figure 3.46 The velocity vector plots on slices along the x-axis of the baseline configuration at Mach 2.01, angle of attack 8° , sideslip angle 10°	71
Figure 3.47 The pressure contours and streamlines on slices along the x-axis of the optimum configuration at Mach 2.01, angle of attack 8° , sideslip angle 10°	72
Figure 3.48 The pressure contours and streamlines on slices along the x-axis of the baseline configuration at Mach 2.01, angle of attack 8° , sideslip angle 10°	73
Figure 3.49 The change of the static margin with sideslip angle for the optimum and high aspect ratio missile configurations having same planform area.....	75
Figure 3.50 The change of the axial force coefficient with sideslip angle for the optimum and high aspect ratio missile configurations having same planform area ..	75
Figure 3.51 The change of the rolling moment coefficient with sideslip angle for the optimum and high aspect ratio missile configurations having same planform area ..	76
Figure B.1 The change of the objective function during DATCOM PSO iterations .	87
Figure B.2 Variation of the leading edge location of the strake during DATCOM inside PSO iterations	89
Figure B.3 Variation of the chord length of the strake during DATCOM inside PSO iterations	90
Figure B.4 Variation of the span length of the strake during DATCOM inside PSO iterations	90

LIST OF TABLES

TABLES

Table 3.1 The flow properties for D57 test case	34
Table 3.2 The flight conditions for D57 test case	37
Table 3.3 The limits of geometrical parameters.....	48
Table 3.4 The strake planform geometry and placement on the body during gradient based optimization iterations (+ view).....	52
Table 3.5 The strake planform geometry and placement on the body during PSO optimization iterations (+ view).....	56
Table 3.6 The comparison of the geometric parameters of the baseline, optimum and gradient solutions	61
Table 3.7 The comparison of the aerodynamic performance of the baseline, optimum and gradient solutions	61
Table A.1 The Gradient Vector Calculation for Iteration 1 of the Optimization.....	85
Table A.2 The Gradient Vector Calculation for Iteration 2 of the Optimization.....	85
Table A.3 The Gradient Vector Calculation for Iteration 3 of Optimization.....	86
Table A.4 The Gradient Vector Calculation for Iteration 4 of the Optimization.....	86
Table B.1 The comparison of the geometric parameters of the optimum configurations obtained by PSO using CFD and PSO using Missile DATCOM 2009	88
Table B.2 The comparison of the aerodynamic parameters obtained by CFD and Missile DATCOM 2009 for the MDBEST configuration	88
Table B.3 The comparison of the aerodynamic parameters of the MDBEST and CBEST configurations by CFD analysis	89

CHAPTER 1

INTRODUCTION

Very low aspect ratio missile configurations are preferred for their compact structures in span constrained missile applications with storage requirements. In addition, they are also used as cableways removing the extra need for special cable ways in some applications. Missiles having very low aspect ratio fins also have several distinct aerodynamic features. These include high lift and maneuverability compared to tail only configurations, low rolling moment compared to the high aspect ratio wings, and small center of pressure shift with varying angle of attack [1]. Moreover, interference lift produced due to body-fin interactions is large for missile-strake configurations, since they produce an important amount of the lift as vortex lift due to vortices shed along the long wingtip edges [2].

Since linear theories usually break and fail to estimate mutual interference adjacent to the long line along the strake body junction, fast prediction tools are not robust for estimating aerodynamics of the missiles having a strake [2]. The detailed analyses and a comparative validation study investigating aerodynamic capabilities of fast prediction methods White's method and DATCOM compared with CFD solutions for missiles having strakes can be found in Chapter 3.

Aerodynamic design optimization requires exploring a huge design space. However, for the problems with limited usage of fast prediction tools, the computational methods with small design space must be explored with few number of design parameters. The design space for Computational Fluid Dynamics optimization study needs to be small due to high computational demand. In the optimization study, for reaching solution faster, in a limited time, parallel function evaluations (that is

meshing multiple configurations, and running multiple CFD runs for our case) at the same time is required.

For optimization of performance parameters with geometrical parameters, a gradient based method is tested and a stochastic optimization method is used to assure global optimization instead of finding local solution. The steepest descent used in this study is a gradient based method. The Particle Swarm optimization method and the Steepest Descent with line search are used as optimization methods. PSO is a population based heuristic optimization method. Starting with random solution, the generations are updated at each step. The potential solutions called particles follow the current best solution and travel through search space as a swarm of particles. Since it allows multiple concurrent function evaluations during iterations, it fits our needs of meshing multiple configurations at the same time and having CFD calculations run in parallel. The details of the Particle Swarm Optimization Method are explained in Chapter 2.

After investigating various engineering level methods (used interchangeably with fast prediction methods) and performing computational study for solving body-strake aerodynamics, using CFD tools, an optimization study to alleviate pitch moment coupling on sideslip angle is performed while trying to keep static margin constant as a controlling parameter. The results of the optimization study can be found in Chapter 3.

1.1 Missiles with very low aspect ratio fins

Some of the missiles having very low aspect ratio fins are presented in the figures below. They range from ballistic intercept to short/medium range air-to-air, surface-to-air missiles, and even air-to-surface anti-radiation missiles. For example short range air to air missiles have strict space limitations and for this reason strake fins are employed [3].



Figure 1.1 Raytheon RIM-161 Standard SM-3 [4]



Figure 1.2 MBDA MICA [5]



Figure 1.3 Astra [6]



Figure 1.4 IRIS-T SL [7]



Figure 1.5 RIM-162 Evolved Sea Sparrow Missile [8]



Figure 1.6 AGM-78 Standart ARM [9]

As seen from the figures above, the strake fins are low or very low aspect ratio stationary fins having small span compared to the chord length. Commonly, strake fins can be placed over the nose or center body of the missile.

1.2 Aerodynamic Loads Acting on the Missile

On a missile in a six degree of freedom (6DOF) flight, three forces and moments act over the missile as shown in the figure below.

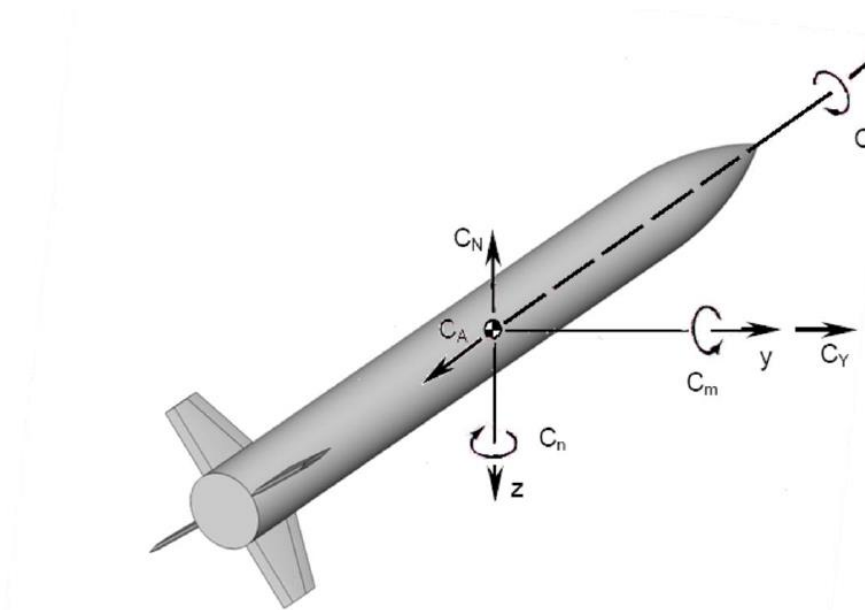


Figure 1.7 Aerodynamic Moment and Forces Acting On the missile [10]

In this paper, the reference length is taken as the missile diameter and reference area is the missile area.

The non-dimensional force coefficients are obtained by dividing force with the dynamic pressure (q) times reference area (S_{ref}). Moments are additionally divided by reference length (L_{ref}) to obtain moment coefficients.

$$C_{Force} = \frac{Force}{q \cdot S_{ref}} \quad (1.1)$$

$$C_{Moment} = \frac{Moment}{q \cdot S_{ref} \cdot L_{ref}} \quad (1.2)$$

The basic forces acting on the missile are normal force, axial force and side force as shown in Figure 1.7. The basic moments consist of the pitching moment, yawing moment and rolling moment.

1.3 Aerodynamic Performance Parameters

There are certain aerodynamic performance parameters to assess the missile aerodynamics in terms of stability and maneuverability. Some of them are listed below:

- Static Margin
- Control Effectiveness
- Trim Load Factor

1.3.1 Static Stability

A missile is aerodynamically stable if it has tendency to move back into equilibrium when perturbed. Static stability of the missile is measured by the slope of the pitching moment vs. angle of attack curve. The static stability condition is as follows:

$$C_{m_\alpha} < 0 \quad (1.3)$$

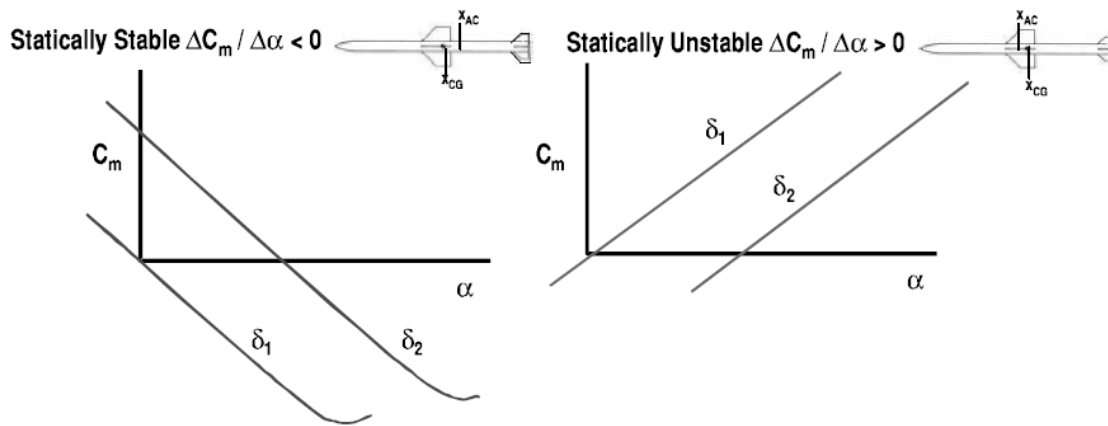


Figure 1.8 Static stability and pitching moment with angle of attack curve relation [11]

For a statically stable missile an increase in angle of attack results in a decrease in pitching moment, eventually causing a decrease in angle of attack. Opposite occurs for a statically unstable missile as shown in Figure 1.8.

Static margin is defined as the distance between the center of gravity (X_{cg}) and center of pressure locations (X_{cp}). For the missile design problems, a certain level of static margin is used to ensure positive static stability.

$$SM = \frac{X_{cp} - X_{cg}}{D} \quad (1.4)$$

1.3.2 Aerodynamic Trim and Control Effectiveness

At aerodynamic trim condition:

- Moment terms are zero about center of gravity location
- Force terms are balanced
- Controls are in trim condition

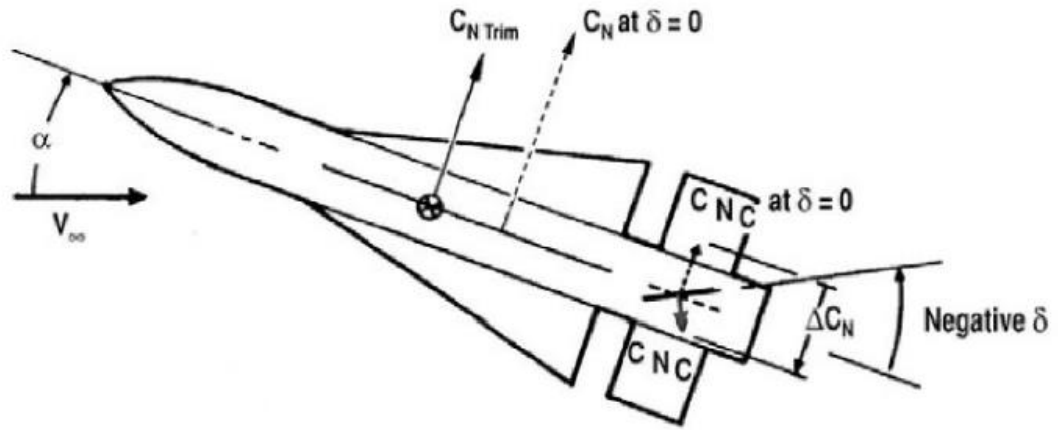


Figure 1.9 Tail control deflection for aerodynamic trim condition [11]

Control effectiveness is defined as the ratio of the control deflection required for trim (δ_{trim}) divided by the trim angle of attack (α).

$$C.E. = \frac{\delta_{trim}}{\alpha} \quad (1.5)$$

1.3.3 Trim Load Factor

The load factor is a measure of the aerodynamic maneuver capability of a missile. It is defined as the ratio of aerodynamic normal force to the weight of the missile:

$$n = \frac{N}{W} \quad (1.6)$$

where W is the weight of the missile and N is the normal force.

1.3.4 Pitching Moment due to Sideslip Angle and Vortex Breakdown

The pitching moment due to sideslip derivative is formulated as follows:

$$C_{m\beta} = \frac{\Delta C_m}{\Delta \beta} \quad (1.7)$$

The pitching moment due to sideslip angle is a cross coupling effect which occurs in asymmetric flow conditions, or unsteady flow conditions such as high angles of attack. This term usually may arise due to asymmetric vortices triggered by

asymmetric flow conditions in steady flow, or due to nature of unsteady flow. This term may be neglected for comparatively less maneuverable aircraft problems, but has importance for missiles and high maneuverability military aircrafts. If there are cross coupling effects due to sideslip angle in pitching moment:

$$C_{m\beta} \neq 0 \quad (1.8)$$

If this derivative numerically grows, the cross coupling effect become larger.

The flow around the missile at high angles of attack is characterized by large regions of flow separation [12]. The asymmetric vortices start with unsteadiness in the flow field at some critical angles of attack for high angle of attack. However, for missiles both at moderate or low angles of attack with a certain sideslip angle, due to asymmetric orientation to the flow the asymmetric vortices are shed.

Considering swirling flows the abrupt change of the flow structure due to adverse pressure gradients is called vortex breakdown (also known as vortex bursting). This phenomenon is illustrated in Figure 1.10 for delta wings [12]. Actually, vortex breakdown is very often seen in low aspect ratio wings. However, vortices are beneficial since due to formation of vortices additional lift is produced in low aspect ratio wings, called vortex lift. If vortex breakdown occurs, it results in the loss of vortex lift. Therefore, vortex related phenomena like vortex breakdown makes the low aspect ratio aerodynamics harder to estimate using fast prediction methods.

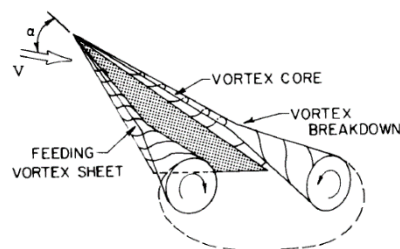


Figure 1.10 Vortex breakdown sketch for delta wings [12]

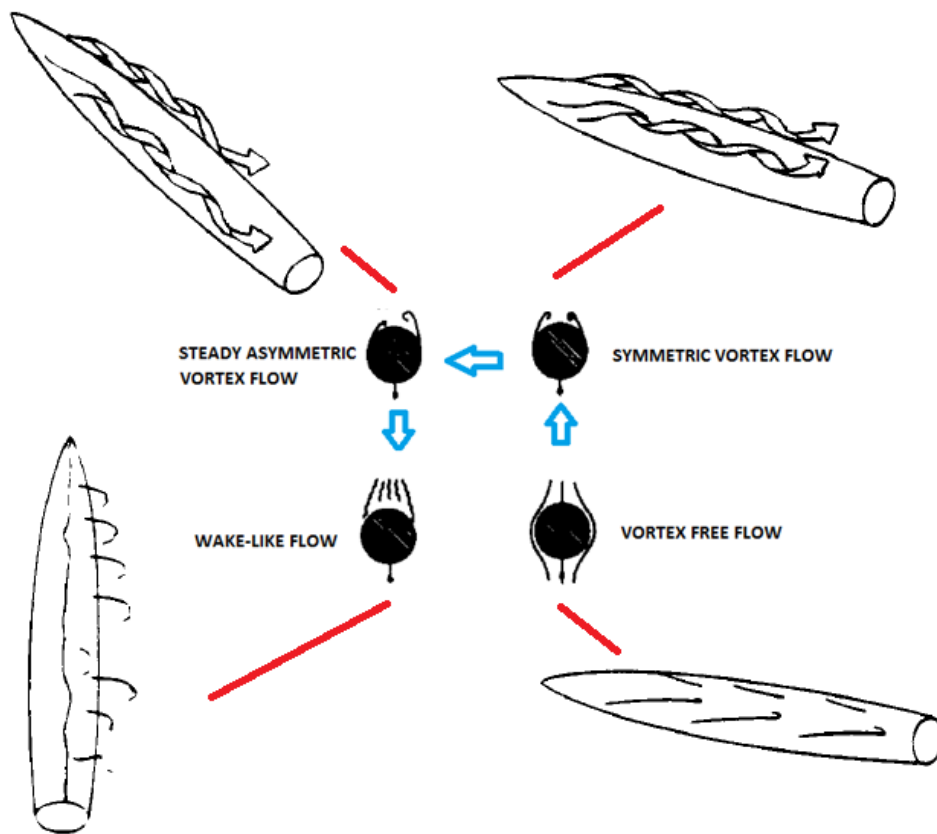


Figure 1.11 Cross sectional aerodynamic flow patterns [12]

As seen in Figure 1.11, four major cross sectional flow patterns occur in a typical missile flight. If the level of complexity increases, the flow changes from vortex-free flow to the wake-like flow in the order shown in the figure.

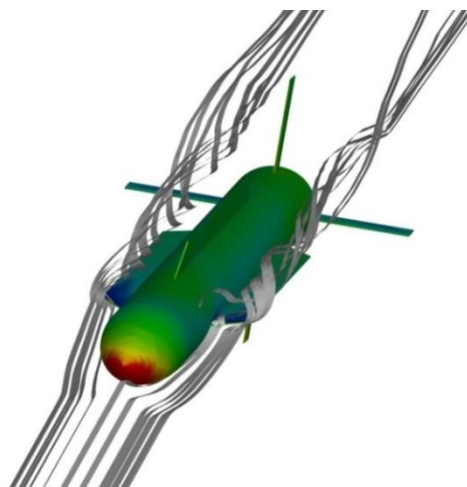


Figure 1.12 Vortex shedding from the strake panels

Analogous to high angle of attack, for a missile both at an angle of attack and sideslip, due to asymmetric orientation to the flow direction, asymmetric vortex shedding occurs. A sample representation of the asymmetric vortex shedding from the long strake panels which is taken from CFD study in this thesis can be seen in Figure 1.12

1.4 Considerations of Missile Design Analysis

In missile analysis from design oriented view, there are certain considerations during external configuration design optimization problem [12]

- Packaging efficiency for compactness
- Fast response
- Positive static stability
- Low drag
- High maneuverability
- Constant center of pressure location
- Small hinge moments
- Configurationally simplicity

The challenge of the aerodynamic design engineer is to design efficiently but also not complex.

1.5 Literature Survey

The missiles having strakes (sometimes referred to as dorsals) are compact missiles with high maneuver capability usually designed to fly at supersonic speeds and strake fins are used in space limited applications. Another benefit in terms of structures is that they serve as cableways and remove the need for additional parts for cableways.

The strake fin structures are employed mainly to fix the loss in the aerodynamic efficiency [13]. The strong body fin interactions produce extra lift due to vortices formed along the edges of the long wing tips [2]. Thanks to this extra vortex lift, the

total lift of the strake fins may even beat the lift of the high aspect ratio fins having the same planform area. Low rolling moment compared to high aspect ratio wings and small center of pressure shift are other benefits of strake usage [1]. They can be used effectively to increase the balanced maneuverability capability of the missile. Actually, by using strakes the directional stability might be increased, which results in a large increase in the stable trimmed maneuver capability [14].

Moreover, the strakes are used in some applications to reduce asymmetric dispersion. The strake fins are usually placed over the nose, or the central body. By placing strakes or strakelets at appropriate locations on the body the flow separation over the body is controlled. Controlling the flow separation location on the body allows minimizing lateral forces due to vortices formed near the end of the body [14].

The strake fins will observe an increased angle of attack with respect to the geometric angle of attack due to body upwash. It should also be mentioned that placing tail fins following strakes allow tail fins to be exposed to lower effective angles of attack than the geometric angle of attack delaying the stall angle of attack at the tail [2].

Historically, missile aerodynamicists attempted to develop fast prediction methods to quickly estimate aerodynamic forces and moments. These engineering level methods came into maturity level to be used during conceptual missile design. Engineering level methods are composed in fast prediction codes, such as Missile DATCOM, MISL3, and Aeroprediction Code (AP). Most of the time, these codes are enough to carry out design and sizing studies for classical missile geometries. In other words, conventional missiles can be modeled successfully with fast prediction tools. However, for very low aspect ratio wings, engineering level methods are limited in success due to complex interaction of the body upwash and wing carryover flow fields. Alternatively, accurate predictions are viable through Computational Fluid Dynamics (CFD) techniques [2].

In missile aerodynamics, the missile geometry is modeled as a slender body with low aspect ratio lifting surfaces. The engineering level method for body aerodynamics

originates from the Munk's theory for slender airship hulls and is later extended into missile aerodynamics. Theoretical and semi-empirical methods for modeling missile body aerodynamics based on slender body theory are introduced by different researchers. The most widely used slender body theory based approach is viscous cross flow approach developed by Allen and Perkins [15]. Nielsen, in his book "Missile Aerodynamics" exhibits a summary of the slender body theory based methods [16]. For fin alone aerodynamics various theoretical and semi-empirical methods such as potential flow theory, Lucero's method and Rosema's improvement on Lucero's method are used [17]. For modeling nonlinear aerodynamics of missile fins and control surfaces at high angles of attack, equivalent angle of attack approach was developed by Hemsch and Nielsen [18]. After component treatment, component build up methodology is used to obtain complete configuration loads from body alone and fin alone loads by the accounting for the interference effects. There are various engineering level codes developed for solving missile aerodynamics based on these theoretical methods and each of them may give different results depending on the missile configuration and the flow regime [19].

Missiles with very low aspect ratio fins needed special treatments and different researchers had investigations about this problem. White, in his study developed an empirical correlation between normal force and center of pressure of the strake unit which included all of the strake-alone, strake in the presence of the body and body in the presence of the strake [2]. Sigal in his study in 2006 developed unified crossflow method for longitudinal aerodynamics estimation of missiles with strakes [20]. He used crossflow drag coefficient in estimation of normal force and center of pressure of these configurations with special treatment of cross flow drag coefficient in the body part including strakes. Later, in 2010 Sigal and Blake had another study establishing empirical correlations for normal force and center of pressure at small angles of attack by using wind tunnel test data [21]. According to their statement, their method produced similar results to Missile DATCOM 2007 version, but had limited success.

Simpson and Birch investigated a comparative study consisting of three distinct wing-body configurations. Body being unchanged, a strake configuration (B11AW22A3), a conventional low aspect ratio wing and a delta planform fin having the same area as the strake configuration were analyzed. The tools accompanying their wind tunnel experiments included Missile DATCOM and IMPNS CFD tool. They found that although the conventional wing has a small normal force advantage, the B11AW22A3 strake configuration has significantly smaller axial force for small incidences. B11AW22A3 configuration was found to have the lowest rolling moment of all, but has vortex interference at 45 degrees roll angle. They found Missile DATCOM 97 unreliable for applications to very low aspect ratio wings due to misprediction of body carryover normal force and, recognized simple vortex methods in DATCOM 97 to be inferior, but their CFD applications were successful [22].

In recent years, Tulig, in his thesis developed an engineering level method based on 2D unsteady potential formulation (free vortex model) to estimate normal force and center of pressure of cruciform missiles with strakes in plus orientation at supersonic Mach numbers. He performed a detailed analysis of the vortex shedding for the body and very low aspect ratio lifting surface combinations. He tried different vortex models and finally developed a free vortex model. He finally developed an integrated formulation to estimate the nonlinear behavior of wing-body carryover factor. The results of his formulation for center of pressure and normal force of body-strake combinations had different accuracies for different problems. For example, in B11AW22A3 test case, the normal force is under predicted for high angles of attack and center of pressure is predicted forward compared to that of the experimental data [3].

Tulig also analyzed the flow over body-strake combination. He asserted that the body-strake aerodynamics is dominated by flow separation at the side edge. There was no leading edge vortex shed since the leading edge of the strake fin set is supersonic for Mach numbers greater than 2.0. Vortices were expected to concentrate into a single concentrated vortex sheet at low angles of attack while multiple vortices were shed at high angles of attack dependent on the cross flow Mach number. It

should be noted that the side edge vortex remained attached until higher angles of attack [3].

Missile external configuration design is carried out by various optimization studies. Both stochastic and gradient methods were used in previous studies. Akgül and Tiftikçi performed a 2D CFD based nose shape optimization study to minimize axial force coefficient by using gradient based steepest descent method with line search [23]. Arslan in his thesis obtained aerodynamic coefficients from Missile DATCOM and performed a design study to optimize missile external configuration for a generic air to ground missile by using a stochastic optimization method [10].

1.6 Aim of the Thesis

The missile strake configurations are widely used for supersonic missiles of moderate to high maneuverability. However, engineering level codes are inferior and not robust for design of such missiles. Alternatively CFD can be used to evaluate aerodynamic performance of the candidate missile configurations. Therefore, a CFD based optimization approach is developed with the main aim of reducing coupling effects on pitching moment due to sideslip angle. Eventually, it is aimed to minimize coupling effects on the longitudinal maneuver plane of the missile from the sideslip angle while keeping static margin nearly constant.

The detailed analyses and a comparative validation are performed to investigate aerodynamic capabilities of fast prediction methods including White's method and DATCOM. Before optimization study, a validation study of the CFD tools with a selected test case from literature is performed. After validating CFD tool with the wind tunnel data, strake planform optimization is performed.

The missile configurations evaluated during iterations are meshed by GAMBIT tool, and boundary layer developed with TGRID. The CFD solutions are obtained from FLUENT solver. Using CFD results the aerodynamic performance parameters are calculated and these results are input into the optimization problem.

A stochastic and a gradient based optimization method are selected for comparison. Particle Swarm Optimization (PSO) is a population based stochastic method and Steepest Descent with Line Search is a gradient based method. Both PSO and Steepest Descent with Line Search are applied for the aerodynamic design optimization problem.

CHAPTER 2

METHODOLOGY

In this chapter, the CFD tool and fast prediction methods used in this thesis will be introduced. The governing equations for Reynolds Averaged Navies Stokes Equations (RANS) and solver configuration for the FLUENT CFD solver used in this study will be introduced. The White's experimental method and Missile DATCOM semi-empirical solution will be explained in details. Moreover, stochastic Particle Swarm Optimization (PSO) method and gradient based Steepest Descent with Line Search method are explained in detail. A flowchart and an application of the PSO algorithm are also presented.

2.1 The Aerodynamic Estimation Tools

The details of the aerodynamic tools used in this thesis are given in this part. The FLUENT is used as the CFD solver in validation and optimization studies. Semi-empirical Missile DATCOM and experimental White's method are used as fast prediction tools in the D57 test case validation study.

2.1.1 The CFD Solver

The FLUENT CFD tool is used in this thesis as the CFD solver. Its working scheme is given in Figure 2.1. Previous CFD studies by different researches are considered in the solver configuration, turbulence model selection and grid sizing. In a previous CFD study for NASA Dual Control missile it was shown that for pitching moment and normal force coefficients a medium grid size would be enough [24].

The solver is configured to be density based solver with energy equation. Grid is discretized based on the finite volume scheme and for gradient evaluation; Green

Gauss Node Based approach is employed. Spatial domain is discretized based on the first order upwind scheme and for flux calculations ROE-FDS scheme is employed. Solution is initialized from the pressure far field and solved towards the inner domain. The turbulence parameters such as the turbulent dissipation rate are changed from the first order to second order and the Courant number is adjusted suitably during the iterations. The compressible RANS equations are solved by FLUENT solver using implicit solver (Gauss Seidel).

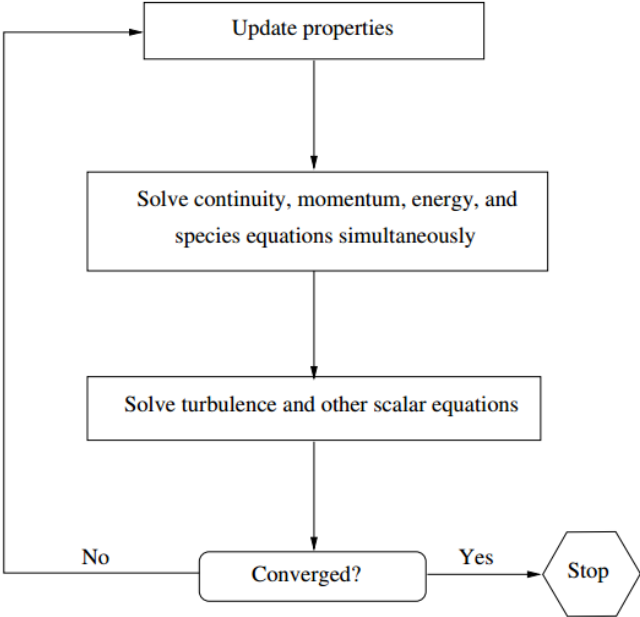


Figure 2.1 Density based solution methodology [25]

2.1.1.1 Reynolds Averaged Navier Stokes Equations

The Reynolds Averaged Navier Stokes Equations used in CFD solver are presented in this part.

The equation for the conservation of mass is as follows:

$$\frac{\partial \rho}{\partial t} + \nabla \cdot (\rho \vec{u}) = 0 \tag{2.1}$$

The second law fundamental for a fluid flow is conservation of the momentum:

$$\rho \frac{\partial \vec{u}}{\partial t} + \rho \vec{u} \cdot \nabla \vec{u} = -\nabla p + \nabla \cdot \vec{\tau} \quad (2.2)$$

where shear stress tensor relation is :

$$\vec{\tau} = \lambda \nabla \cdot \vec{u} \bar{\bar{I}} + \mu (\nabla \vec{u} + \nabla \vec{u}^T) \quad (2.3)$$

$\bar{\bar{I}}$: identity matrix

μ : coefficient of viscosity

$$\lambda = -\frac{2}{3}\mu \quad (2.4)$$

Since dynamic viscosity is temperature dependent we have the following relation by Sutherland's law:

$$\mu = \frac{1.45T^{\frac{3}{4}}}{T + 110} 10^{-6} \quad (2.5)$$

The conservation of energy formulation is:

$$\rho \frac{Dh}{Dt} = \frac{Dp}{Dt} + \nabla \cdot (k\nabla T) + \tau_{ij} \frac{\partial u_i}{\partial x_j} \quad (2.6)$$

$$\frac{D(\cdot)}{Dt} = \frac{\partial}{\partial t} + \vec{u} \cdot \nabla(\cdot) \quad (2.7)$$

The complementary equation is ideal gas relation for compressible flow:

$$p = \rho \cdot R \cdot T \quad (2.8)$$

The stagnation state properties characterizing the compressible flow are accounted by the following equations [26]:

$$\frac{p_0}{p} = \left(1 + \frac{\gamma - 1}{2} M^2\right)^{\gamma/(\gamma-1)} \quad (2.9)$$

$$\frac{T}{T_0} = 1 + \frac{\gamma - 1}{2} M^2 \quad (2.10)$$

2.1.1.2 Turbulence Model Selection

Turbulence modeling is the construction of a computational model to include the effects of unsteady fluctuations due to chaotic or turbulent flow. Instead of calculating the full time dependent flow with details, averaging the mean flow characteristics by simple differential algebraic equations is preferred to represent the flow profile. Using these simplified equations, it is possible to reduce computational power required considerably. The mostly used turbulence modeling approaches are Reynolds Averaged Navies Stokes (RANS), Large Eddy Simulation (LES) and Direct Numerical Simulation (DNS) [27].

The most practical and computationally friendly method for industrial applications is the RANS method. In the RANS method, terms are separated into average and fluctuating parts. For example velocity is represented as:

$$u_i = \bar{u}_i + u_i' \quad (2.11)$$

Based on RANS the classical there are a number of turbulence models according to the number of additional partial differential equations to be solved.

In this thesis a two equation model, realizable k- ε is used as the turbulence model.

The realizable k- ε method is proven to be reliable, effective and comparatively fast for missile aerodynamic estimations [24], and detailed below.

In general, k- ε models are based on the mechanisms affecting the turbulent kinetic energy. Particularly, realizable k- ε model contains improved equations for the dissipation rate, ε which is derived from the transport of mean square vorticity

fluctuation. Moreover, turbulent viscosity formulation is updated in this model. The performance of the realizable $k-\varepsilon$ method is improved compared to standard $k-\varepsilon$ method for problems involving boundary layer with strong adverse pressure gradients, rotational and separating flows [27].

2.1.1.3 Development of an Automatic Grid Generation Tool

In this study, standard missile geometry was used consisting of cross orientation, variable geometry four strakes in front part and non-changing tail geometry on the body adjacent to the base. Plot of the configurations was automated with the automatic grid code by making parametric journal file for the strake planform geometry.

It was possible to develop automatic grid tool for meshing the whole missile with the help of GAMBIT meshing tool. The non-changing parts such as the tail and nose were meshed with the same grid density. However, for the varying strake geometry, the grid size was adjusted with a size function starting with a constant small mesh size and growing proportional to the chord length of the strake with a maximum mesh size limit imposed. On the other hand, the center body was split up into two parts, one including tail fin set and the other part including strake fin set. In these two sections the mesh growth was adjusted with size functions. The growth rate for surface grid was 1.1 and the growth rate for volume grid was 1.15. The grid size was decreased in the parts where the flow changes direction. A simple representation of the split regions for the mesh generation is shown in the figure below:

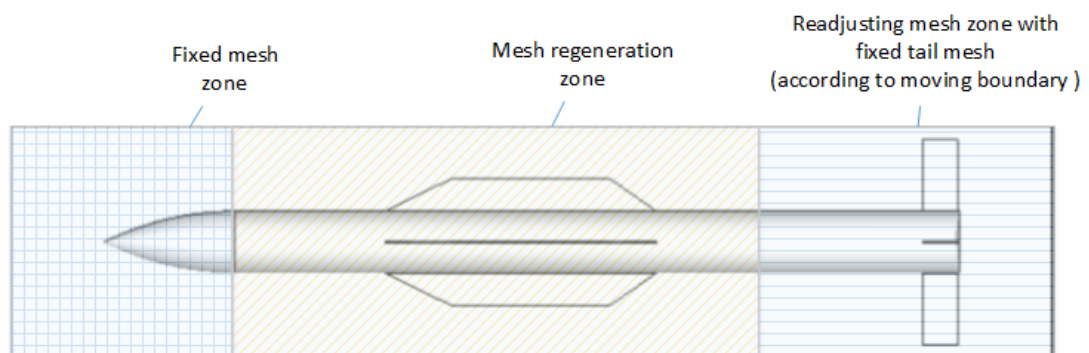


Figure 2.2 Mesh generation regions for the body-strake-tail configuration

By defining parameters for meshing based on the strake length it was possible to automate the process of meshing. The center body was split at the middle point between the trailing edge of the strake and the leading edge of the tail. Moreover, the growth rate of the grid along the edge of the chord was adjusted to be 1.15 with a certain maximum size limit imposed.

The automatic grid code had the ability to prepare the necessary journal file, by adjusting the parameters such as body split-up location, and body size function based on the strake chord length. The Gambit meshing tool was called by the code with the prepared journal file for all configurations at the iteration step.

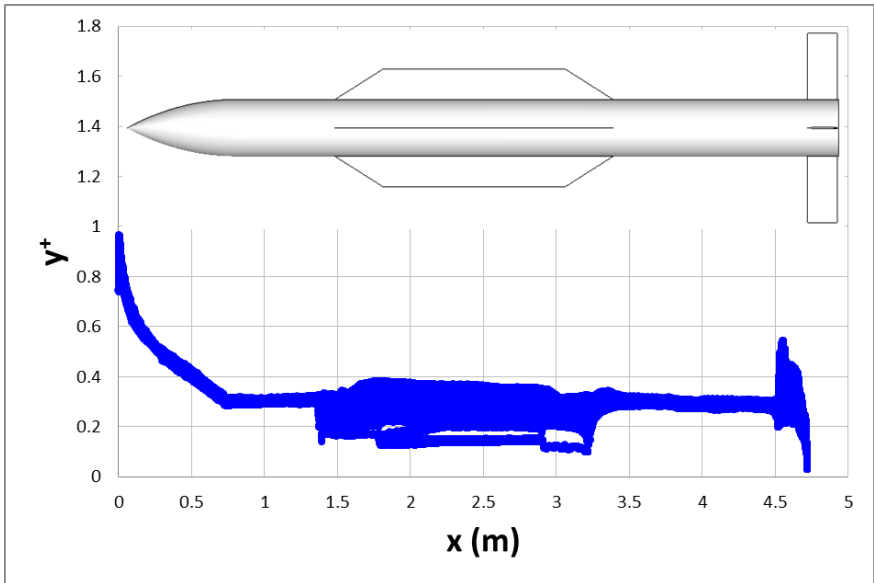


Figure 2.3 y^+ Distribution over wall surfaces

For the turbulence model selection in this study, to adjust the proper size of the boundary mesh near the wall, y^+ value was adjusted to be less than 1. For Mach 2.01 the y^+ distribution on wall surfaces is shown in Figure 2.3 for an intermediate configuration. The first height of the boundary layer mesh was calculated and growth from the wall surfaces was adjusted accordingly to ensure a y^+ value of less than 1.

For grid generation a previous CFD study for NASA Dual Control missile was considered. In that study, it was shown that medium grid size would be enough for estimation of pitching moment and normal force coefficients [24]. Therefore, for the

whole domain, automatic grid generation part of our code generated a medium mesh having 3-4.0 million tetrahedral volume elements.

The population of the optimization routine consisted of four members. Around each member local search by tunneling was performed. The tunneling part of the optimization routine was parallelized, but it was not simple to make the whole process automatic since different programs were used as mesher and solver.

The FLUENT solutions could be obtained easily with parallel runs using multiple processors. However, initially the GAMBIT meshing process had to run serially meaning that while a configuration was being meshed; another configuration had to wait in queue. The solution to this problem was found in Sun Grid Engine. The Sun Grid Engine made it possible to run parallel GAMBIT processes instantaneously with multiple input batch files prepared by the optimization code during the scan around the current configuration. The batch jobs were submitted to the Sun Grid engine nodes, different nodes running different instances of the Gambit meshing scheme.

2.1.2 The Missile DATCOM

The Missile DATCOM 97 and the Missile DATCOM 2009 versions were employed in this study. In Missile DATCOM 1997 version Lucero's method was used to estimate fin alone normal force and center of pressure of missiles with very low aspect ratio wings [28]. In Missile DATCOM 2009, Lucero's empirical method improved by Rosema is used for very low aspect ratio fins. The fins are categorized into rectangular, delta, and trapezoidal considering the planform shape of the panels in Missile DATCOM 2009. Lucero's empirical method improved by Rosema is used for rectangular fins, for delta fins linear theory is employed with thickness correction factors, and Lucero's method and linear theory are used interchangeably for trapezoidal fins [17].

The Missile DATCOM has special treatment to include the interference effects developed due to vortex formation from interaction of body and fin components. In Missile DATCOM version 2009 and previous versions, the fin shed vortices are

represented by a single vortex sheet released at the trailing edge, interacting with the downstream tail surfaces. This single vortex representation reduces the accuracy of the results, and multiple vortex model is necessary to better represent the effect of the vortices on downstream tail surfaces [29]. In addition, according to the previous studies, the Missile DATCOM has biggest error in estimating the body-carryover effect (K_{Bw}) which is the force increment on the body due to the interaction effects from the fin panels [22]. This is mainly due to the fact that the methods for modeling vortices shed from the side edges of the lifting surfaces have limited accuracy [3].

2.1.3 The White's Method

White in his study establishes an empirical correlation between geometrical parameters and aerodynamic data (normal force and center of pressure) by using a huge wind tunnel database. The strake span, body radius, body maximum frontal area and strake planform area are the geometrical parameters used for the normal force estimation of the strake unit.

2.2 Optimization Methods

In the optimization problems, an objective function is formed to represent certain goals in mathematical terms. The main aim of the optimization problem is minimize or maximize the objective function subject to the constraints of the problem. Defining an objective function representative of the problem, both stochastic and gradient methods are employed in design studies. In this thesis, the deterministic gradient based optimization method and stochastic Particle Swarm Optimization method are employed for the same objective function definition. The details of these two optimization methods are represented in this part.

2.2.1 Particle Swarm Optimization Method

Particle swarm method is an optimization method simulating the social behavior of individuals in bird flock or fish school during group movement. A multidimensional search space is formed with a position vector representing individuals and another vector for determining the movement of the individuals called velocity vector. Each

individual is called particle and moves in search space remembering the best position it has seen and communicates with other members to learn other good positions. . The PSO algorithm decides the velocity vector of the particles regarding the current best position of the particle and global best position of the swarm. The calculated velocity is then used to update the position vectors. This movement of particles as a swarm searching for the best solution is continued iteratively until a certain residual is reached. Particle Swarm Optimization (PSO) is very efficient even for difficult problems according to the previous studies made [30]. Some of the behavioral movements of an individual in a bird swarm are simulated by Craig Reynolds in 1986 as shown below [31].

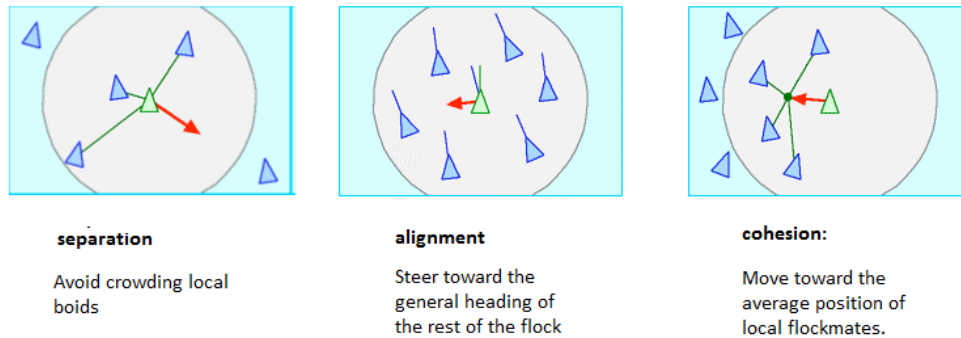


Figure 2.4 Simulation of the individual behavior in motion of flocks of birds [31]

2.2.1.1 The Details of the PSO Algorithm

We have an n-dimensional swarm of particles with the following vectors, for i^{th} particle:

$$\mathbf{x}_i = (x_{i,1}, x_{i,2}, x_{i,3} \dots, x_{i,n}) \quad : n \text{ dimensional position vector}$$

$$\mathbf{v}_i = (v_{i,1}, v_{i,2}, v_{i,3} \dots, v_{i,n}) \quad : n \text{ dimensional velocity vector}$$

$$\mathbf{p}_{i,best} = (p_{i,1}, p_{i,2}, p_{i,3} \dots, p_{i,n})$$

: n dimensional best position vector for the particle

$$\mathbf{g}_{best} = (g_1, g_2, g_3 \dots, g_n) \quad : n - \text{dim. best position vector for all particles}$$

The particle position and velocity is updated according to the local best position of the particle and global best position of the swarm by the following equations for i^{th} particle at each dimension $d=1,n$:

$$v_{i,d+1} = \omega \cdot v_{i,d} + c_1 \cdot \varphi_1 \cdot (p_{i,d} - x_{i,d}) + c_2 \cdot \varphi_2 (g_d - x_i) \quad (2.12)$$

$$\mathbf{x}_{i+1} = \mathbf{x}_i + \mathbf{v}_i \quad (2.13)$$

c_1, c_2 : positive constants between 0 and 1

Comparing the objective function, particle's best position is updated (local best position):

$$\text{if } f(\mathbf{x}_i) < f(\mathbf{p}_i) \text{ then } \mathbf{p}_i = \mathbf{x}_i$$

Comparing the objective function, update swarm's best position (global best position):

$$\text{if } f(\mathbf{p}_i) < f(\mathbf{g}_{best}) \text{ then } \mathbf{g}_{best} = \mathbf{p}_i$$

$\omega, \varphi_1, \varphi_2$ are user controlled parameters to control the behavior and efficiency of the PSO [30].

The particles of the swarm interact with neighborhood and global swarm, and try to get positions similar to their previous best positions and to that of the better neighbors. Particle's next position is updated based on the swarm's best position and the best position in particle's memory as shown in Figure 2.4. The green line represents inertia, blue line represents personal influence and the red line represents social influence of the swarm.

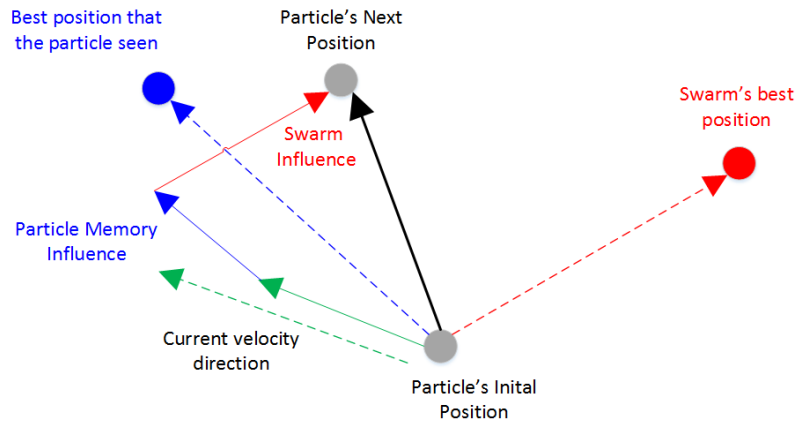


Figure 2.5 The Particle Swarm Optimization Method New Position Calculation

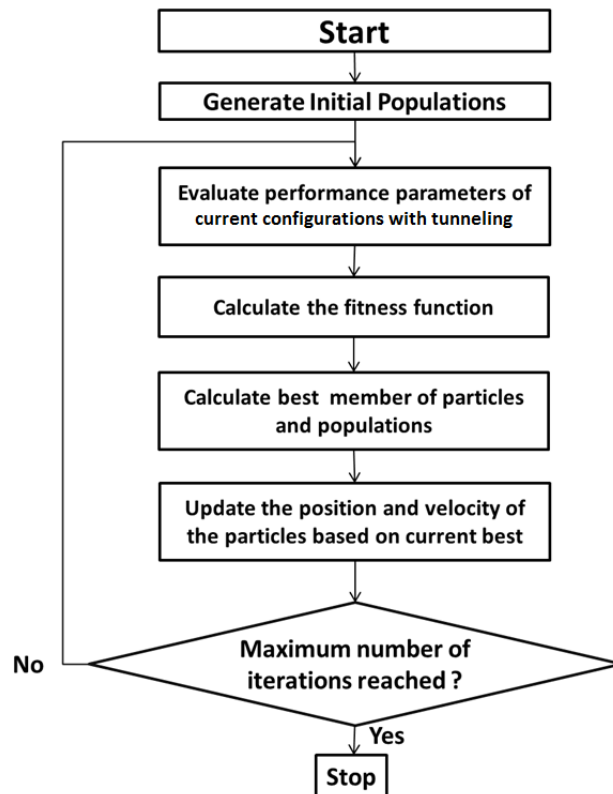


Figure 2.6 Flowchart for the Optimization of Strake Planform Geometry with Particle Swarm Optimization

2.2.1.2 An Application of the PSO algorithm

Before aerodynamic performance optimization, a preliminary optimization study of the test function “Eggholder” is made by using PSO optimization method, and the results are shown below. The contour below shows egg holder function for positive values of x and y.

$$f(x,y) = -(y + 47) \cdot \sin\left(\sqrt{\left|y + \frac{x}{2} + 47\right|}\right) - x \cdot \sin\left(\sqrt{|x - (y + 47)|}\right) \quad (2.14)$$

(Eggholder Function)

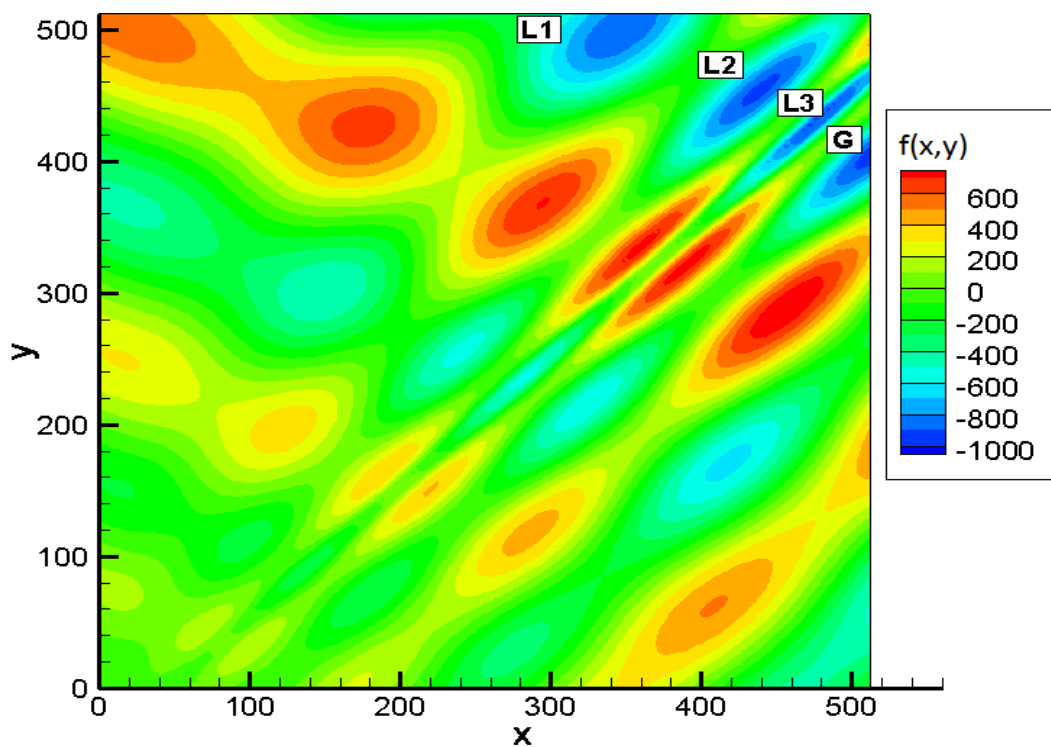


Figure 2.7 Contour plot of “Eggholder” function

The local minimas shown by L1, L2 and L3 above in the contour plot are:

$$f(347.3,499.4) = -888.9$$

$$f(439.5,454.0) = -935.3$$

$$f(482.3,432.9) = -956.9$$

and the global minimum shown by “G” above in the contour is:

$$f(512.0,404.2) = -959.6$$

It can be observed that PSO method ensures global solution and can be used for aerodynamic performance optimization.

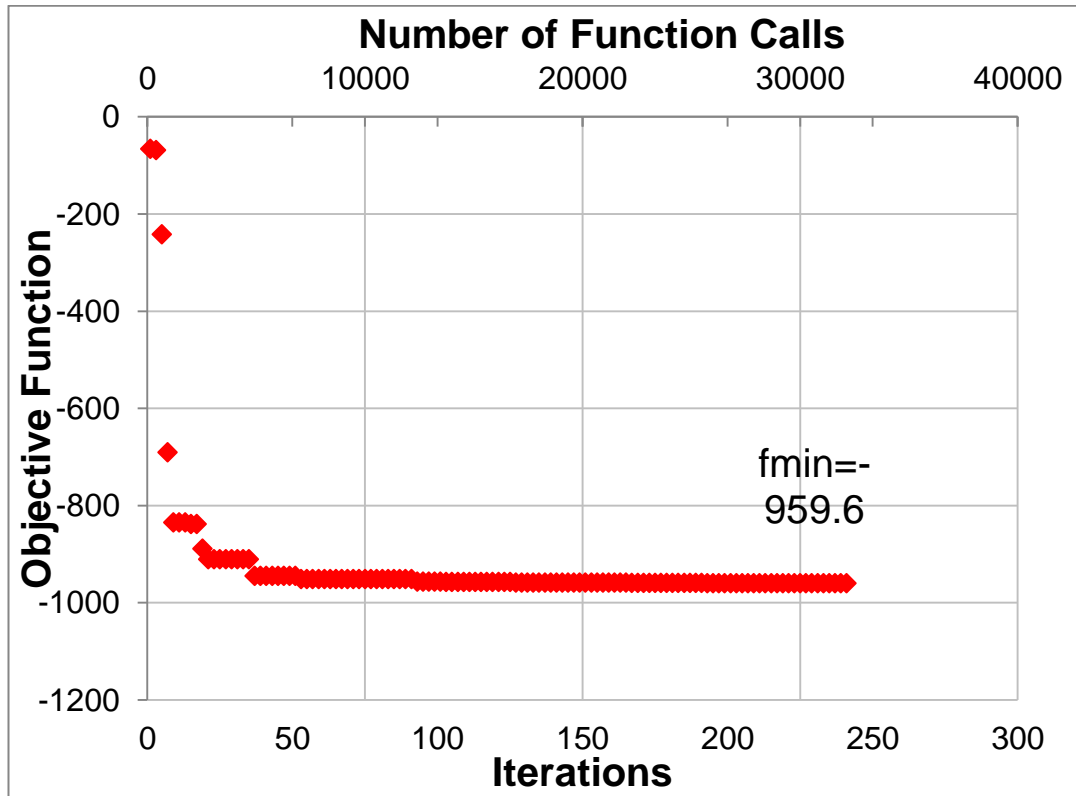


Figure 2.8 Number of iterations and number of function calls during iterations by

The PSO method is configured to have a population consisting of 20 members initially. All of the particles have their own local best in their neighborhood. The paths followed by the local particles at intervals of nine iterations are given in Figure 2.9 starting at 15th iteration. As can be seen from the figures the particles move in the domain, change direction in some regions, sometimes move away from each other or towards each other, but finally they synchronize with each other. The synchronous paths followed by different particles direct them finally to upper right portion of the domain can be observed from Figure 2.9.

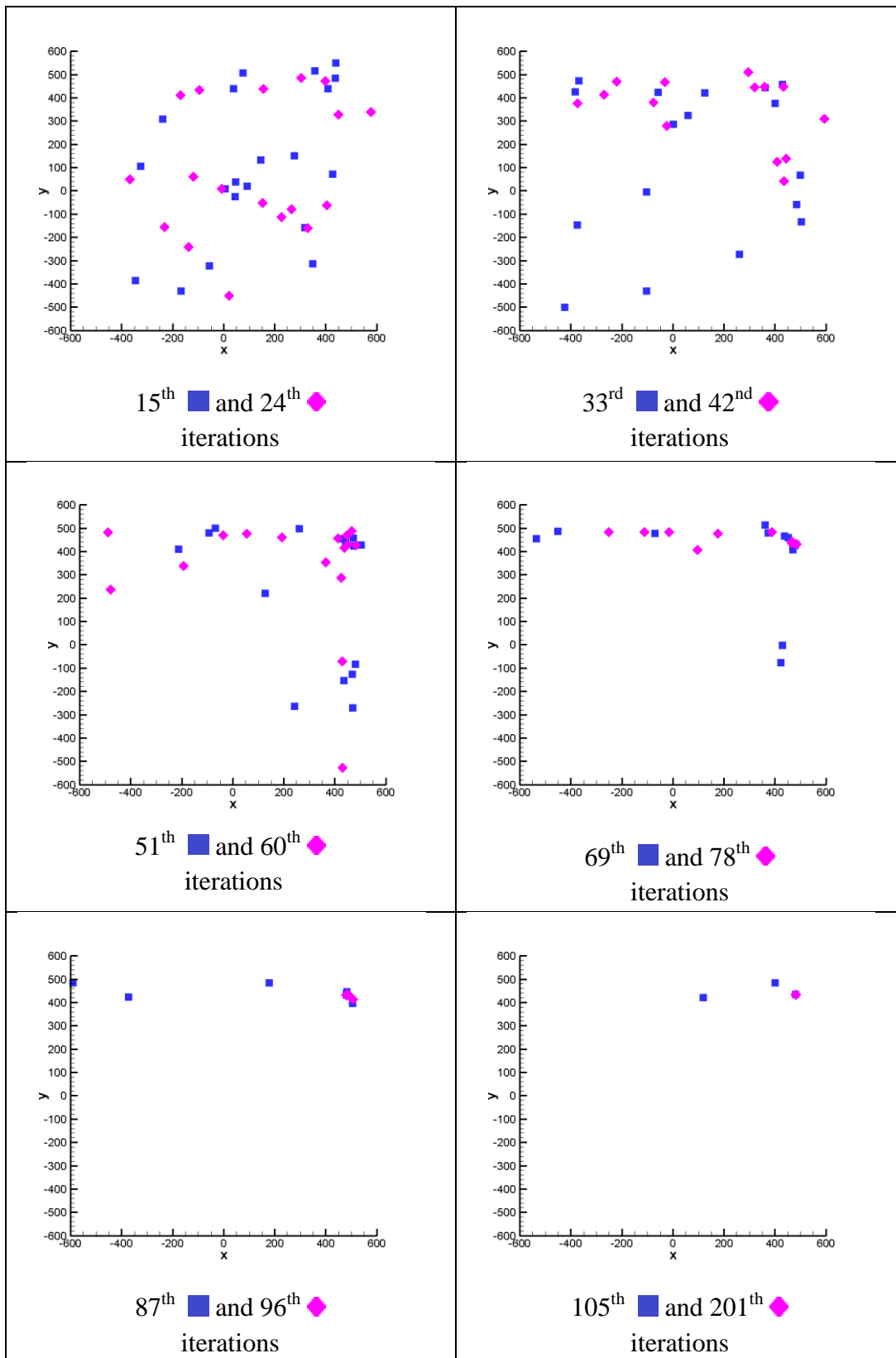


Figure 2.9 The movement of the particles in search space during PSO iterations (Former iterations are shown by blue-square and latter ones by pink-diamond.)

2.2.2 Gradient Based Optimization

Steepest descent with line search is used as a gradient based optimization method. The gradient of a function at a point represents the rate of change of the function at that point. In other words, the negative gradient of a function ($-\nabla F(X)$) represents the direction in which the function decreases.

In gradient based optimization, the gradient of the function is calculated at the current point. The line search steps in the inverse direction of the gradient function are taken until the function starts to increase. In these steps, α is searched for minimizing the objective function at the current point:

$$F(X^i - \alpha \cdot \nabla F(X^i)) \quad (2.15)$$

After the α is found by the line search process, the solution is updated by using the step size α found:

$$X^{i+1} = X^i - \alpha \cdot \nabla F(X^i) \quad (2.16)$$

The gradient is calculated at the updated point and the above process is continued until the gradient of the function equals zero.

The gradient method quickly converges, but usually finds the local optimum. Gradient based optimization method has fast convergence rate and therefore it is preferred in computational problems [23].

CHAPTER 3

RESULTS AND DISCUSSION

In this part, a comparative study of the tools for estimating aerodynamics of missiles having strakes is performed. The aerodynamic tools used in this comparative study consist of Missile DATCOM, FLUENT and, White's experimental method. The CFD tool is found to be robust and consistent with the experimental results. Since CFD tool is validated, using this tool a gradient based optimization method and a stochastic optimization method are applied to minimize the change of the pitching moment with sideslip angle by changing the strake geometry. The results of strake design study by these two optimization methods are presented. The geometric design and aerodynamic performance parameters obtained during the optimization iterations are analyzed in this chapter. The details of the optimum geometry are given and the results of the optimization study are discussed.

3.1 Aerodynamic Validation Study with D57 Missile Configuration

Highly maneuverable supersonic missiles usually include very low aspect ratio wings. Strakes are very suitable for span constrained problems as already mentioned in the previous chapters. Strake type wings (also referred to as dorsals) interacting mutually with the body have non-linear aerodynamic characteristics. Linear methods are not enough to model strake's aerodynamic effects and even nonlinear corrections are insufficient in most of the cases. Vortex sheets are attached along the long strake tip edges arising from the mutual interference of the strake fins and the body, producing vortex lift. Therefore, not only lift but also maneuverability of the missiles is increased by employing strakes.

During the course of missile aerodynamics, both theoretical and empirical methods were developed for estimating the normal force and center of pressure of very low aspect ratio wings. Their accuracy varies depending on the flow regime and the missile configuration studied.

In this chapter, a CFD analysis is performed for the selected D57 strake test case to predict the normal force and center of pressure of the strake unit. In the grid sizing, turbulence model selection, and solver configuration process knowledge obtained from previous CFD are considered [24]. Furthermore, a comparative study of the results of CFD, theoretical and empirical methods is carried out and the results are compared with LTV HSWT 655 Wind Tunnel Test Data. The wind tunnel results were taken from White’s study in which the data was included from Standard Missile Database of Hughes Missile Company [2]. The following methods were included in this study:

- a.) FLUENT
- b.) Missile DATCOM 1997
- c.) Missile DATCOM 2009 / Rosema’s Method
- d.) White’s Method

The fluid properties used in the CFD studies inside FLUENT for test case are as follows:

Table 3.1 The flow properties for D57 test case

Density, ρ	1.225 kg/m ³
Fluid Type	Air
Static Pressure, P_∞	101325 Pa
Static Temperature, T_∞	300 K

Body-strake (D57) - test case is investigated in this study which is in (+) orientation having four panels of strake type. Geometric details of D57 strake and missile body are shown in Figure 3.1.

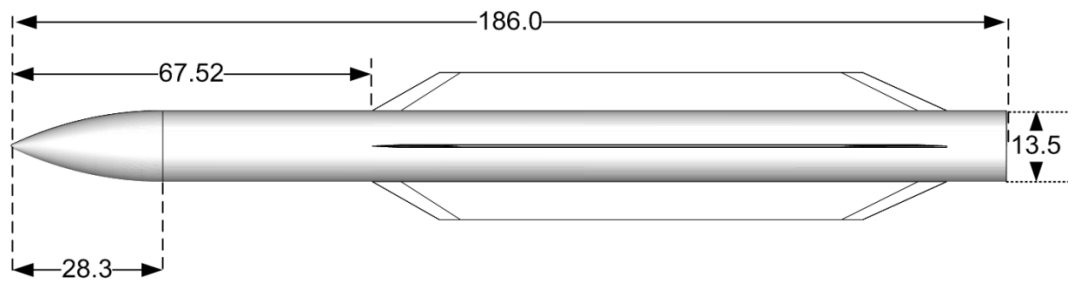


Figure 3.1 Geometric Details of the test case Missile Body and placement of D57 Strake [All dimensions are in inch]

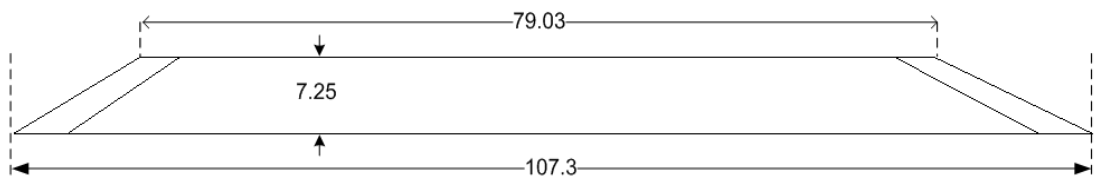


Figure 3.2 Geometric Details of the D57 Strake Panels [All dimensions are in inch]

3.1.1 Computational Grid

The surface meshes of the body-strake (D57) and body alone together with volume meshes of the solution domains are represented in Figure 3.3.

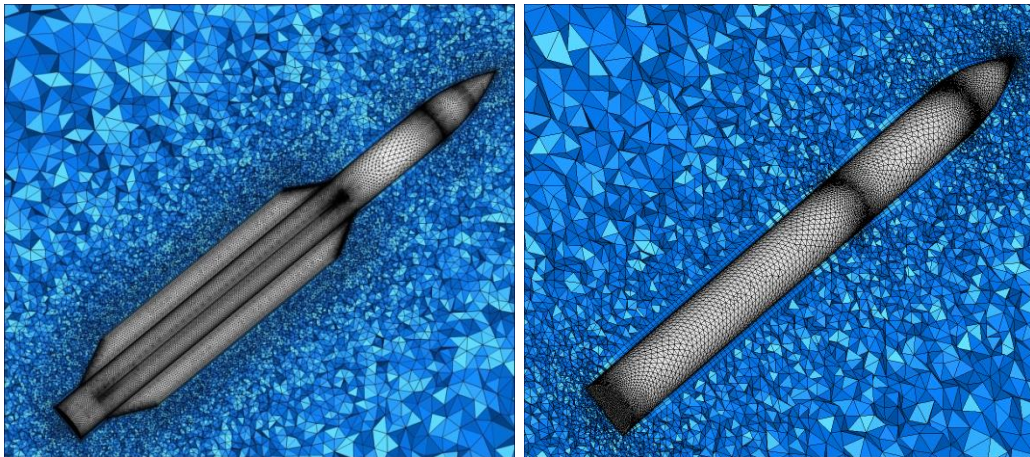


Figure 3.3 A detailed view of Surface and Volume Grid

In the mesh generated for the whole missile there are 291,788 triangular surface elements in missile's outer surface and fluid domain consists of 5,641,729 unstructured volume elements. Boundary layer mesh was generated using TGRID ensuring a y^+ value of 1. To satisfy the y^+ requirement, the first height of the

boundary layer mesh was calculated and growth from the wall surfaces was adjusted accordingly.

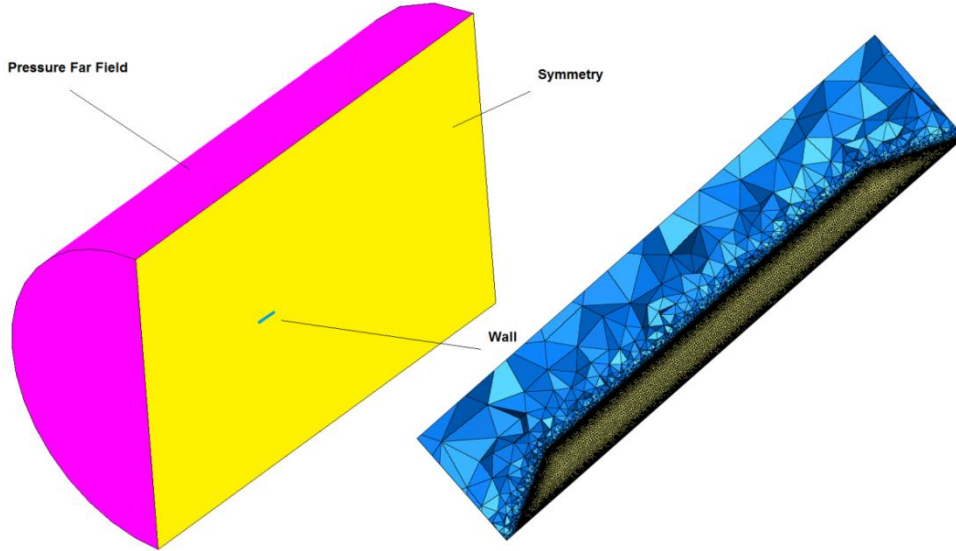


Figure 3.4 Boundary Conditions and Detailed View of the Strake Panel Grid

The strake alone boundary conditions are presented in Figure 3.4. The yellow region shown in the figure shows the symmetry plane which allows strake-alone computations. Strake alone data for the panels in (+) orientation (panel 2 and panel 4) are summed to obtain the results for the whole fin set. Later in this chapter, a force breakdown study is performed to calculate the interference effects by using the strake alone results.

$$C_{N_{strake\ alone}} = C_{N_{panel\ 2}} + C_{N_{panel\ 4}} \quad (3.1)$$

The missile body diameter is taken as the reference length and maximum cross sectional area of the cylindrical section is taken as reference area for aerodynamic calculations. The center of pressure of the strake unit is measured from leading edge point of the strake.

$$L_{ref} = 13.5\ in$$

$$S_{ref} = 143.1387 \text{ in}^2$$

The normal force and pitching moment coefficients of the strake unit are calculated by subtracting body alone values from body-strake values. The center of pressure of the strake unit is calculated by dividing the pitching moment coefficient to normal force coefficient of the strake unit.

$$C_{N_{strake-unit}} = C_{N_{body-strake}} - C_{N_{body-alone}} \quad (3.2)$$

$$C_{m_{strake-unit}} = C_{m_{body-strake}} - C_{m_{body-alone}} \quad (3.3)$$

$$X_{CP_{strake-unit}} = \frac{C_{m_{strake-unit}}}{C_{N_{strake-unit}}} \quad (3.4)$$

CFD solver used in this study is ANSYS FLUENT. Three dimensional, steady, compressible Reynolds-Averaged Navier-Stokes equations with k-ε turbulence model were solved by using finite volume method to calculate flow field around the missile.

3.1.2 Comparison of the Aerodynamic Loads

In this part, CFD and engineering level codes were used to predict the aerodynamic characteristics of the body-strake configuration D57 at supersonic flow conditions. Results obtained were compared with existing experimental values. It was shown that CFD is consistent with the experimental results and can be used for the optimization problem. Total of 20 cases were solved for flight conditions shown in the Table 3.2.

Table 3.2 The flight conditions for D57 test case

Mach Number	2.01, 2.8, 3.98
Angle of attack (α)	0°, 5°, 10°, 15°, 20°, 25°, 30°
Roll orientation, phi (ϕ)	0°, 45°

The pressure contour slices at distinct locations along the body-strake and body alone configurations for D57 strake are shown in Figure 3.5 . Looking at the slices, it can be stated that the pressure difference between upper and lower surfaces increase with the increasing location along the strake panels. Clearly, the long chord surfaces create a substantial pressure difference between the upper and lower flow fields along the strake fins.

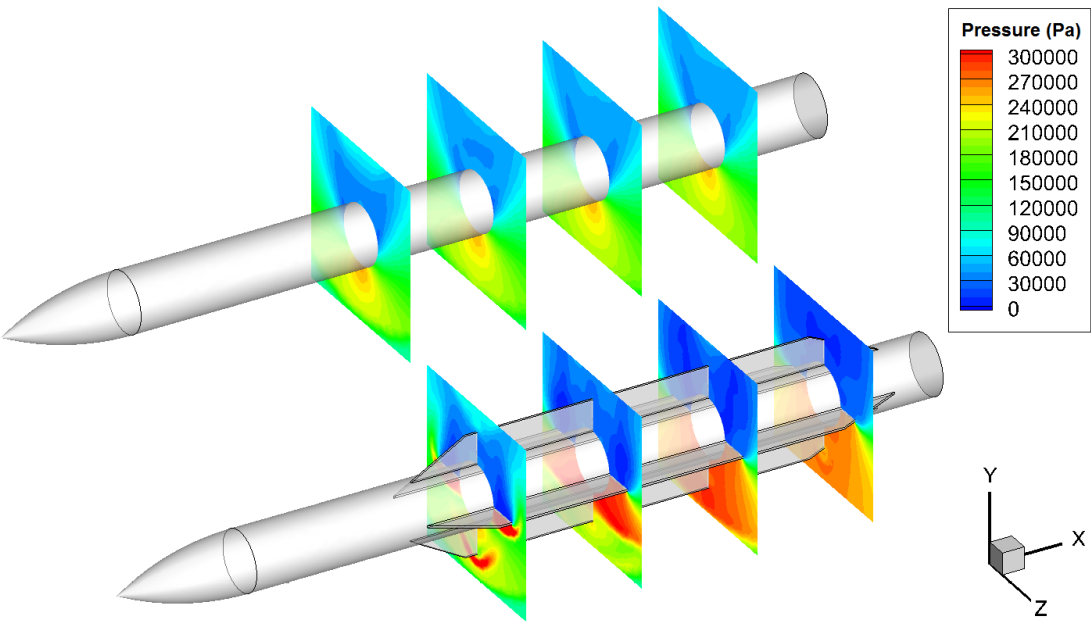


Figure 3.5 The pressure contours slices along the body alone and body-(D57) strake configuration

The Missile DATCOM 1997, the Navier-Stokes solution, the Missile DATCOM 2009, the White’s Method and experimental results are presented in Figure 3.6 through Figure 3.17 at following conditions

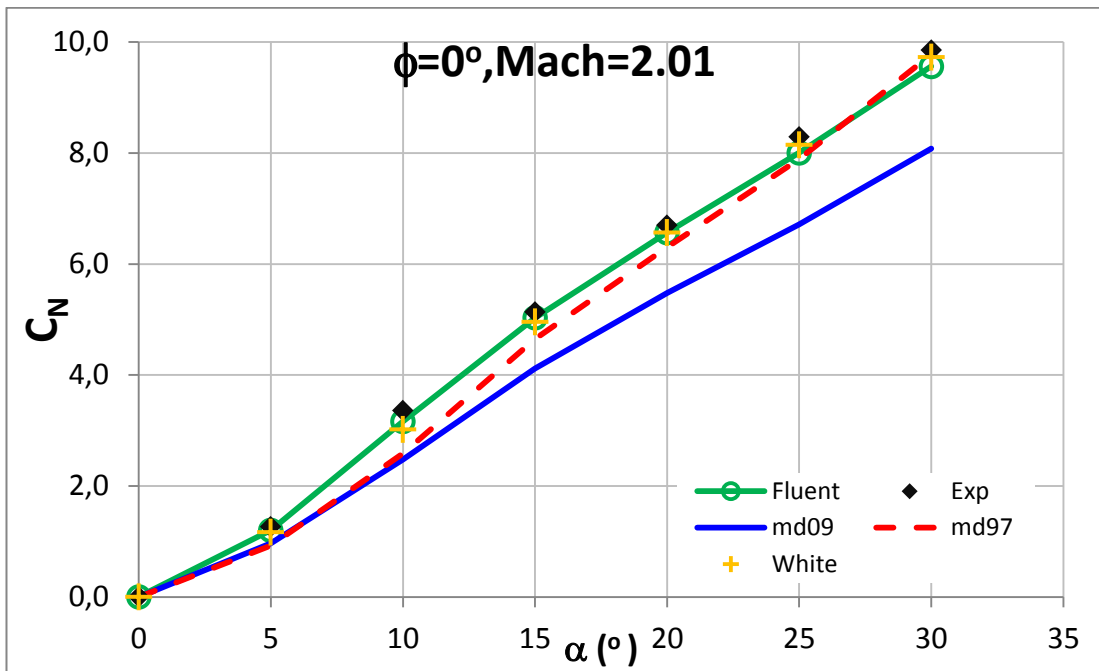


Figure 3.6 Normal Force coefficient of the Strake Unit (D57) with Angle of Attack (Mach=2.01, $\phi=0^\circ$)

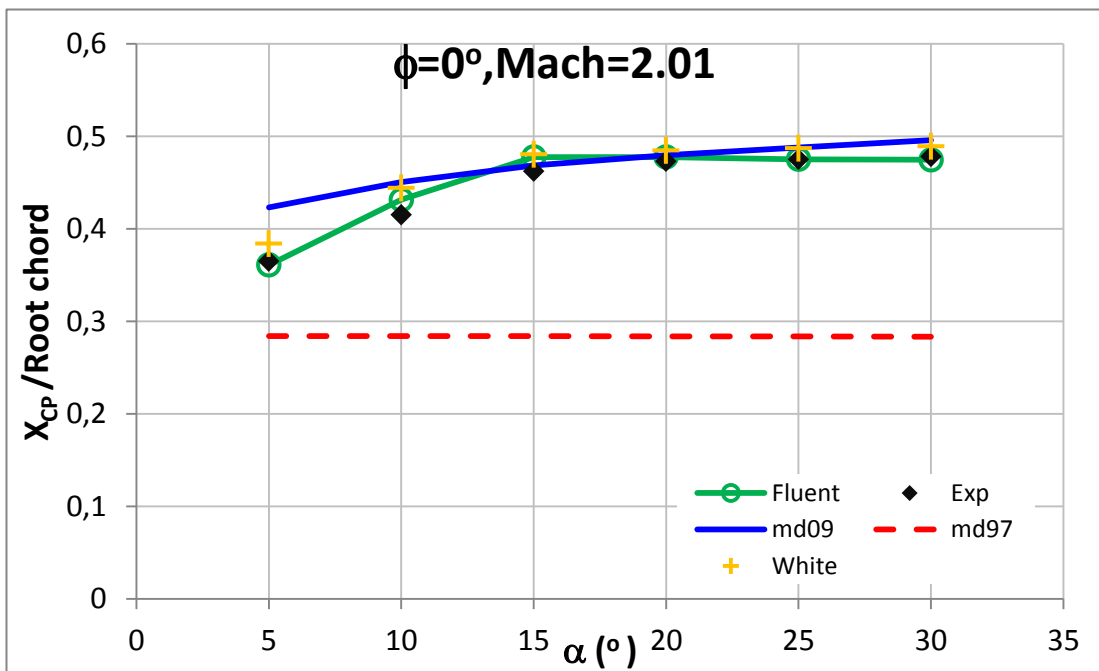


Figure 3.7 Center of Pressure of the Strake Unit (D57) with angle of attack (Mach=2.01, $\phi=0^\circ$)

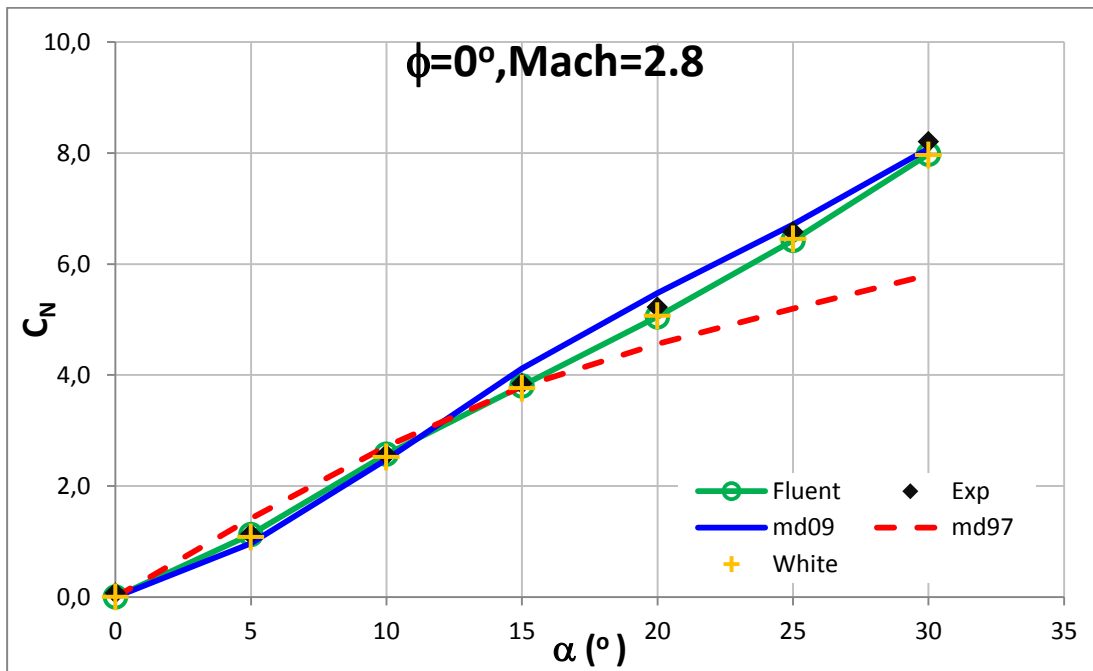


Figure 3.8 Normal Force coefficient of the Strake Unit (D57) with Angle of Attack (Mach=2.8, $\phi=0^\circ$)

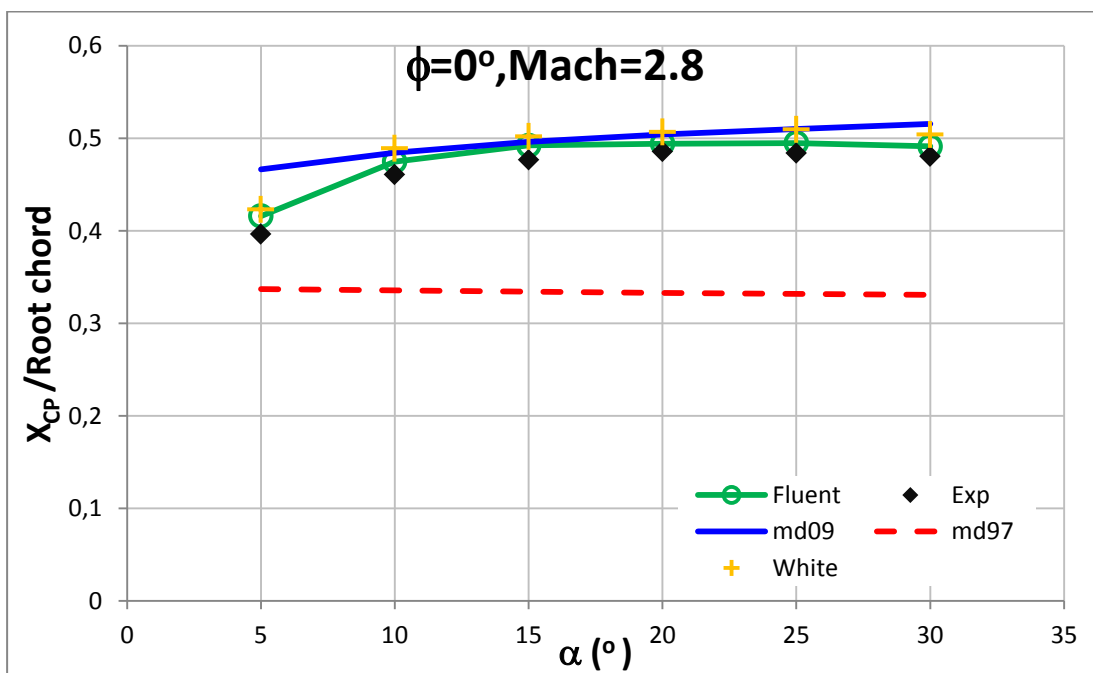


Figure 3.9 Center of Pressure of the Strake Unit (D57) with angle of attack (Mach=2.8, $\phi=0^\circ$)

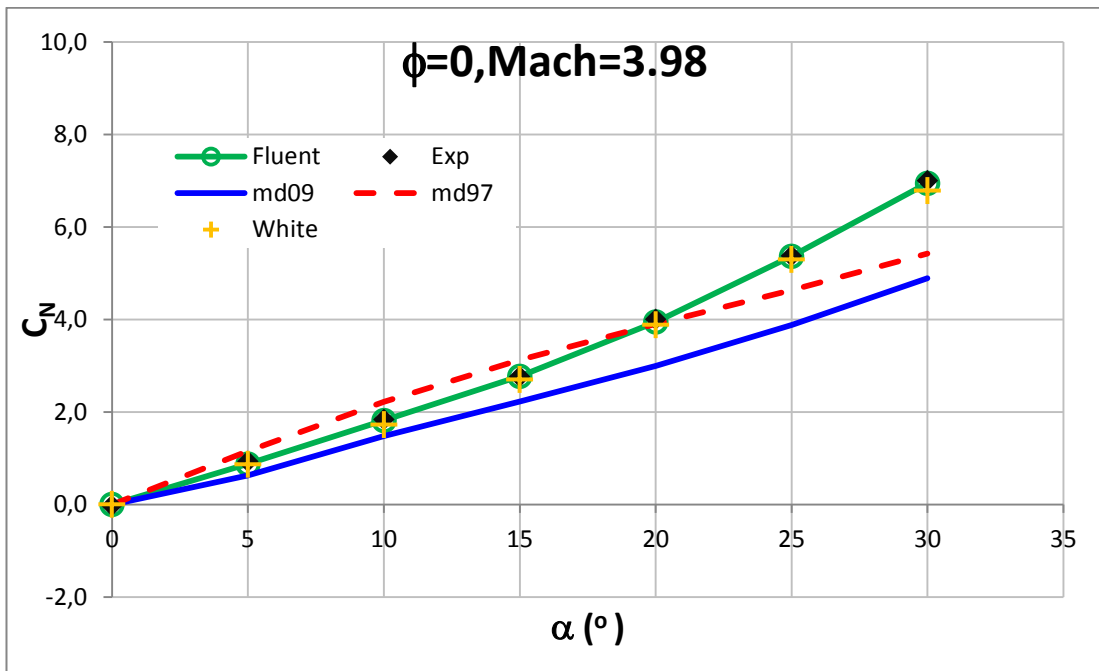


Figure 3.10 Normal Force coefficient of the Strake Unit (D57) with Angle of Attack (Mach=3.98, $\phi=0^\circ$)

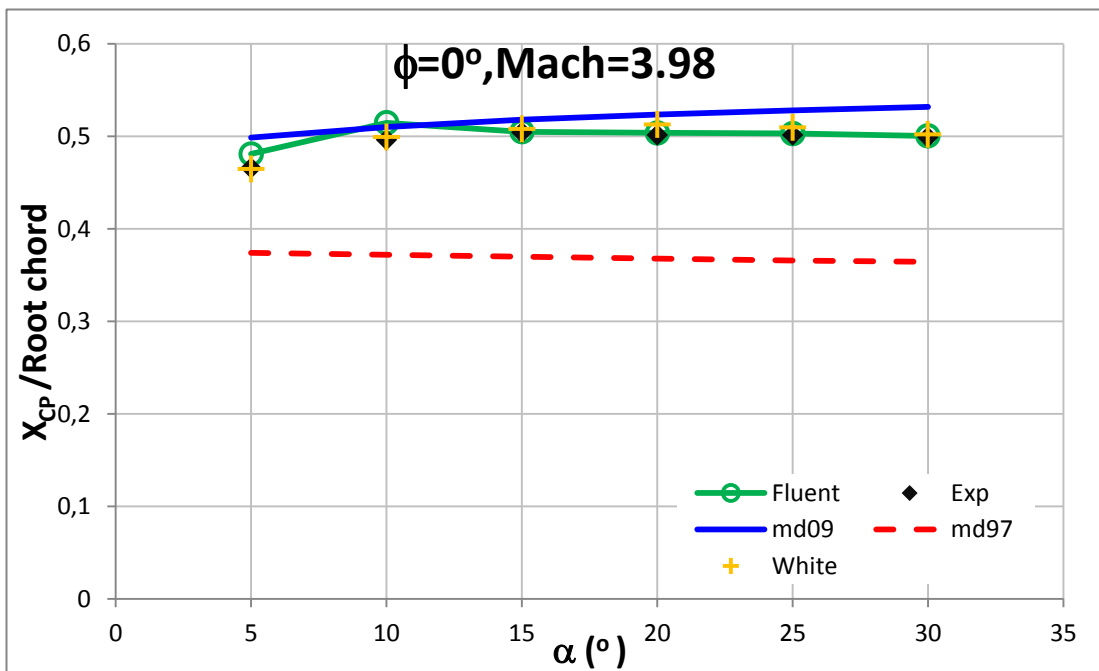


Figure 3.11 Center of Pressure of the Strake Unit (D57) with angle of attack (Mach=3.98, $\phi=0^\circ$)

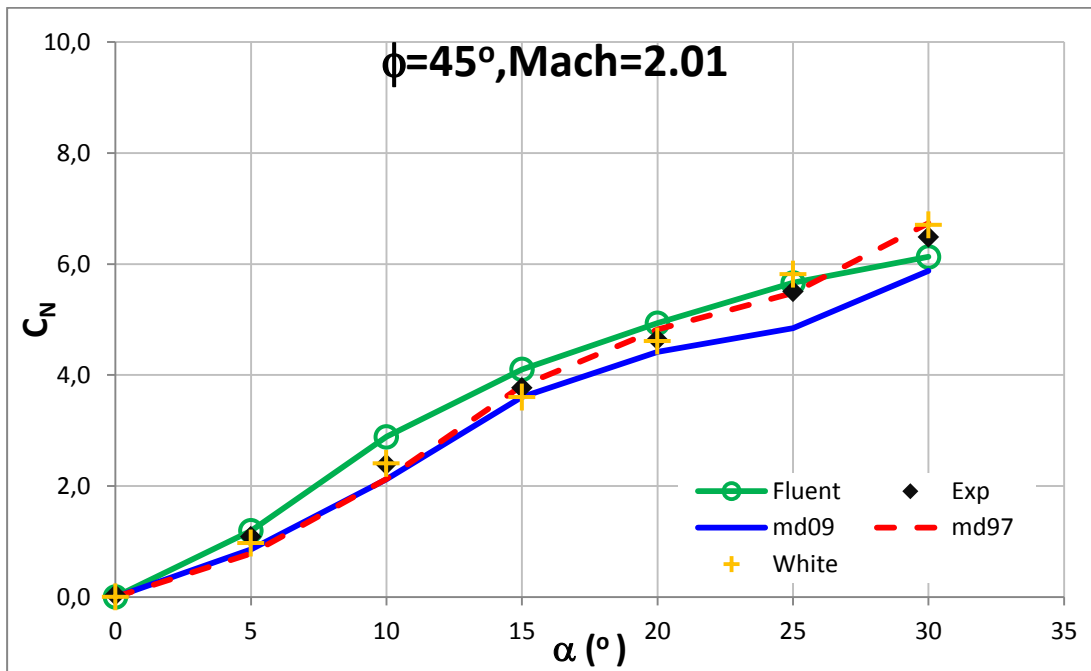


Figure 3.12 Normal Force coefficient of the Strake Unit (D57) with Angle of Attack (Mach=2.01, $\phi=45^\circ$)

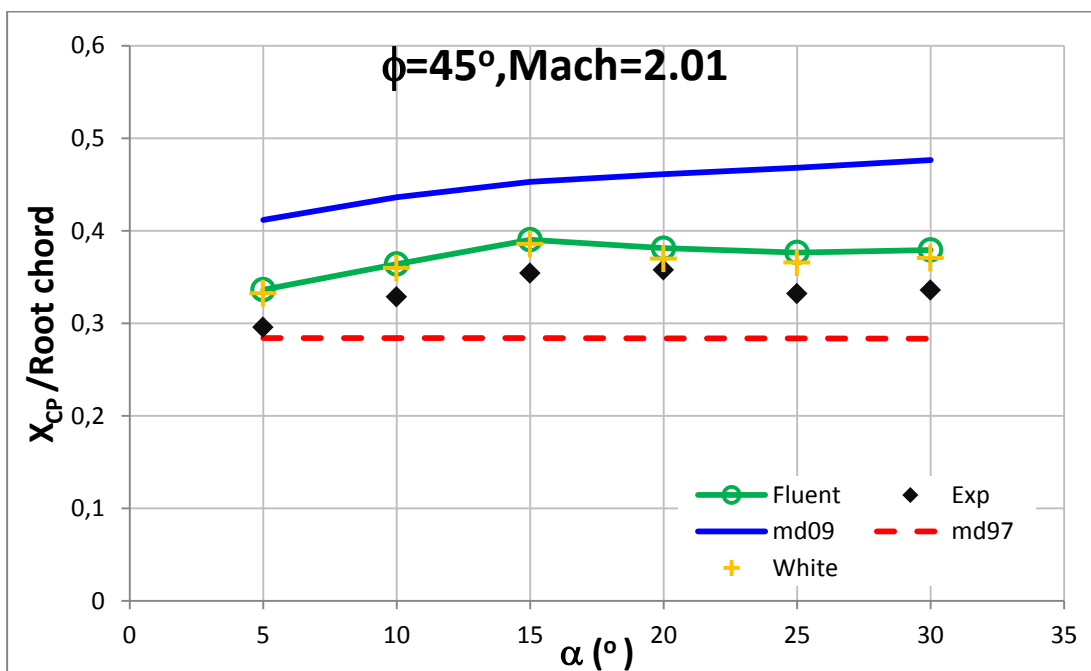


Figure 3.13 Center of Pressure of the Strake Unit (D57) with angle of attack (Mach=2.01, $\phi=45^\circ$)

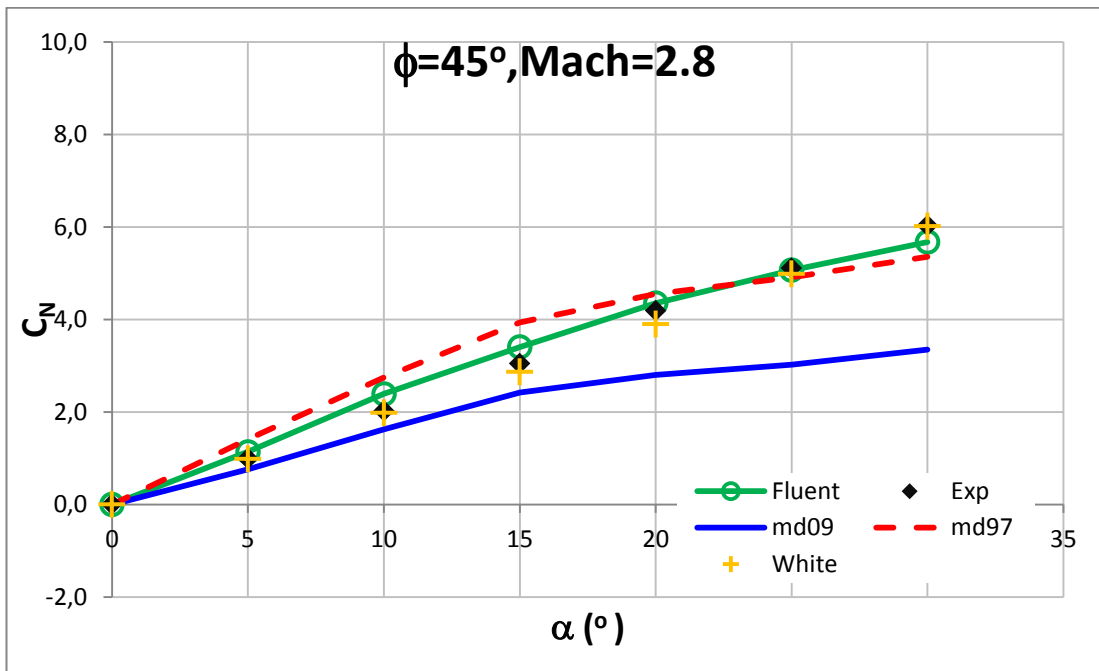


Figure 3.14 Normal Force Coefficient of the Strake Unit (D57) with Angle of Attack (Mach=2.8, $\phi=45^\circ$)

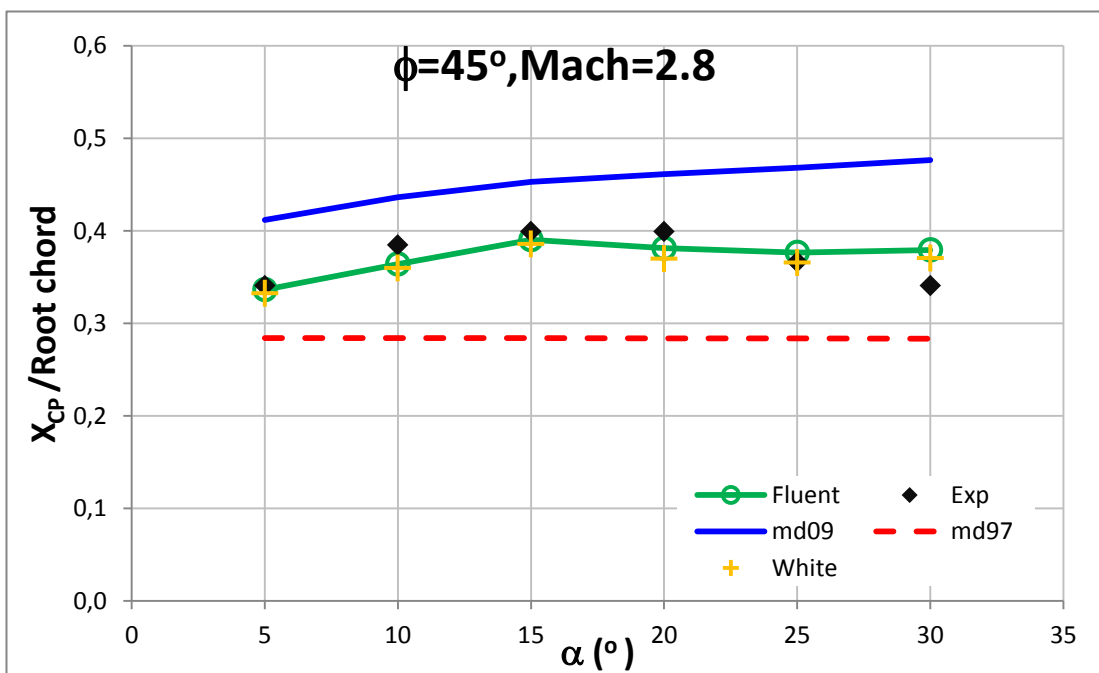


Figure 3.15 Center of Pressure of the Strake Unit (D57) with angle of attack (Mach=2.8, $\phi=45^\circ$)

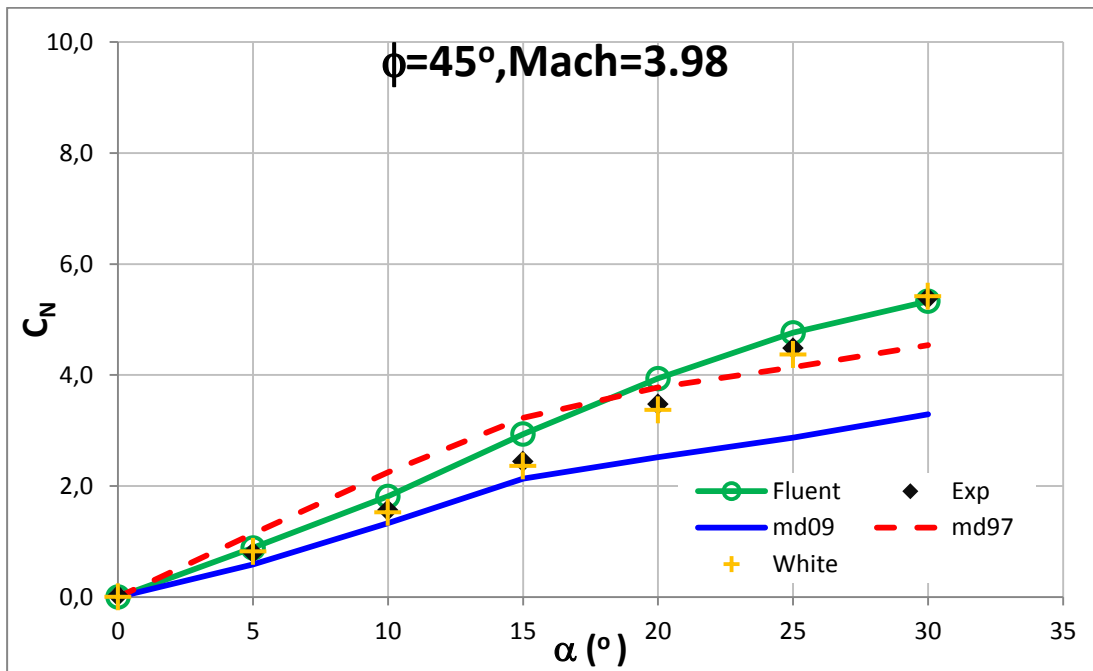


Figure 3.16 Normal Force Coefficient of the Strake Unit (D57) with angle of attack (Mach=3.98, $\phi=45^\circ$)

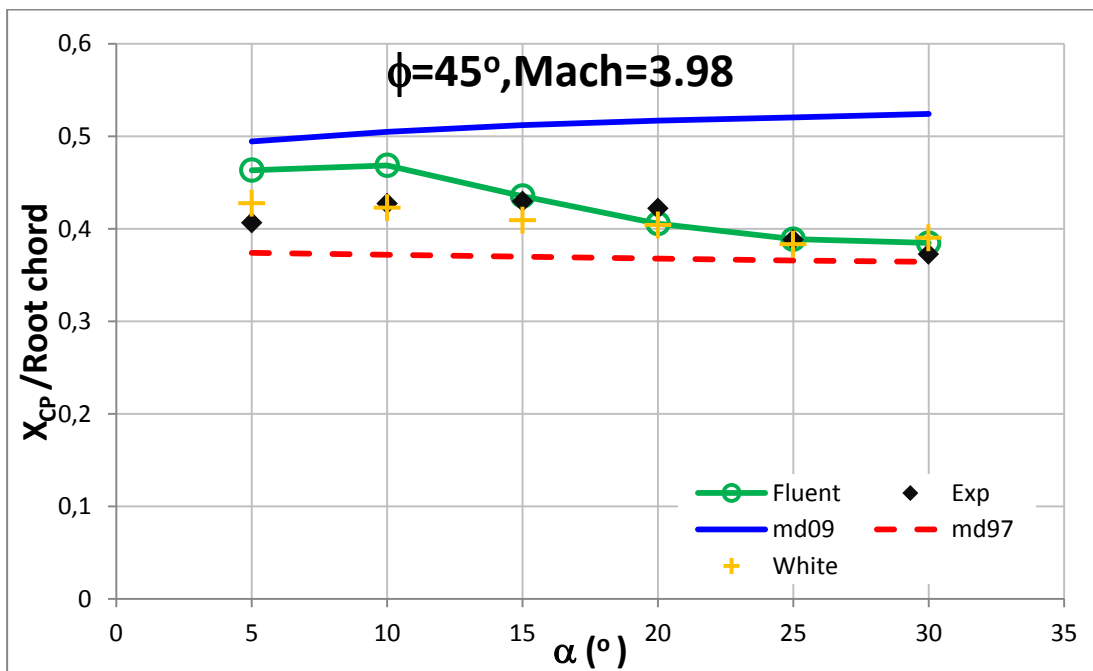


Figure 3.17 Center of Pressure of the Strake Unit (D57) with angle of attack (Mach=3.98, $\phi=45^\circ$)

The results are shown above. From the figures it can be derived that, White's method and Reynolds-Averaged Navier Stokes (CFD) method are very good for predicting the normal force and center of pressure of the strake unit for this configuration.

CFD results are in a very good agreement with the experimental results for the center of pressure variation with angle of attack. Only for Mach 3.98 at small angles of attack, there exists a small difference between the experimental and CFD results.

In Missile DATCOM 97, the variation of the center of the pressure of the strake unit in the body presence is constant with angle of attack. This is mainly due to the fact that Missile DATCOM 97 does not consider separate components of the normal force (linear and nonlinear terms). By taking into account linear and nonlinear contributions to the normal force and by taking into account the fin location on the body, Rosema developed an empirically based methodology to improve the center of pressure location [32].

Missile DATCOM 2009 results have changing accuracy. In only very few cases DATCOM results are in very good agreement with the experimental results. It is relatively good for center of pressure estimation at zero roll orientation compared to other Missile DATCOM 2009 results.

Even though there is improvement in Missile DATCOM version 2009, still it is not good enough and does not have the robustness of the White's method and Navier-Stokes method. Since the test case was taken from White's study, White's method should be further explored to evaluate its applicability.

Using the body alone, strake alone and body-strake CFD solutions, a component force breakdown is carried out at Mach 2.01. In the body-strake CFD solutions, zonal forces of the strake and body which are strake in the presence of the body and body in the presence of the strake are also checked. Body force increment is found by subtracting body alone results from body in the presence of strake results. Strake force increment is calculated by subtracting strake alone results from the strake in the presence of body results. The component force breakdown is shown in Figure 3.18.

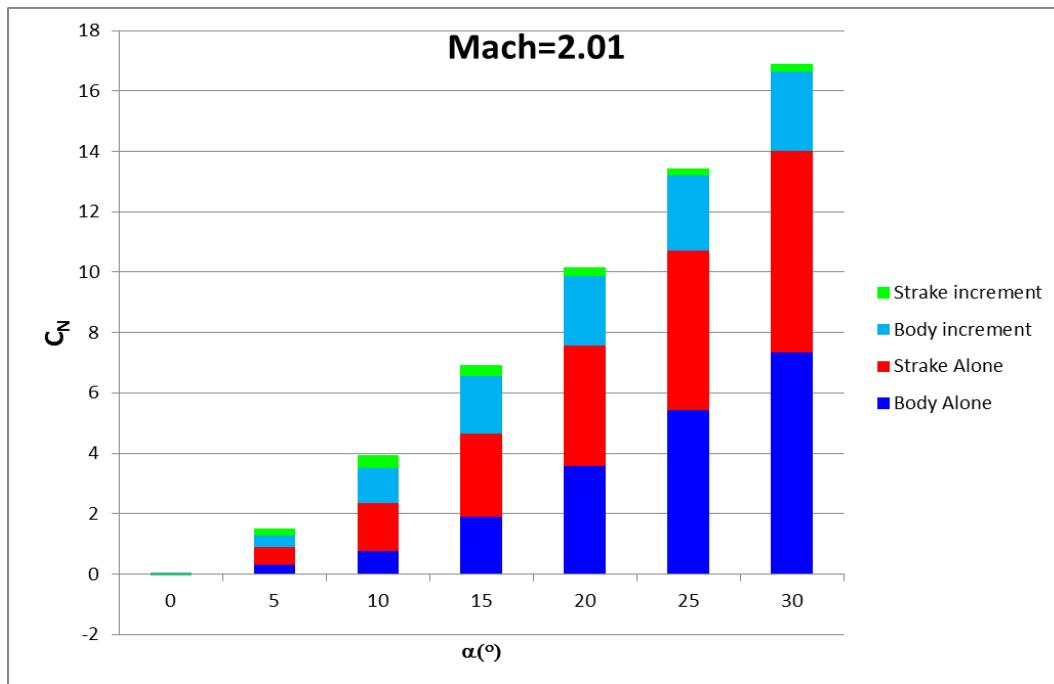


Figure 3.18 The breakdown of the Interference and Component Normal Forces

The results suggest that, the body and strake alone form up the main part of the total forces produced. In addition, body incremental force due to interference with very low aspect ratio fins is very important with respect to the strake incremental force for this body-strake configuration and its amount increases as the angle of attack increases. This proves the importance of the vortex lift mentioned in first chapter.

Body-strake interference effects on aerodynamic coefficients are investigated.

As the distance from the tip of the chord increases, the pressure difference between upper and lower surfaces of the strake unit gets larger.

The normal force increment of the body due to interference effects is larger compared to the normal force increment of the strake unit due to interference with the body. This implies that the vortices shed on the body along the strake chord adjacent to the body increase the body normal force.

White's method and CFD methods seem to be powerful in estimating the normal force and center of pressure of the D57 strake configuration. DATCOM is not very

good at estimating the center of pressure and normal force of the strake unit despite the improvement. Since limited in application and test case was taken from White's study (further research is necessary), the CFD is selected as the optimization tool.

3.2 Optimization Studies

In this part, the optimization studies for reducing coupling of pitching moment from sideslip plane are presented. Initially, a gradient based optimization algorithm (steepest descent) with line search is used. It is shown that the steepest descent algorithm converges to local solution. Since gradient method is trapped in the local solution, gradient based optimization is not suitable for this problem. Therefore, a stochastic optimization method, namely Particle Swarm Optimization method is employed to search for the global solution.

The computation time was approximately 12.5 days for PSO while only 2.5 days was enough for gradient method with a computer having 16 Intel XEON E5520 2.27 GHz processors with each including 4 cores. Each CFD run was performed using 8 cores and each CFD run took approximately 2.5 hours.

3.2.1 Aerodynamic Performance Optimization Problem

The geometrical sizing parameters and leading edge location of the strake planform used in the optimization process are shown in the figure below. Root chord length and span length of the strake are geometrical sizing parameters while leading edge location (XLE) is the parameter showing placement of the strake measured from the nose tip. The tip chord is calculated by keeping the sweep angles at the leading and trailing edges constant. The missile fins were placed in cross orientation in the optimization studies. The representative geometry is shown in Figure 3.19 for plus orientation. The certain interval limits on the span length, chord length and leading edge location are imposed. The body geometry taken from D57 and the added tail geometry are kept constant.

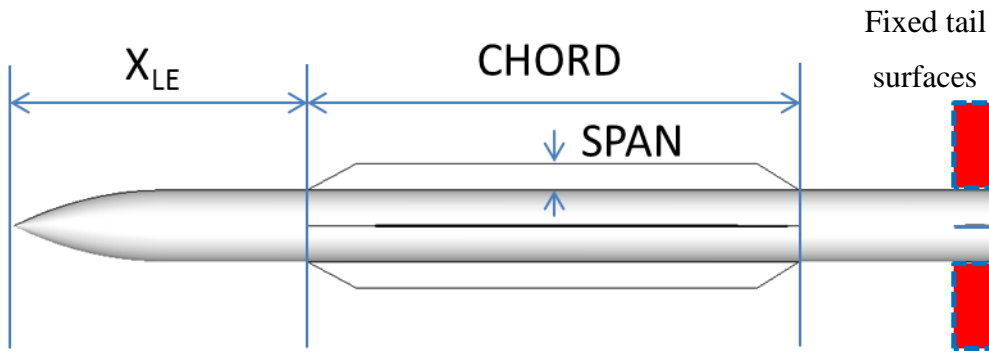


Figure 3.19 Strake planform and location parameters (+ view)

The whole design space geometric parameters are limited in the following range shown in the table below. The configurations out of this range are elected without evaluation, avoiding unnecessary runs:

Table 3.3 The limits of geometrical parameters

Geometric Parameter	Minimum (cm)	Maximum (cm)
Chord	70	272
Span	6	20
Leading edge from nose	75	275

The objective function (f) of the optimization is stated below as sum of two functions:

$$f_1 = (C_{m_{\alpha,\beta=10}} - C_{m_{\alpha,\beta=5}})^2, \alpha = 8^\circ, M \quad (3.5)$$

$$\text{if } SM < 1 \text{ or } SM > 1.2$$

$$f_2 = (SM \cdot 10 - 11)^2 \quad (3.6)$$

$$\text{if } 1 < SM < 1.2 \quad f_2 = 0$$

$$f = f_1 + f_2 \quad (3.7)$$

In the above equations the definitions of the objective function for minimization problem is given. It must be noted that the static margin is used as the controlling

parameter with the aim of keeping it in between 1.0 and 1.20. If the static margin is out of this range it adds positive value to the objective function proportional to the square of the distance to this range, reducing the chance of the configurations to be selected as optimum. Meanwhile, it is mainly aimed that change of the pitching moment with sideslip is minimized as seen from the equation for the first term of the objective function.

For objective function evaluation, the difference between the two pitching moment values at sideslip angles of 5 and 10 degrees are considered. The square of this value forms the first part of the objective function. If the static margin takes values between 1.0 and 1.2, the static margin makes no effect on the objective function. However, if it is out of this range, square of ten times its distance to the center of this interval is added to the objective function, causing an increase in the objective function. These two parts of the objective function are added to ensure satisfying both objective functions simultaneously.

The aerodynamic optimization problem was solved both by a stochastic and a gradient based optimization method. The aerodynamic coefficients for two sideslip angles were obtained by using CFD solver. The aerodynamic performance parameters were calculated from the aerodynamic coefficients. The aerodynamic performance parameters were used as inputs to the objective function calculation.

The iterations for both CFD based PSO and gradient optimization (Steepest Descent with Line Search) were run, in which the planform geometry and position of the strake fins on the body from the nose were changed during iterations, aiming to reduce asymmetric loading on pitching moment due to sideslip while keeping static margin between 1 and 1.2. The geometry of the tail and the body were kept constant during optimization iterations and center of gravity for the whole configuration is 235 cm from the nose.



Figure 3.20 Baseline missile geometry (+ view)

The baseline missile geometry is shown in the above figure which is variant of the D57 missile analyzed in the validation chapter. The center body of the baseline missile is the same as D57 missile. The aerodynamic performance of the baseline missile will be compared with the optimum missile geometry that will be obtained at the end of the iterations.

3.2.2 Gradient based Optimization

In this part, the results of the gradient based optimization are presented. The calculation steps of gradient based optimization can be found in the Appendix part. The gradient based optimization is continued for four iterations. In iteration 1, span length gets out of limits, and therefore in iteration 2 the length of the span is fixed; in both steps, change of the objective function during line search is plotted. In iteration 3 the span is used again as design parameter. In iteration 4, the span length is again removed due to ending in out of limits again.

3.2.2.1 Variation of the Objective Function in Gradient Based Optimization

In Figure 3.21 the change of the objective function during the first line search step is shown.

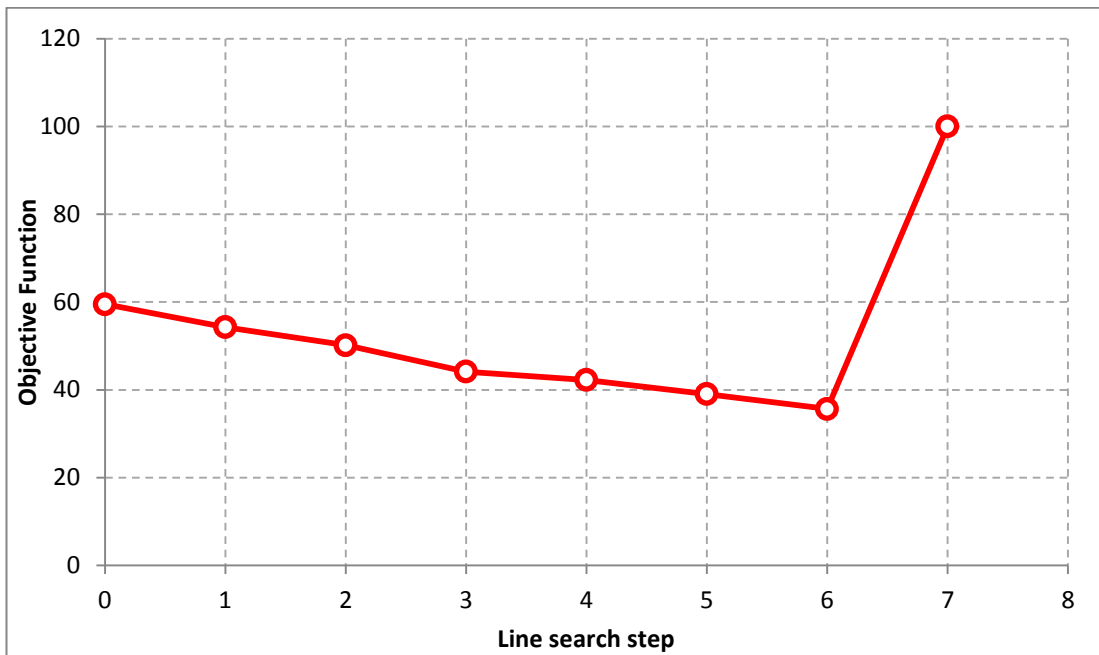


Figure 3.21 Variation of the objective function during line search in iteration 1

At iteration 1, span ended in out of limits as shown in Figure 3.23, therefore, by fixing the span, the second step is continued with two parameters. The change of the objective function during the line search in iteration 2 is shown in the Figure 3.22.

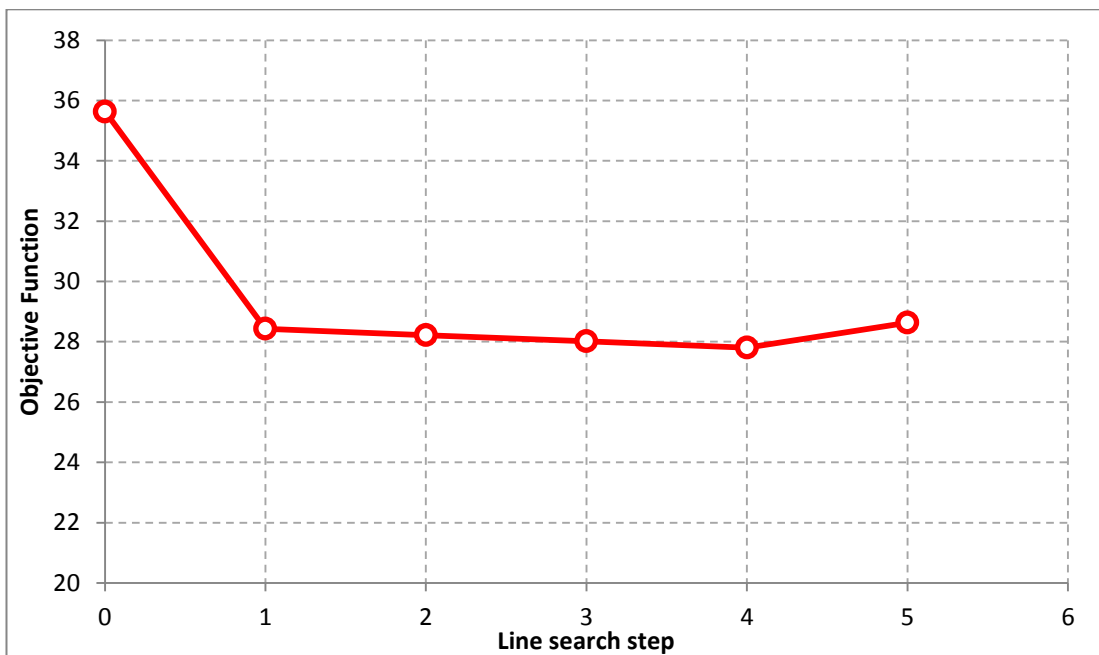

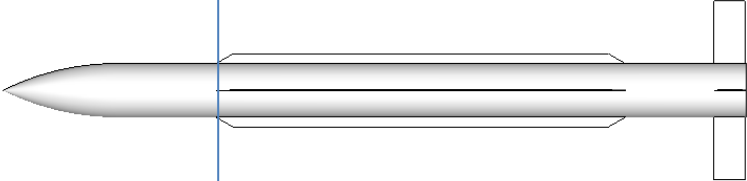
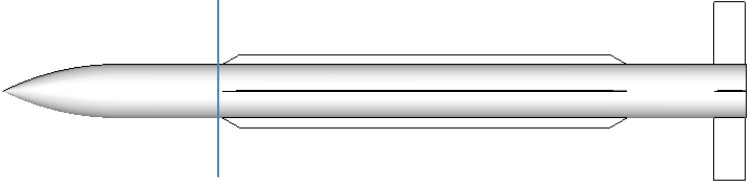


Figure 3.22 Variation of the objective function during line search in iteration 2

3.2.2.2 Variation of the Configuration in Gradient Based Optimization Iterations

The change of the strake geometry and placement on the body during gradient based optimization iterations are shown in the table below. In Figure 3.23 the variation of the geometrical parameters during the first line search step is shown. As seen in the table, span length of the strake planform gets smaller abruptly. However, there is not much change in the other two parameters during gradient based optimization iterations.

Table 3.4 The strake planform geometry and placement on the body during gradient based optimization iterations (+ view)

Iteration Number	Missile Configuration Geometry
0	
1	
2	

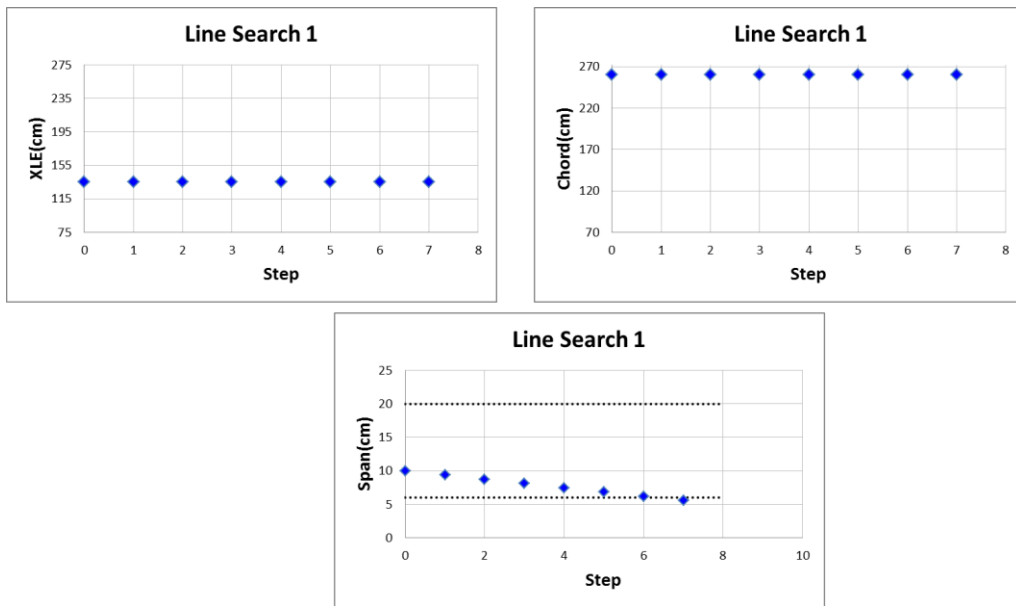


Figure 3.23 Variation of the geometrical parameters during line search in iteration 1

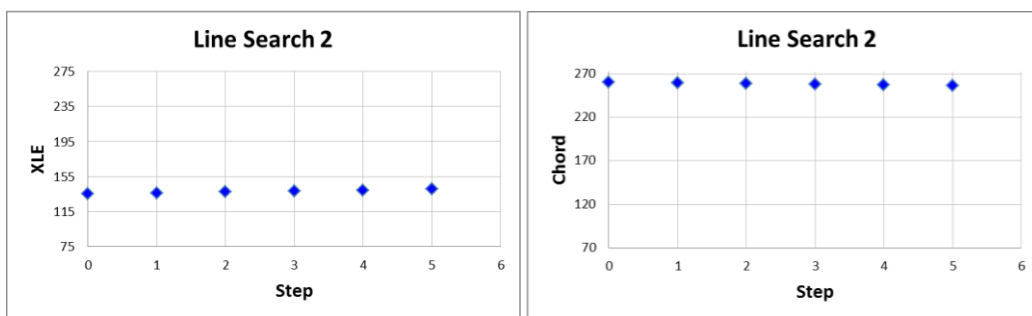


Figure 3.24 Variation of the geometrical parameters during line search in iteration 2

As already mentioned, the length of the span is fixed in iteration 2. However, no substantial changes occur in other parameters in this step.

The gradient based optimization process is finished at iteration 4, but the best solution is obtained in iteration 2. In iteration numbers 3 and 4 the line search cannot proceed and ends immediately at first step. The obtained geometry is shown in the figure below.



Figure 3.25 The optimum strake planform geometry and placement obtained by gradient optimization (+ view)

3.2.3 Particle Swarm Optimization

In this CFD based PSO study, the strake design optimization study lasted for 49 iterations. The population consisted of five members, which needed to be chosen small due to high computational demand. In each step, by tunneling around each member of the population, four configurations are meshed in Gambit with the help of the automatic meshing scheme developed and the performance parameters are evaluated by using ANSYS FLUENT solver. This means that if there is no configuration elected due to geometric restriction or, repeating value, 20 configurations are evaluated at each iteration step. The total number of configurations evaluated counts to 575, which is not 49 multiples 20, due to the code block which is checking repetitiveness and geometric restrictions.

The best configuration is reached in 38 iterations, and 439 function evaluations are performed until this iteration. At the remaining iterations a better configuration cannot be found. In the following 11 iterations, there is no configuration better than the reached configuration in 38th step. Although the number of evaluations seems to be too many for such a high computationally demanding problem, with an initial insight into problem and good baseline selection, the solution time can be improved. In this problem only limits on the dimensions are imposed.

There were four configurations evaluated in each tunneling. Two CFD analyses were performed for each missile configuration corresponding to two sideslip angles of 5 and 10 degrees.

In this part, the PSO was performed by using CFD to obtain aerodynamic coefficients. In the APPENDIX B, the Missile DATCOM 2009 is used to evaluate the aerodynamic coefficients and the results of the optimization study are compared with the results obtained in this chapter. It is shown in APPENDIX B that optimization study by Missile DATCOM 2009 converges to a different configuration than the CFD based optimization.

3.2.3.1 Variation of the Objective Function in PSO Iterations

In this section, the variation of the objective function for the current best missile configuration during optimization iterations is presented. As seen in Figure 3.26 the objective function continually decreases during the iterations

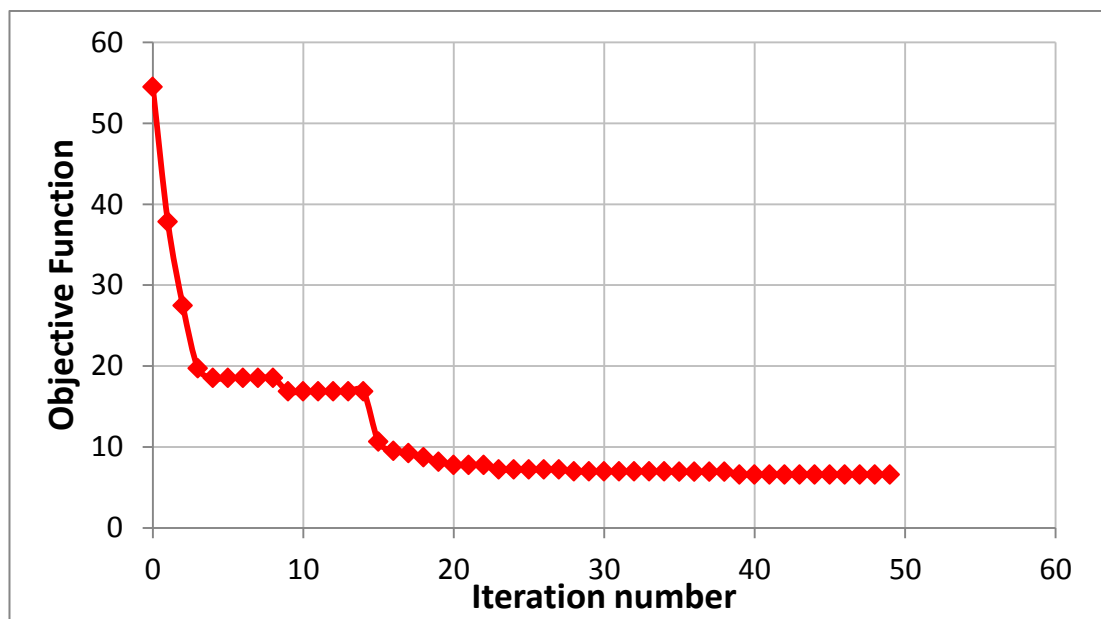
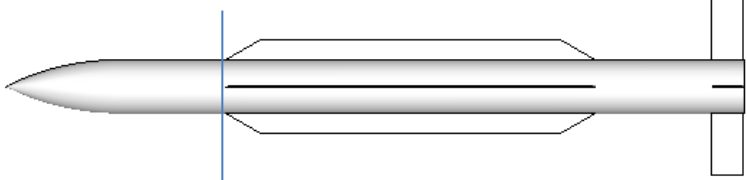
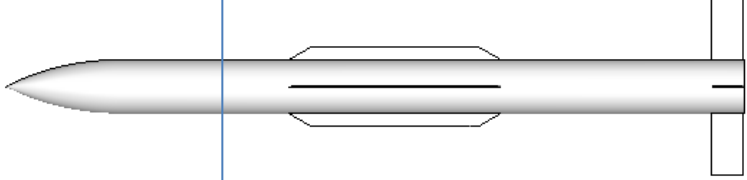
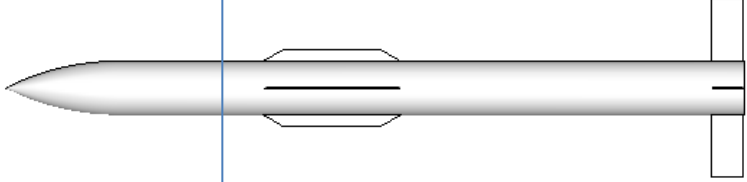
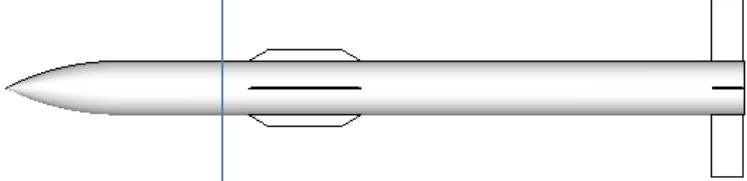
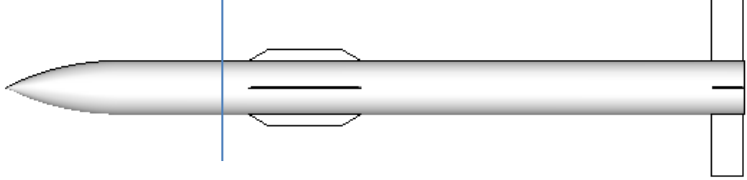


Figure 3.26 Objective function during PSO iterations

3.2.3.2 Variation of the Configuration in PSO Iterations

The change of the strake geometry and placement on the body during PSO iterations are shown in the table below. As seen in the table, the location of the leading edge of the strake moves back and forth with iterations and the size of the strake planform gets smaller. At the end of the iterations, a small strake structure placed in the front part of the missile body is obtained.

Table 3.5 The strake planform geometry and placement on the body during PSO optimization iterations (+ view)

Iteration Number	Missile Configuration Geometry
1 (Baseline)	
10	
20	
30	
38 (Optimum)	

In Figure 3.27, the change of the leading edge on the body as measured from the nose tip is presented. In Figure 3.28 the change of the chord length and, in Figure 3.29 change of the span length of the strake unit is presented. Since the stochastic optimization method is employed, there is a fluctuation in the graphs during iterations.

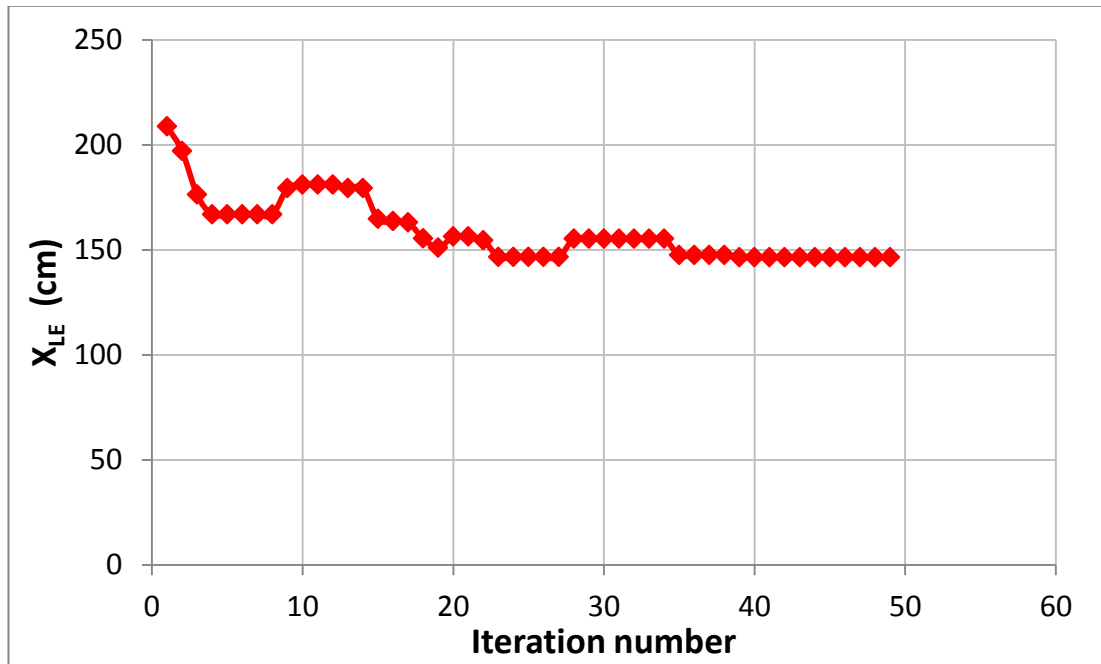


Figure 3.27 Variation of the leading edge location of the strake during PSO iterations

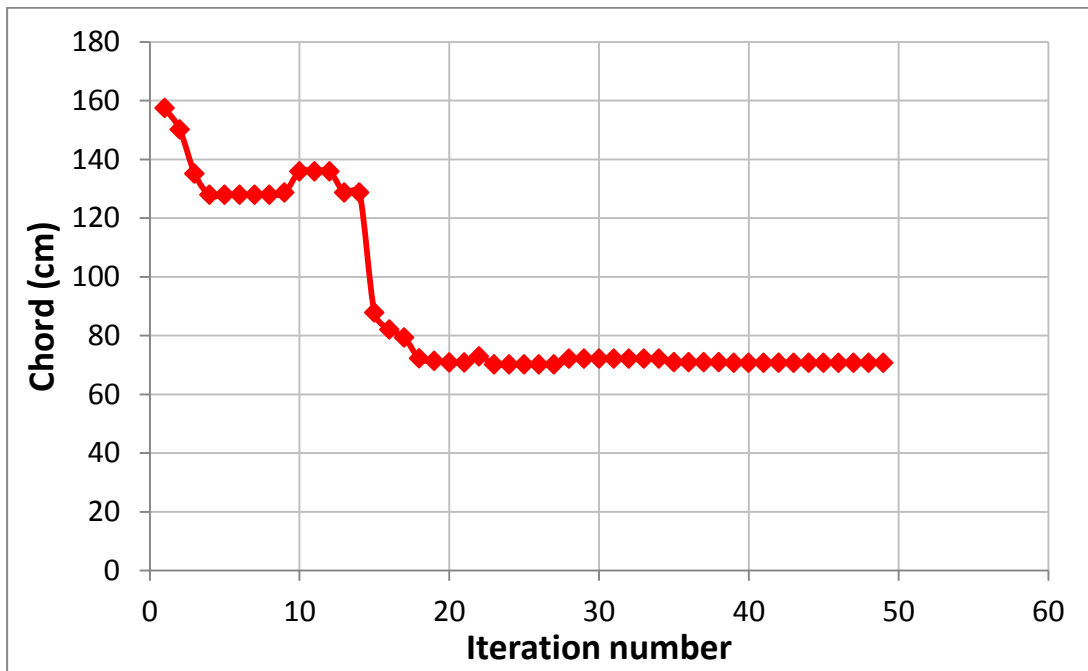


Figure 3.28 Variation of the chord length of the strake during PSO iterations

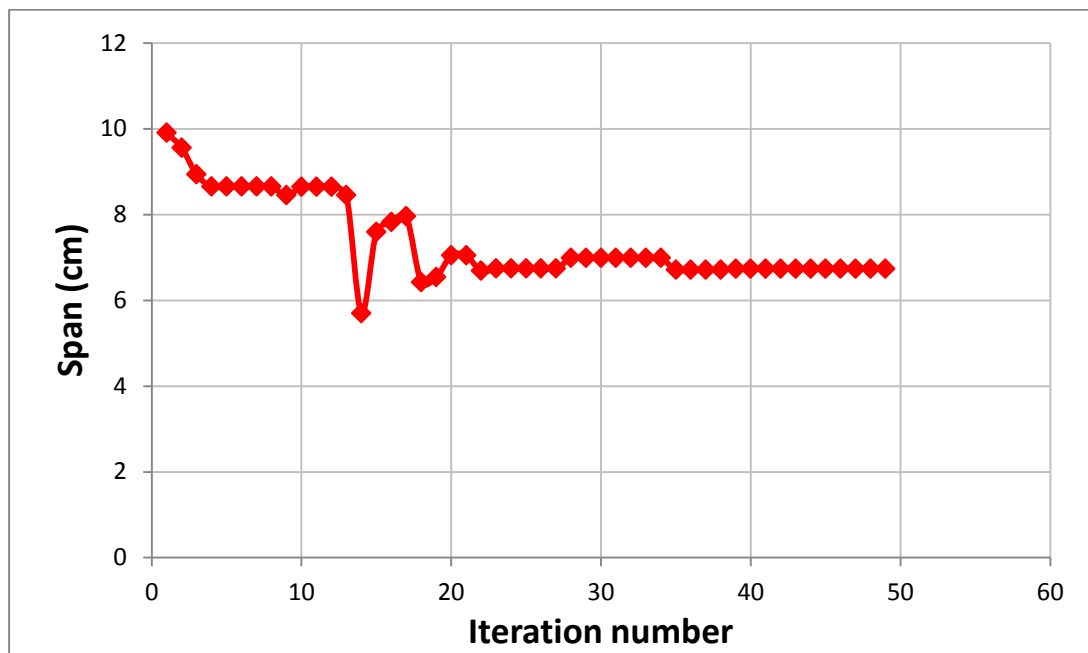


Figure 3.29 Variation of span length of the strake during PSO iterations

3.2.3.3 Variation of the Performance Parameters in PSO Iterations

In this section, the change of the aerodynamic performance parameters and the objective function of the current best missile configuration during optimization iterations are presented. It is seen in figures Figure 3.30 and Figure 3.32 that coupling effect is successfully reduced while static margin is kept in the desired range.

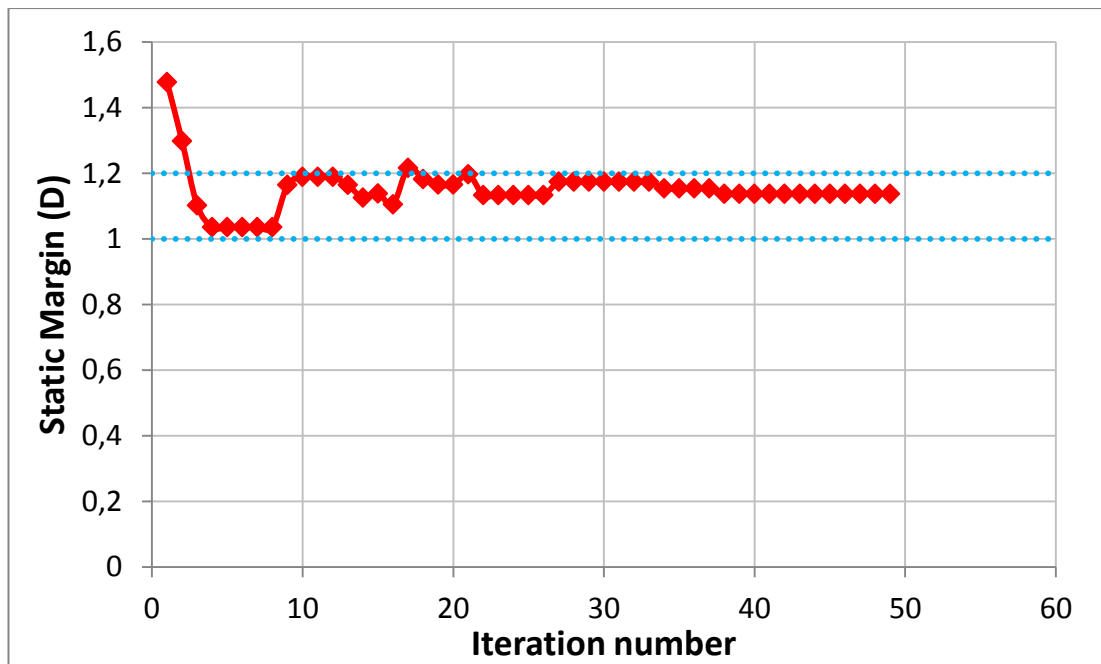


Figure 3.30 Variation of the static margin of the current configuration during PSO iterations

The change of the load factor during PSO iterations is shown in the figure Figure 3.31. In calculation of the load factor in this figure, the weight of the missile was taken 975 kg just to observe how the load factor changes with respect to initial case.

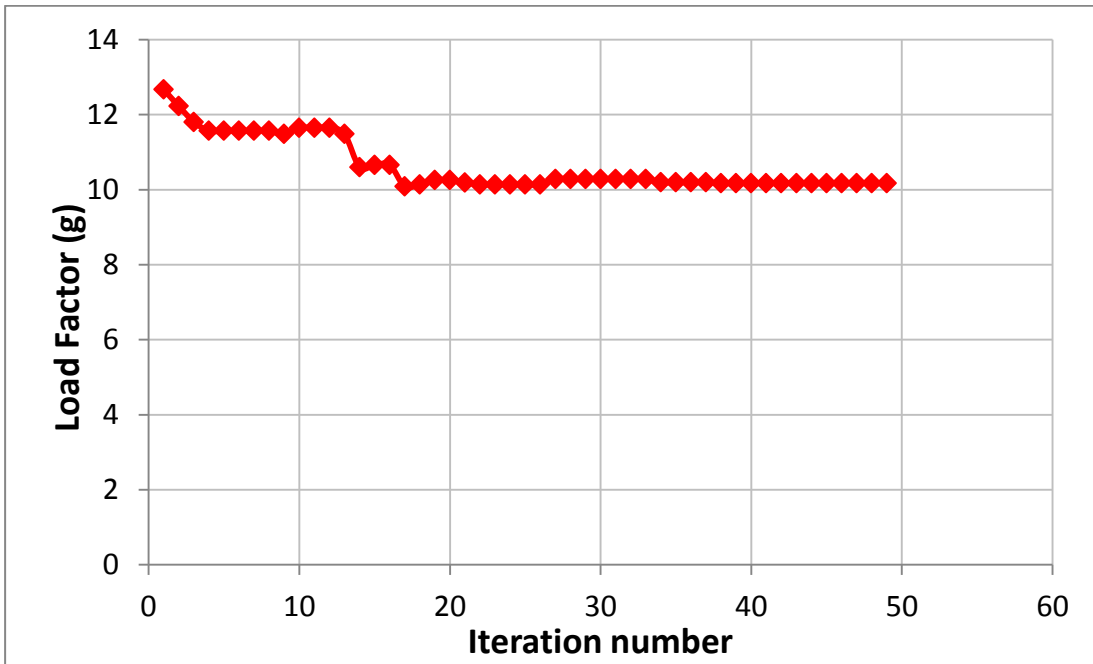


Figure 3.31 Variation of the load factor of the current configuration during PSO iterations

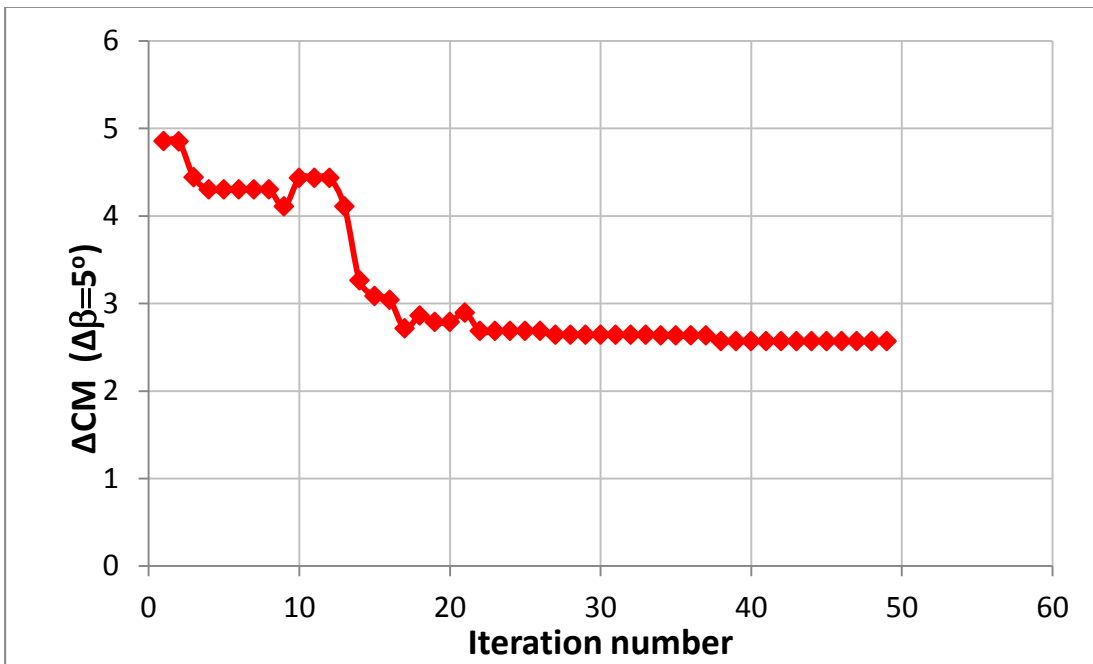


Figure 3.32 Variation of the pitching moment differential with sideslip angle of the current configuration during PSO iterations

3.2.4 Comparison of the PSO with Gradient Optimization

The geometric details of the optimum strake geometry obtained at the end of the PSO iterations are compared with the baseline and gradient method below:

Table 3.6 The comparison of the geometric parameters of the baseline, optimum and gradient solutions

	Chord Length (cm)	Span Length (cm)	Leading Edge Location (cm)
Baseline	236.48	12.63	140.68
Optimum (PSO)	70.86	6.73	146.37
Gradient Solution	256.97	6.16	139.41

The performance parameters for optimum and baseline configurations are compared in table below. The incremental change in the pitching moment with sideslip is reduced to 1/3rd of its starting point by the PSO methodology. The static margin is kept successfully in between 1.0 and 1.2.

Table 3.7 The comparison of the aerodynamic performance of the baseline, optimum and gradient solutions

	ΔCM_{β}	Static Margin [d]
Baseline	7.48	0.64
Optimum (PSO)	2.57	1.13
Gradient Solution	5.27	1.19

According to the results of the gradient optimization, although pitch-yaw coupling is reduced into a small extent, gradient optimization cannot find the global solution of the problem. Gradient method very quickly can detect the span effect, but misses the effect of other parameters. Eventually, it is seen that PSO succeeds in finding global solution. The PSO optimization study was also performed by using Missile DATCOM 2009 in APPENDIX B and it is shown that the optimization with Missile

DATCOM results in a different optimum configuration than CFD based optimization. The findings of the APPENDIX B reinforce our claim with the necessity of the CFD based optimization.

The picture corresponding to the optimum missile-strake configuration with rectangular cross section strake surfaces and modified double wedge cross section tail surfaces is shown in Figure 3.33 in side view. In Figure 3.34, the optimum and baseline configurations are compared in isometric view.

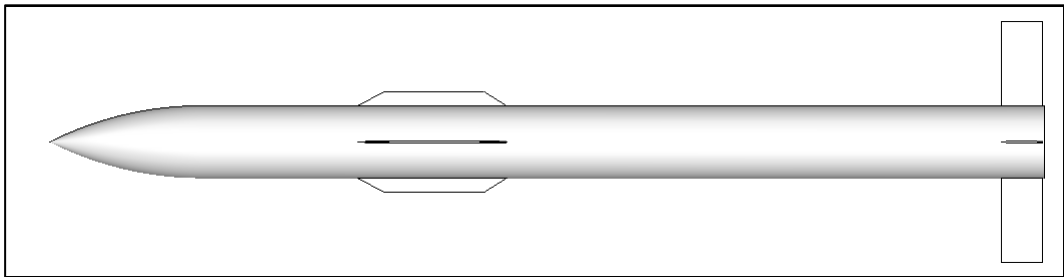


Figure 3.33 Optimum missile strake geometry (+ view)

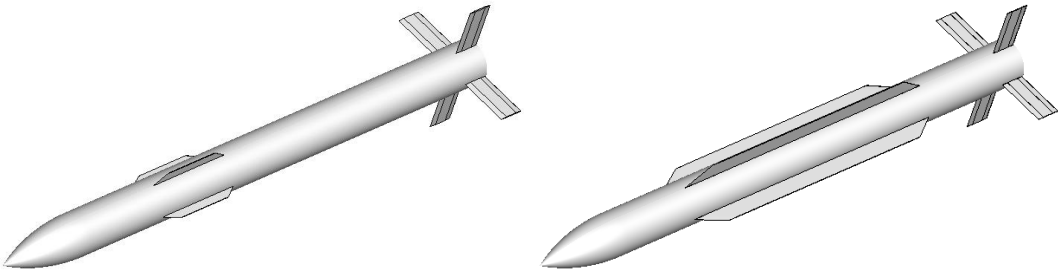


Figure 3.34 Comparison of the optimum and baseline missile body-strake geometries (isometric view)

3.2.5 Comparison of the Optimum and Baseline Configurations

The optimization problem is thus successfully solved. The results of the optimum and baseline configurations are compared in the following figures.

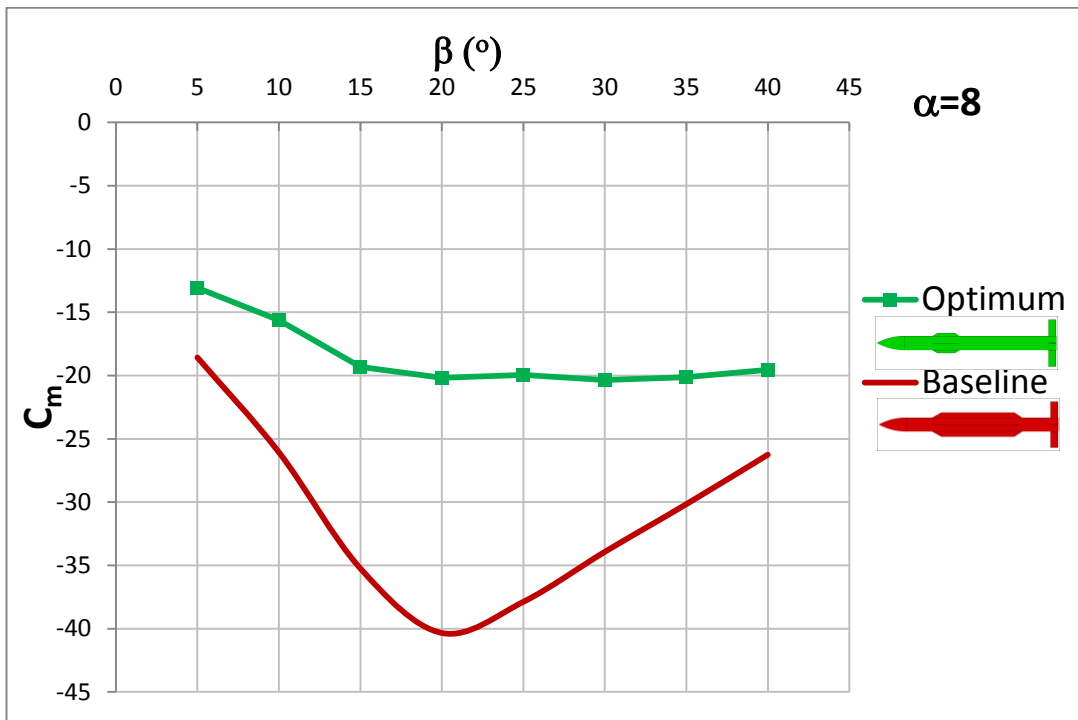


Figure 3.35 The change of the pitching moment coefficient with sideslip angle for the optimum and baseline missile configurations (Mach=2.01)

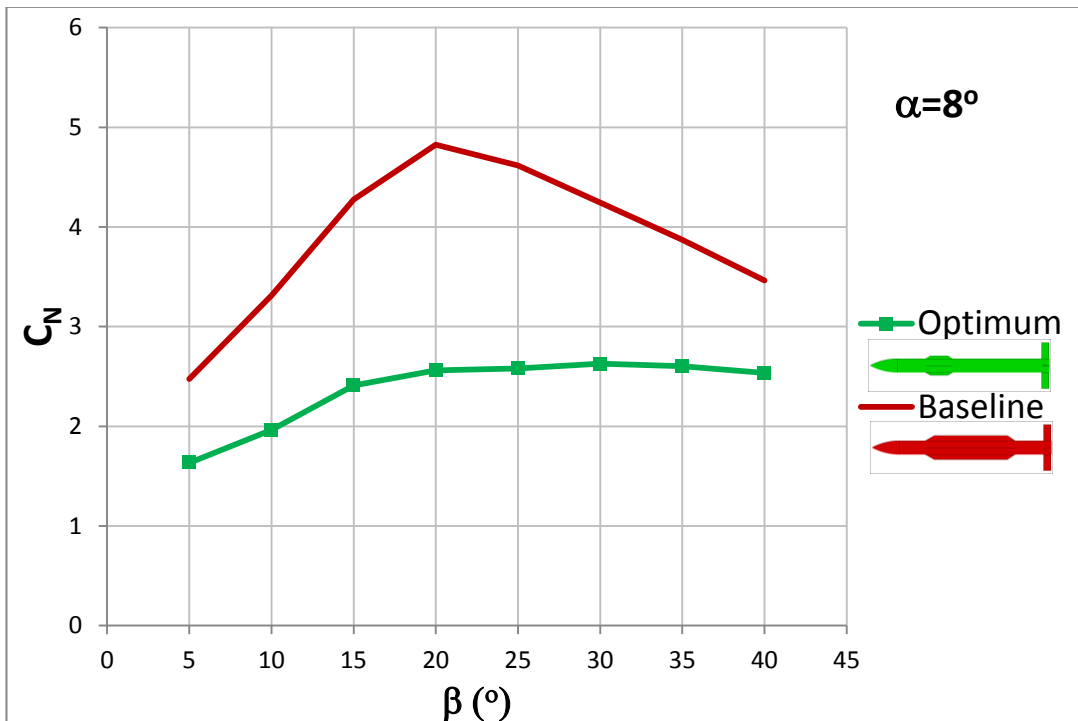


Figure 3.36 The change of the normal force coefficient with sideslip angle for the optimum and baseline missile configurations (Mach=2.01)

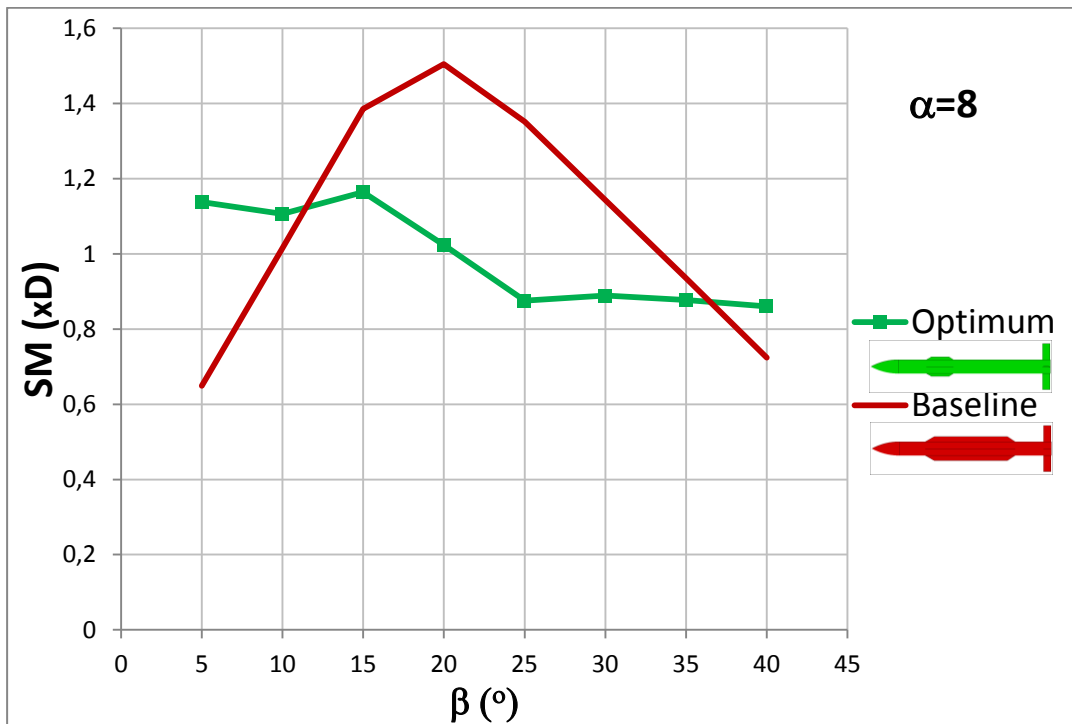


Figure 3.37 The change of the static margin with sideslip angle for the optimum and baseline missile configurations (Mach=2.01)

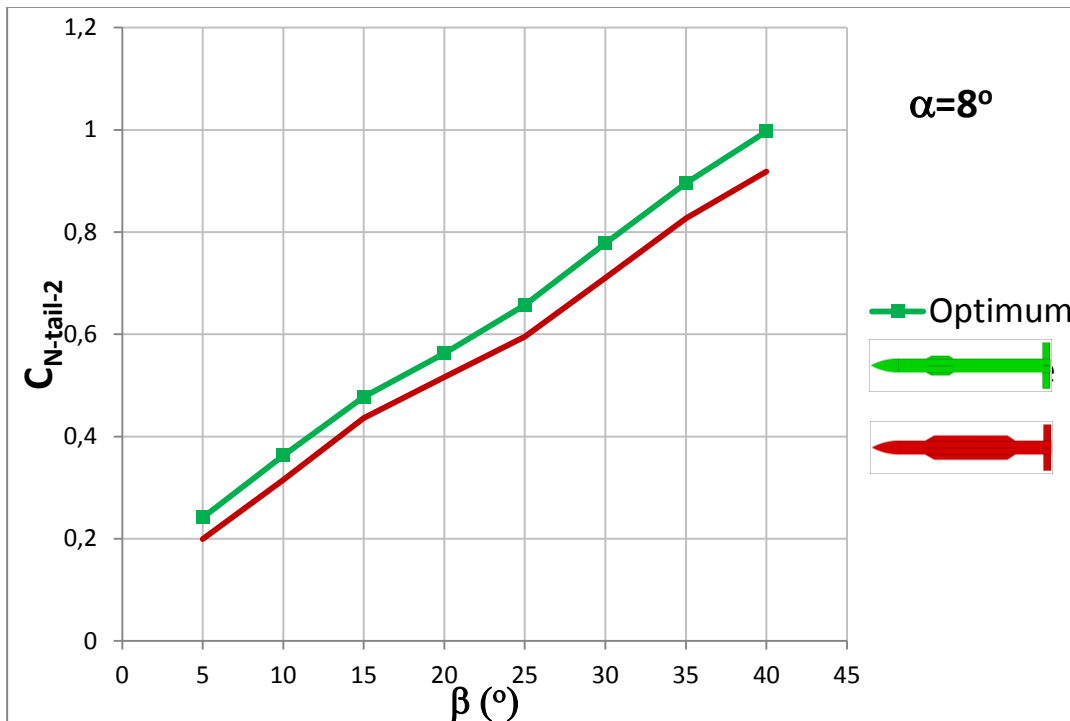


Figure 3.38 The change of the panel normal force of the tail with sideslip angle for the optimum and baseline missile configurations (Mach=2.01)

The performance parameters are compared in figures Figure 3.35-Figure 3.38. The change of the pitching moment coefficient with sideslip angle for optimum configuration is significantly reduced compared to the baseline configuration. Static margin is successfully kept in the range of 1-1.2. Moreover, change of the normal force coefficient with sideslip angle is also positively affected as seen in Figure 3.36, even though it is not a design parameter of the optimization problem. Here it must also be noted that normal force coefficient of the optimum configuration remains nearly constant for high sideslip angles, but baseline configuration fluctuates, firstly increases and then decreases. It can be said that the small strakes do not cause asymmetric effects for high sideslip angles; however, the larger strakes induce larger asymmetric vortices and thus more cross coupling effects.

The pressure distributions of the entire missile are shown for baseline and optimum configurations in Figure 3.39 and Figure 3.41, respectively.

As can be seen from the figures, the symmetry line in the distinction region of the blue and green is longer in the case of the optimum configuration, however, it is smaller for the baseline configuration. In other words, the asymmetric flow developed due to the long strakes create greater cross coupling effects in the pitching plane due to the asymmetry induced from sideslip angle. Moreover, the pressure on the tail surfaces of the optimum configuration is a little bit higher and spread over the tail surfaces due to clear flow over the panels, thus possibly increasing the control effectiveness of the tail surfaces. This effect can also be derived from Figure 3.38, as the panel normal force is higher for the optimum configuration. However, due to increased local angle of attack in tail surfaces of the optimum configuration, the stall for tail panels begin at smaller angles of attack in optimum configuration compared to the baseline configuration. Therefore, the early stall of tail panels may be prevented by placing long strake surfaces close to the tail surfaces, which adversely affects the objective.

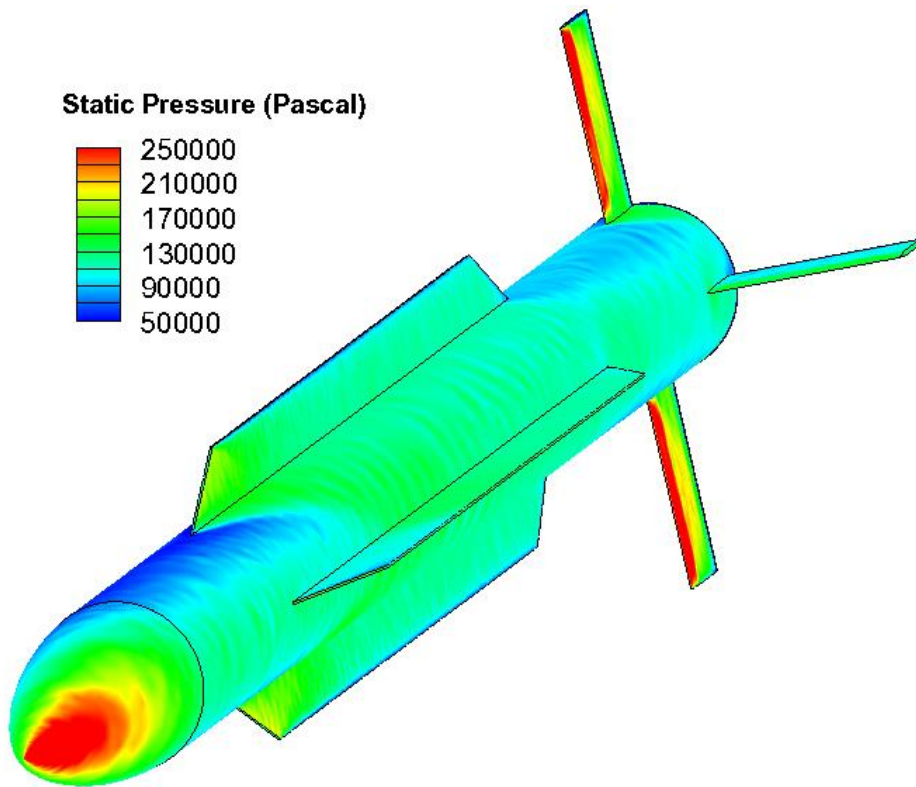


Figure 3.39 The pressure distribution over the baseline missile configuration at Mach 2.01, angle of attack 8° , sideslip angle 10° (45° rotated view)

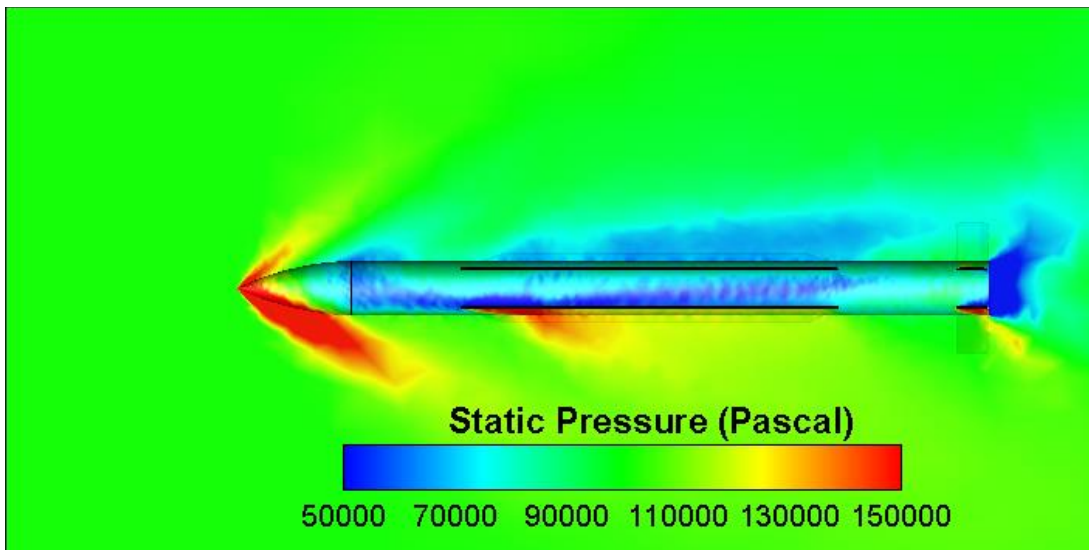


Figure 3.40 The pressure distribution over the baseline missile configuration at Mach 2.01, angle of attack 8° , sideslip angle 10° (side view)

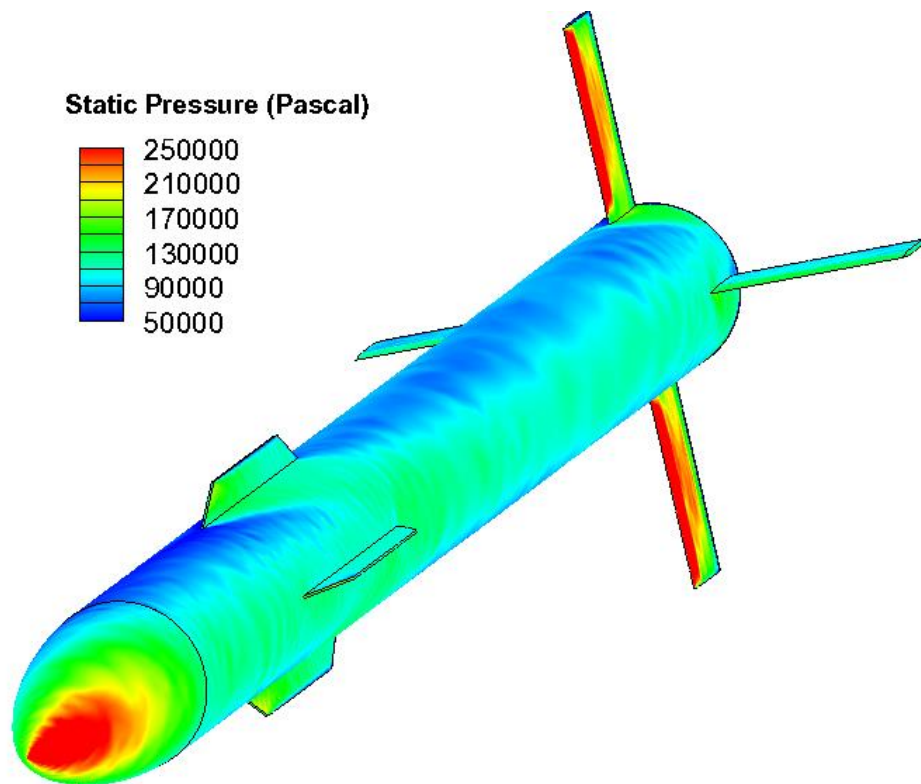


Figure 3.41 The pressure distribution over the optimum missile configuration at Mach 2.01, angle of attack 8° , sideslip angle 10° (45° rotated view)

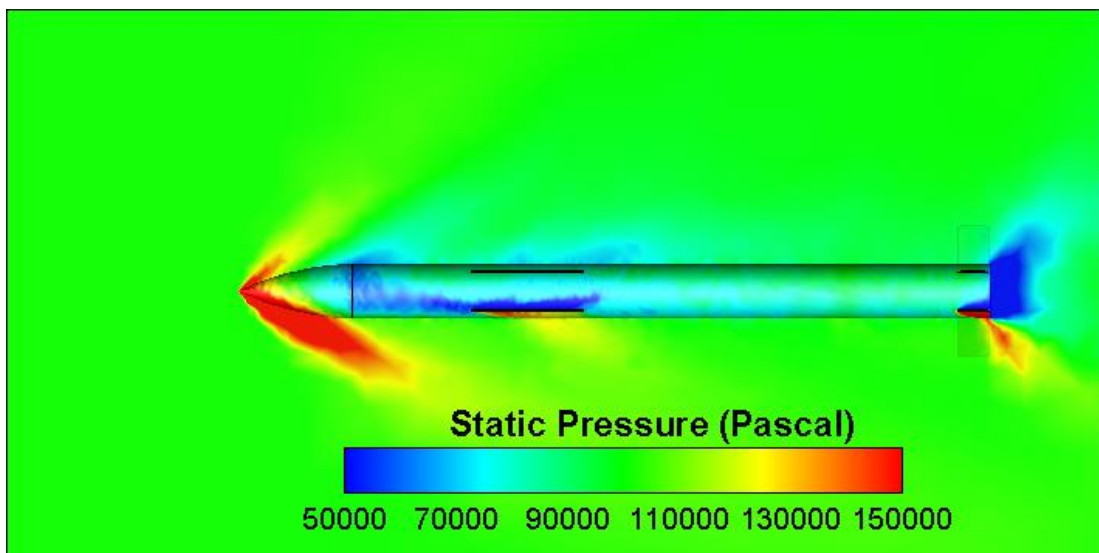


Figure 3.42 The pressure distribution over the optimum missile configuration at Mach 2.01, angle of attack 8° , sideslip angle 10° (side view)

Looking at the pressure distribution over the whole configuration, for the optimum configuration the smaller strakes affect the pressure of the local region only, not disturbing the flow field over the tail surfaces. However, for the baseline configuration larger region of the flow field is disturbed, triggering more vortices and thus asymmetric flow distribution. The vortices shed along the strake panels can be observed in Figure 3.40 and Figure 3.42. As it can be observed the larger panel surfaces induce longer vortices with increasing region of influence in the flow field. Although the larger strake fins cause the fin normal force decrease at the tail surfaces, this affect might be beneficial in terms of reducing effective angle of attack, decaying the stall of the tail fins.

In the figures below, Mach number contours around the optimum and baseline missiles are shown, as seen the flow attaches the surfaces of the long strake fins of the baseline configuration.

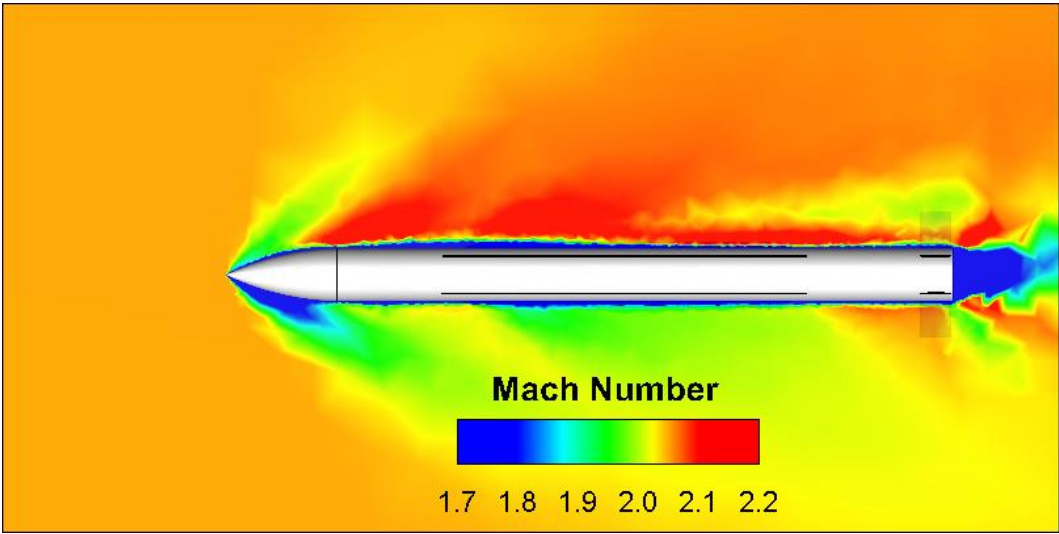


Figure 3.43 The Mach Number Contour Around the Baseline Missile Configuration at Mach 2.01, angle of attack 8° , sideslip angle 10° (side view)

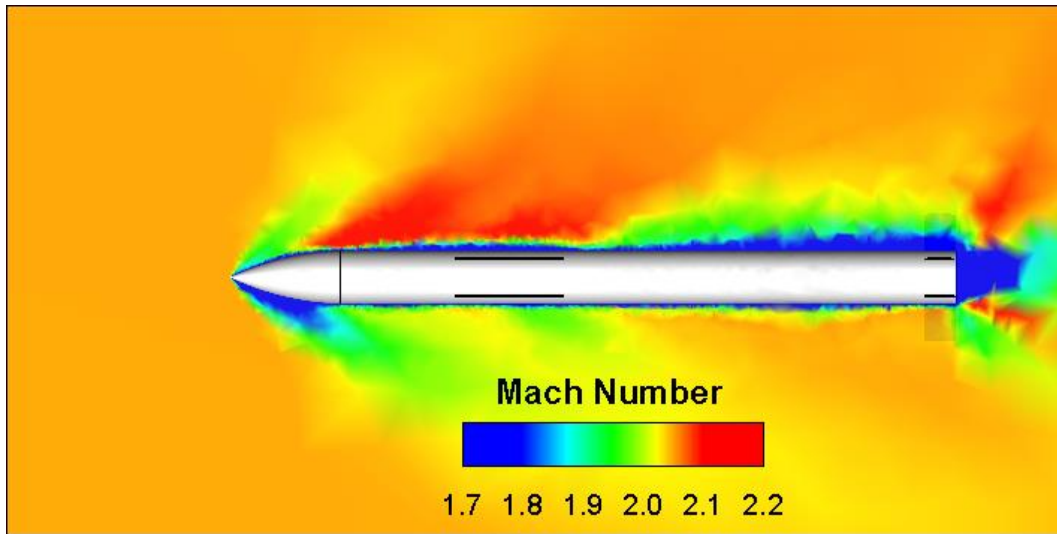


Figure 3.44 The Mach Number Contour Around the Optimum Missile Configuration at Mach 2.01, angle of attack 8° , sideslip angle 10° (side view)

Along the chord of the strake on the body, the slices were taken for both optimum and baseline configurations. The velocity vector plots at intermediate slices along the x axis are shown in the below figures. It can be observed that the vortices start to develop at the leading edge of the strake panels and moving a little bit along the x axis, in the front part of the strake unit two concentrated vortices develop. Moving further along the x axis for the baseline configuration, only a single concentrated vortex is formed. On the other hand since the chord length of the strake of the optimum configuration is shorter than the baseline, the chord finishes before the vortices are transformed into single concentrated vortex.

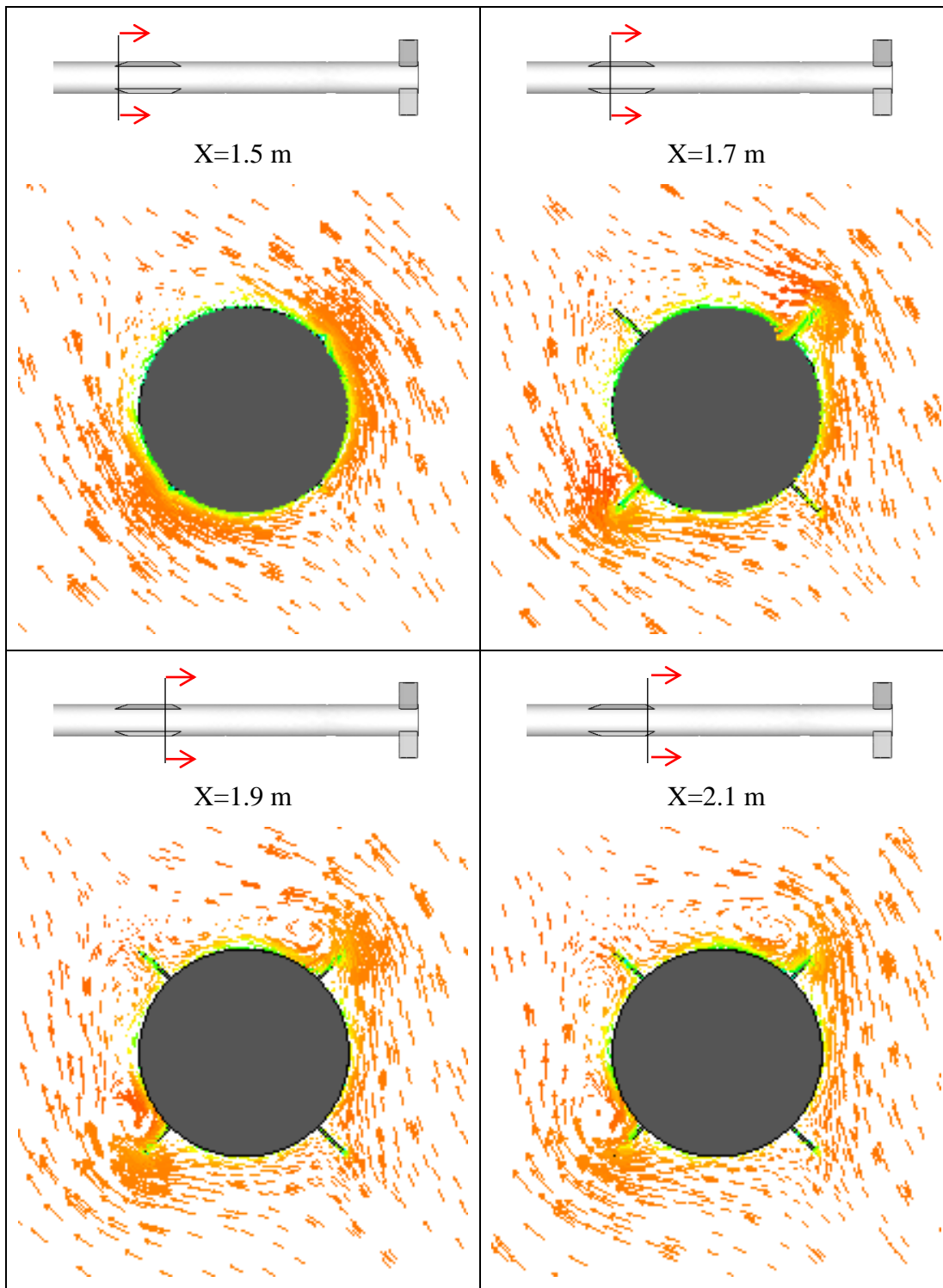


Figure 3.45 The velocity vector plots on slices along the x-axis of the optimum configuration at Mach 2.01, angle of attack 8° , sideslip angle 10°

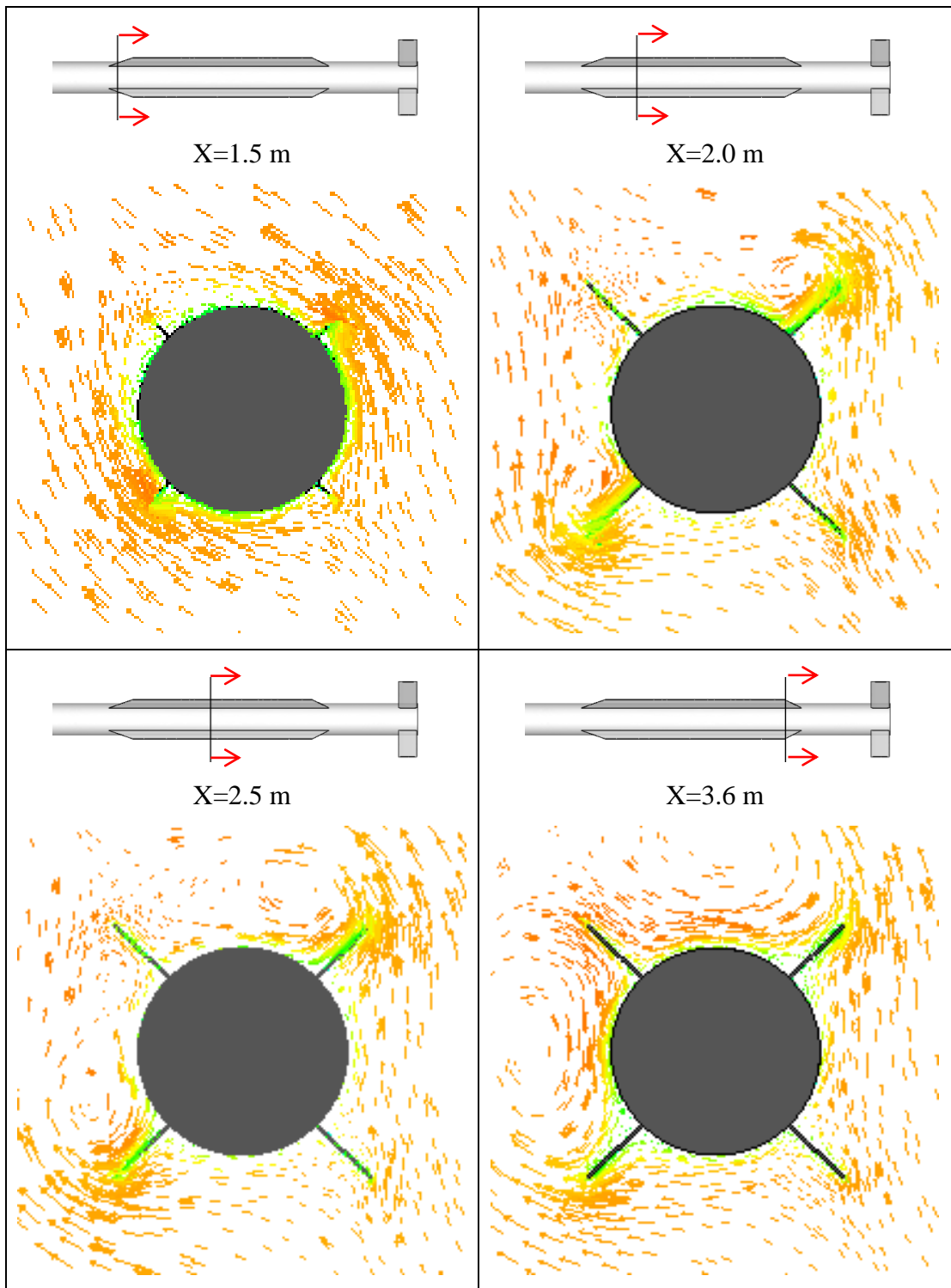


Figure 3.46 The velocity vector plots on slices along the x-axis of the baseline configuration at Mach 2.01, angle of attack 8° , sideslip angle 10°

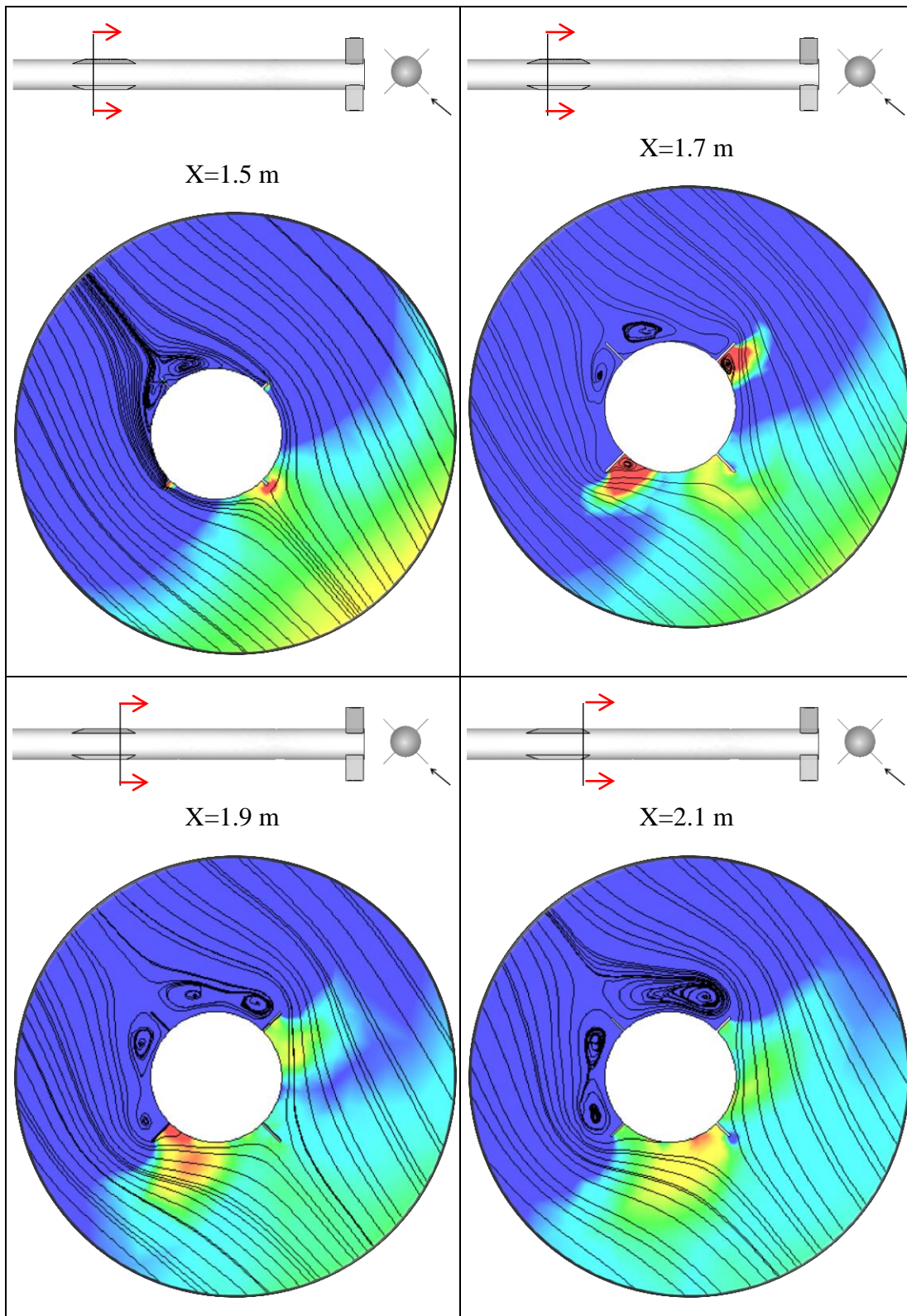


Figure 3.47 The pressure contours and streamlines on slices along the x-axis of the optimum configuration at Mach 2.01, angle of attack 8° , sideslip angle 10°

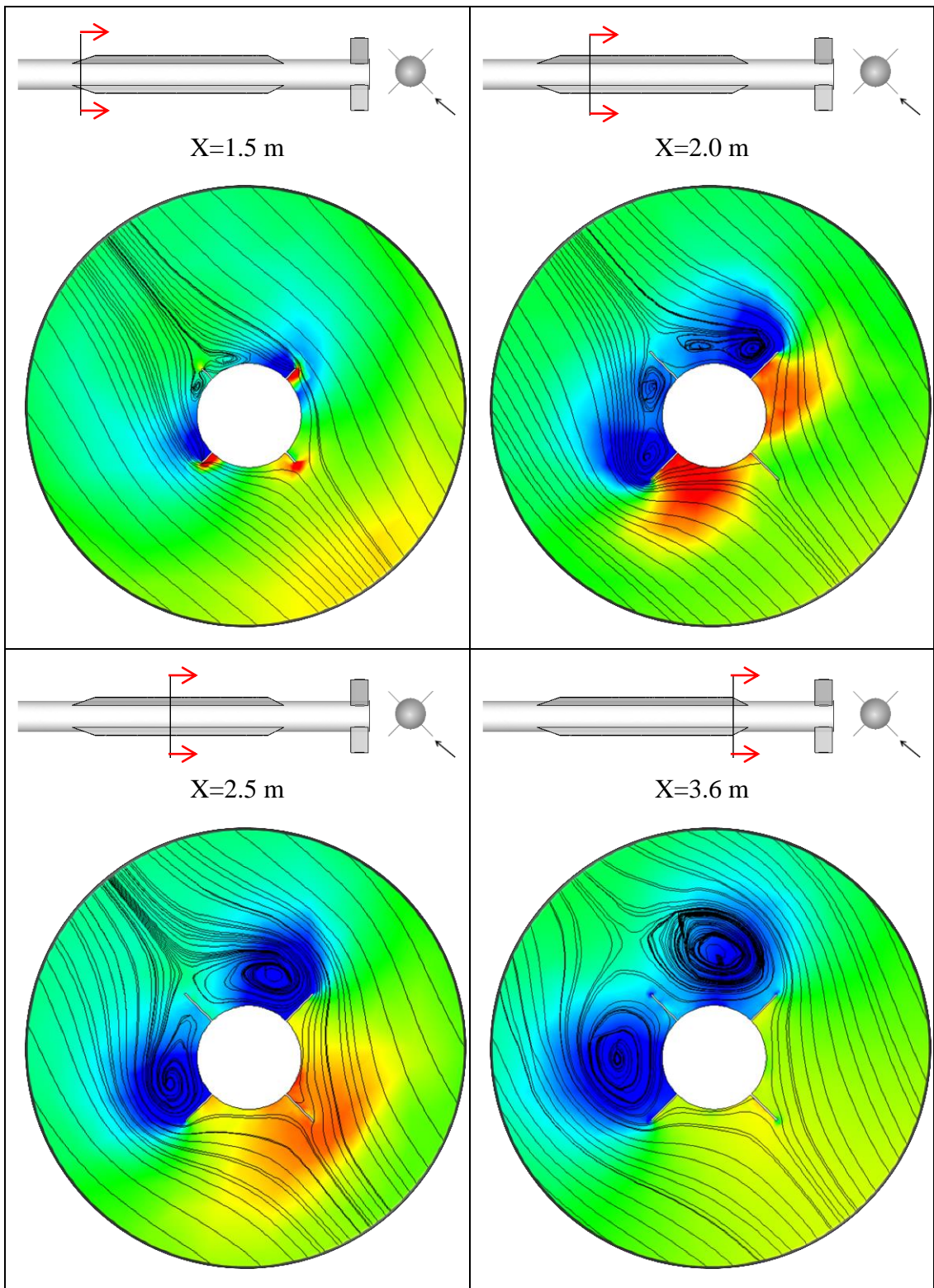


Figure 3.48 The pressure contours and streamlines on slices along the x-axis of the baseline configuration at Mach 2.01, angle of attack 8° , sideslip angle 10°

For long strake structure, body vortices are shed initially, and later a secondary vortex is shed starting at the strake leading edge. Moving further, strake and body vortices combine into a single concentrated vortex. Since the optimum configuration has short strakes, the chord ends before two vortices at cross section are combined into a single concentrated vortex. The vortex structure observed in this part combines into single concentrated vortex, which is similar to the previous studies for body and strake configurations [20].

3.2.6 Comparison of the Optimum and a Classical Configuration

A classical configuration with same planform area but with higher aspect ratio is selected for comparison with our very low aspect ratio optimum configuration. The performance parameters of two configurations are compared. It is found that the low aspect ratio configuration has lower axial force compared to the conventional aspect ratio configuration. The change of the static margin is tremendous for classical one compared to the low aspect ratio one.

The coast phase axial force coefficients of the configurations are compared in Figure 3.50. The optimum configuration has lower axial force coefficient compared to classical wing configuration.

The rolling moment for the optimum strake configuration is lower than that of the classical configuration as expected due to lower moment arm, as shown in Figure 3.51. The rolling moments are close only in the region corresponding to the orientation at sideslip of small moment arm.

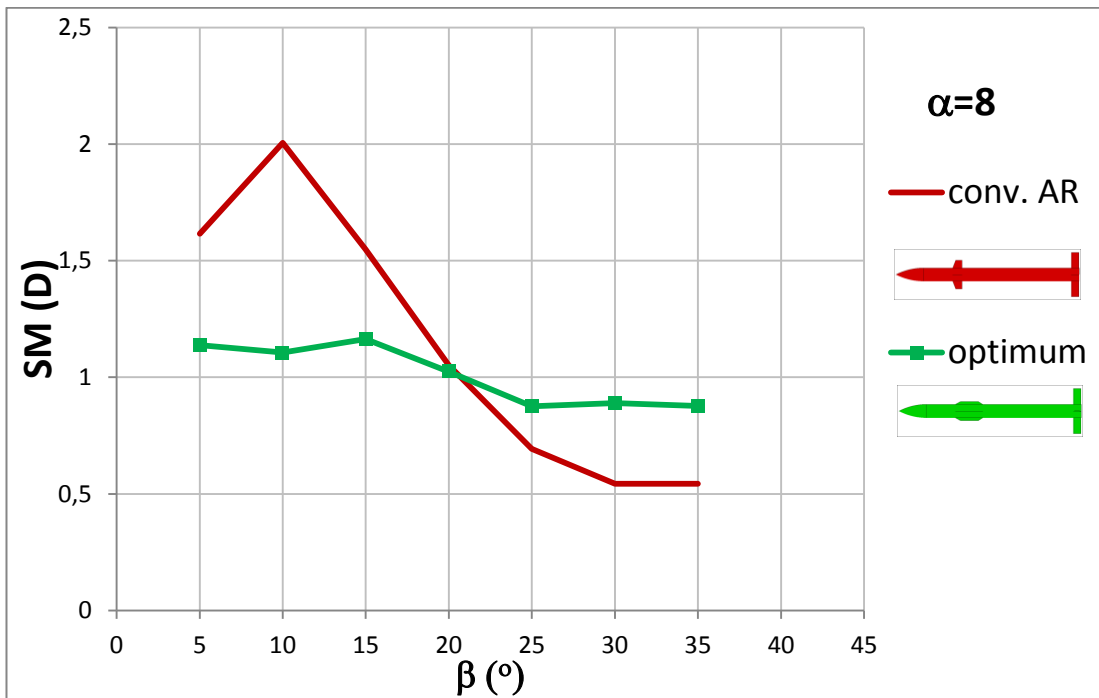


Figure 3.49 The change of the static margin with sideslip angle for the optimum and conventional missile configurations having same planform area (Mach=2.01)

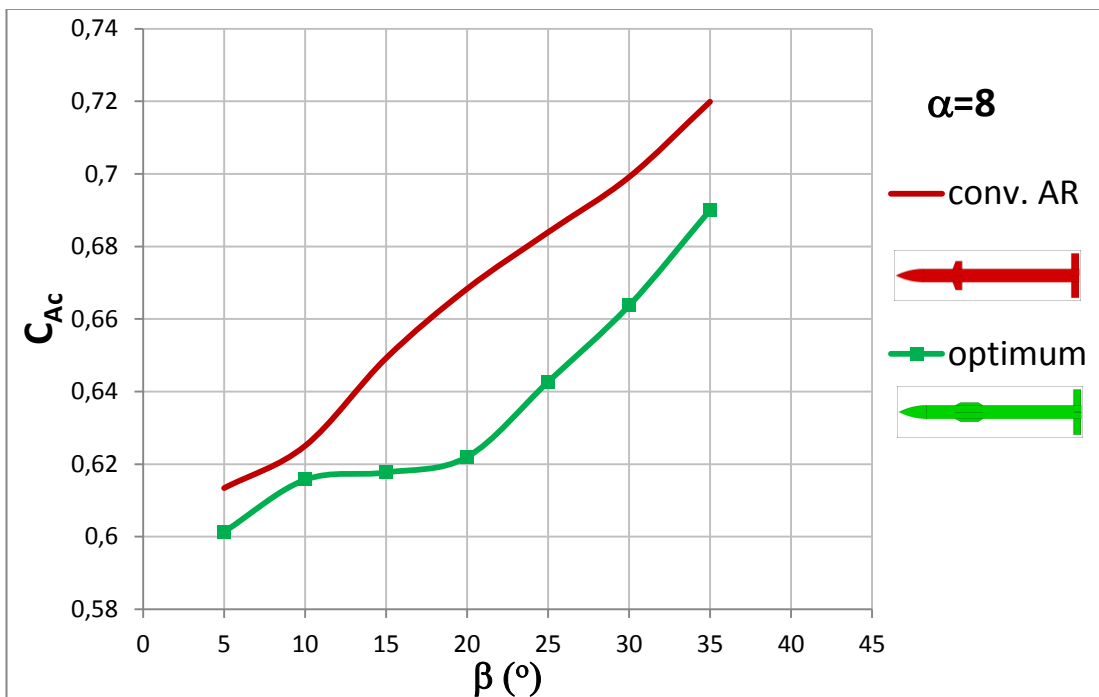


Figure 3.50 The change of the axial force coefficient with sideslip angle for the optimum and conventional missile configurations having same planform area (Mach=2.01)

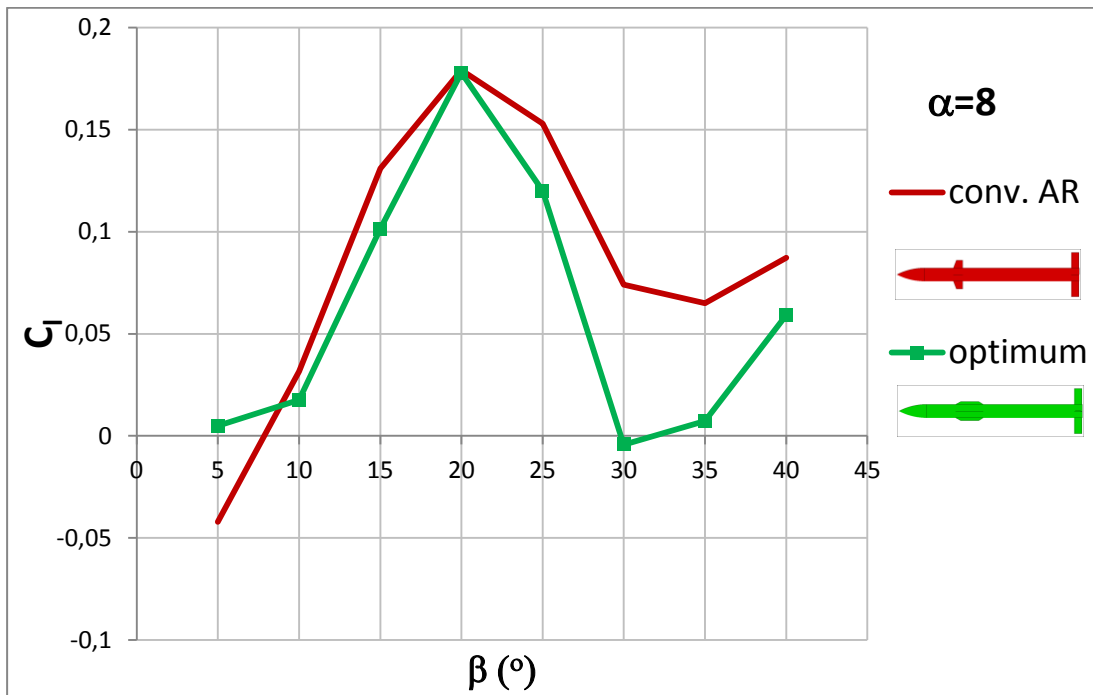


Figure 3.51 The change of the rolling moment coefficient with sideslip angle for the optimum and conventional missile configurations having same planform area (Mach=2.01)

CHAPTER 4

CONCLUSION

In this thesis, computational methods and fast prediction methods were used to predict normal force and center of pressure of a missile with very low aspect ratio fin configuration. A case study was selected for comparative analysis and optimization study. Computational Fluid Dynamics (CFD) results for the case study were compared with empirical and theoretical methods at supersonic Mach numbers. The theoretical methods consisted of MISSILE DATCOM and White's experimental method. The normal force and calculated center of pressure values of the strake unit (D57) were compared with data from LTV HSWT 655 Wind Tunnel Test Data [2]. Strake panel alone and body alone forces together with total forces acting on the body-strake model were used to calculate the aerodynamic interference by CFD analysis. The pressure fields of the body alone and body-strake configurations were compared. The CFD results were found to be robust and consistent with the experimental results. Furthermore, for theoretical methods employed in this study, further research is required. After validating CFD tool, with the addition of fixed tail surfaces on the body, a CFD based optimization study was performed to minimize the incremental change in the pitching moment due to increase in the sideslip angle while keeping static margin in a particular range.

The PSO method and the gradient based optimization method were employed to reduce pitching moment increment due to increase in the sideslip angle. Initially, a design algorithm was developed by using Particle Swarm Optimization method. In this algorithm, the strake planform geometry is changed while body and tail geometry are kept constant. The aerodynamic design parameters were evaluated by

performing CFD solutions for configurations traced by the optimization algorithm. Meanwhile, automatic meshing scheme was developed for the varying strake geometry. In parallel to PSO study, gradient based optimization was also performed. However, gradient solution was trapped in the local optima. Although pitch-yaw coupling was reduced into a small extent, gradient optimization could not find the global solution of the problem. In fact, gradient solution very quickly was able to detect the span effect, but it missed the effect of other parameters. Eventually, it is seen that PSO succeeds in finding global solution.

By the end of the PSO design, coupling of the pitching moment coefficient on the sideslip was significantly reduced while the static margin was kept in the desired range. Also variation of static margin was diminished. Since the coupling of the longitudinal plane on yaw angle was reduced, the balanced maneuverability capability was increased and a good input for the linear autopilot design is prepared. Moreover, as stated above, the gradient solution was trapped in the local solution proving the necessity of the PSO method. For the objective function definition in this study, a short span and short chord fin was obtained by the PSO optimization study. There was a significant decrease in the pitching moment coupling to sideslip angle. However, undesirably load factor was decreased about %40 to that of the starting point.

The goal of the optimization in this thesis was merely reducing the coupling effect of yaw angle on the pitching moment. Therefore, any other design parameters were not included except static margin which was used as a controlling parameter. Actually, if this was a complete missile design problem representing a highly maneuverable missile, large load factor values would be needed. If a large load factor was included as a design parameter, longer chord structures would be expected.

The CFD based optimization tool developed in this study has the capability to take care of different design problems, and could be applied to the problems that engineering level codes are inferior. Only with small modifications in the automatic meshing scheme, grid generation and case preparation can be automated for different missile configurations. This optimization tool can also be further extended to include

other geometrical parameters such as the sweep angle at leading edge and fin thicknesses. In addition, the tail design can also be performed at the same time with the strake design. Moreover, different objective functions based on a variety of aerodynamic performance parameters can be defined for achieving different goals.

REFERENCES

- [1] L. H. Jorgensen and E. D. Katzen, "Aerodynamics of Missiles Employing Wings of Very Low Aspect Ratio," NASA Ames Research Center, United States, Mar 05, 1956.
- [2] J. T. White, "A Method for Predicting Combined Dorsal Normal Force and Center-of-Pressure Location at Supersonic Mach Numbers," in *19th Atmospheric Flight Mechanics Conference*, Scottsdale,AZ, 1994.
- [3] S. Tuling, "An engineering method for modeling the interaction of circular bodies and very low aspect ratio cruciform wings at supersonic speeds," PhD Thesis, University of the West of England, 2013.
- [4] "Global Security Website," [Online]. Available: <http://www.globalsecurity.org/space/systems/images/sm3-Image104.jpg>. [Accessed 27 10 2015].
- [5] "MBDA Missile Systems," [Online]. Available: http://www.mbdasystems.com/mediagallery/photos/MICA-IR-RAFALE-2_zoom.jpg. [Accessed 27 10 2015].
- [6] "Air Force Technology," [Online]. Available: <http://www.airforce-technology.com/projects/10419/images/239521/large/11-image.jpg>. [Accessed 27 10 2015].
- [7] "Diehl Defense Website," [Online]. Available: http://www.diehl.com/uploads/pics/IRIST_SL_02.png. [Accessed 27 10 2015].
- [8] "Sea Forces Online, Naval Information," [Online]. Available:

- <http://www.seaforces.org/wpnsys/SURFACE/RIM-162-Evolved-Sea-Sparrow-Missile-Dateien/image013.jpg>. [Accessed 27 10 2015].
- [9] "Federation of American Scientists Website," [Online]. Available: <http://fas.org/man/dod-101/sys/missile/agm-78.htm>. [Accessed 27 10 2015].
- [10] K. Arslan, "Aerodynamic Optimization of Missile External Configurations," Master's Thesis, Middle East Technical University, Ankara, 2014.
- [11] E. Fleeman, Tactical Missile Design, Virginia: AIAA education series:American Institute of Aeronautics and Astronautics, 2001.
- [12] M. J. Hemsch, Tactical Missile Aerodynamics : "General Topics", Virginia: AIAA Progress in Astronautics and Aeronautics, vol. 141, May. 1991.
- [13] S. S. Chin, Missile Configuration Design, Orlando: McGraw Hill Publishing Company, 1961.
- [14] C. C. Yuan and R. M. Howard, "Effect of Forebody Strakes on Missile Asymmetric Vortices," *Journal of Aircraft*, vol. Vol. 28, no. No:4, pp. 844-846, 1991.
- [15] H. J. Allen and E. W. Perkins, "A Study of Effects of Viscosity on Flow over Slender Inclined Bodies of Revolution," NACA Technical Report 1048., 1951.
- [16] J. Nielsen, Missile Aerodynamics, New York : McGraw-Hill, 1960.
- [17] C. Rosema, J. Doyle, L. Auman and M. Underwood, "MISSILE DATCOM User's Manual - 2011 Revision," AIR FORCE RESEARCH LABORATORY , March 2011.
- [18] M. J. Hemsch and J. N. Nielsen, "Equivalent angle-of-attack method for estimating nonlinear aerodynamics of missile fins," *Journal of Spacecraft and*

Rockets, vol. Vol. 20, no. No. 4, 1983.

- [19] O. Göker, M. Akgül, H. Y. Akargün and A. Akgül, "“NASA Dual Control Missile” İçin Aerodinamik Kestirim Çalışmaları," in *4. Ulusal Havacılık ve Uzay Konferansı*, İstanbul, 2012.
- [20] A. Sigal, "Aerodynamic Analysis of Body-Strake Configurations," US Air Force Research Laboratory European Office for Aeronautical Research and Development, Technion, 2006.
- [21] A. Sigal and W. B. Blake, "Comparative Aerodynamic Analysis of Body-Strake Configurations," in *28th AIAA Applied Aerodynamics Conference*, Chicago, 2010.
- [22] G. M. Simpson and J. T. Birch, "Some Aerodynamic Characteristics of very Low Aspect Ratio Wings," in *19th AIAA Applied Aerodynamics Conference*, Bedford, 2001.
- [23] A. Akgül and H. Tiftikçi, "Hesaplamalı Akışkanlar Dinamiği İle Aerodinamik Tasarım Eniyilemesi," in *2. Ulusal Havacılık ve Uzay Konferansı*, İstanbul, 2008.
- [24] A. Akgül, H. Y. Akargün, B. Atak, A. E. Çetiner and O. Göker, "Aerodynamic Predictions For NASA Dual Control Missile And Comparison With Experiment," in *OTEH 2011 On Defensive Technologies*, Belgrad, 2011.
- [25] "ANSYS FLUENT 12 Theory Guide," Fluent Inc., 2009.
- [26] J. Blazek, *Computational Fluid Dynamics: Principles and Applications*, Elsevier Science, 2005.
- [27] A. Bakker, "Turbulence Models," 2002.

- [28] E. Lucero, "Empirical Curves for Predicting Supersonic Aerodynamics of Very Low Aspect Ratio Lifting Surfaces," in *Journal of Spacecraft and Rockets*, Maryland, 1984.
- [29] C. Rosema and D. J. B., "Fin-Shed Vortex Modeling within Missile Datcom," in *49th AIAA Aerospace Sciences Meeting including the New Horizons Forum and Aerospace Exposition*, Orlando, 2011.
- [30] M. A. Khanesar, T. Hassan, T. Mohammad and M. A. Shoorehdeli, "Novel Binary Particle Swarm Optimization," 2009.
- [31] C. W. Reynolds, "Flocks, Herds, and Schools: A Distributed Behavioral Model presented by Duc Nguyen," 2007.
- [32] C. Rosema and M. Underwood, "Recent Fin Related Improvements for Missile DATCOM," in *25th AIAA Applied Aerodynamics Conference*, Miami, 2007.

APPENDIX A

GRADIENT OPTIMIZATION CALCULATIONS

Details of the gradient calculation during steepest descent optimization can be found in the tables below.

Table A.1 The Gradient Vector Calculation for Iteration 1 of the Optimization

OPTIMIZATION ITERATION 1							
Geo	XLE	CHORD	SPAN	ΔC_m	SM	OBJ	(-)GRAD
G0	135	260	10	7.16478	0.81434	59.4942	
Δ_1	139	260	10	7.28307	0.87514	58.0993	0.007913
Δ_2	131	260	10	7.09001	0.75945	61.8656	
Δ_3	135	264	10	7.23498	0.84596	58.7985	0.006183
Δ_4	135	256	10	7.26165	0.79984	61.7411	
Δ_5	135	260	10.5	7.29151	0.78475	63.1043	-0.12789
Δ_6	135	260	9.5	7.02198	0.85126	55.4953	

At the second step span length is fixed and optimization is continued with two variables since span gets out of limits.

Table A.2 The Gradient Vector Calculation for Iteration 2 of the Optimization

OPTIMIZATION ITERATION 2							
Geo	XLE	CHORD	SPAN	ΔC_m	SM	OBJ	(-)GRAD
G0	135.23	260.185	6.16	5.352	1.147	28.6439	
Δ_1	139.23	260.185	6.16	5.313	1.186	28.2279	0.003596
Δ_2	131.23	260.185	6.16	5.39	1.109	29.0521	
Δ_3	135.23	270.185	6.16	5.423	1.163	29.4089	-0.00276
Δ_4	135.23	250.185	6.16	5.275	1.134	27.8256	

At step two, only small changes occur in remaining two parameters as seen in the above figures.

After step two continuing the gradient search with iteration 3, again the span is taken as an optimization parameter. At this step, all three parameters are taken as input to optimization problem like at the beginning.

Table A.3 The Gradient Vector Calculation for Iteration 3 of Optimization

OPTIMIZATION ITERATION 3							
Geo	XLE	CHORD	SPAN	$ \Delta C_m $	SM	OBJ	(-)GRAD
G0	139.41	256.97	6.16	5.288	1.183	27.9629	
Δ_1	143.41	256.97	6.16	5.25	1.221	29.0266	-0.00295
Δ_2	135.41	256.97	6.16	5.326	1.145	28.3662	
Δ_3	139.41	266.97	6.16	5.359	1.199	28.7188	-0.00282
Δ_4	139.41	246.97	6.16	5.21	1.169	27.1441	
Δ_5	139.41	256.97	10.16	6.741	1.026	45.4410	-0.12817
Δ_6	139.41	256.97	2.16	3.016	1.377	16.7691	

The gradient of the objective function in span direction is too large compared to that of the other parameters. Therefore a step in gradient direction makes span negative therefore we again elect the span from the optimization parameters, leaving chord and leading edge location.

Table A.4 The Gradient Vector Calculation for Iteration 4 of the Optimization

OPTIMIZATION ITERATION 4							
Geo	XLE	CHORD	SPAN	$ \Delta C_m $	SM	OBJ	(-)GRAD
G0	139.41	256.97	6.16	5.288	1.183	27.9629	
Δ_1	143.41	256.97	6.16	5.25	1.221	29.0266	-0.00295
Δ_2	135.41	256.97	6.16	5.326	1.145	28.3662	
Δ_3	139.41	266.97	6.16	5.359	1.199	28.7188	-0.00282
Δ_4	139.41	246.97	6.16	5.21	1.169	27.1441	

APPENDIX B

THE PSO OPTIMIZATION STUDY BY USING MISSILE DATCOM

The PSO optimization study in Chapter 3 was performed by using CFD to evaluate aerodynamic coefficients. In this part, the optimization study by PSO is performed by using the Missile DATCOM 2009 to evaluate aerodynamic coefficients. The results obtained by using Missile DATCOM 2009 inside Particle Swarm Optimization code are compared with the previous results which were obtained by using CFD inside the optimization code.

The change of the objective function during iterations is shown in the figure.

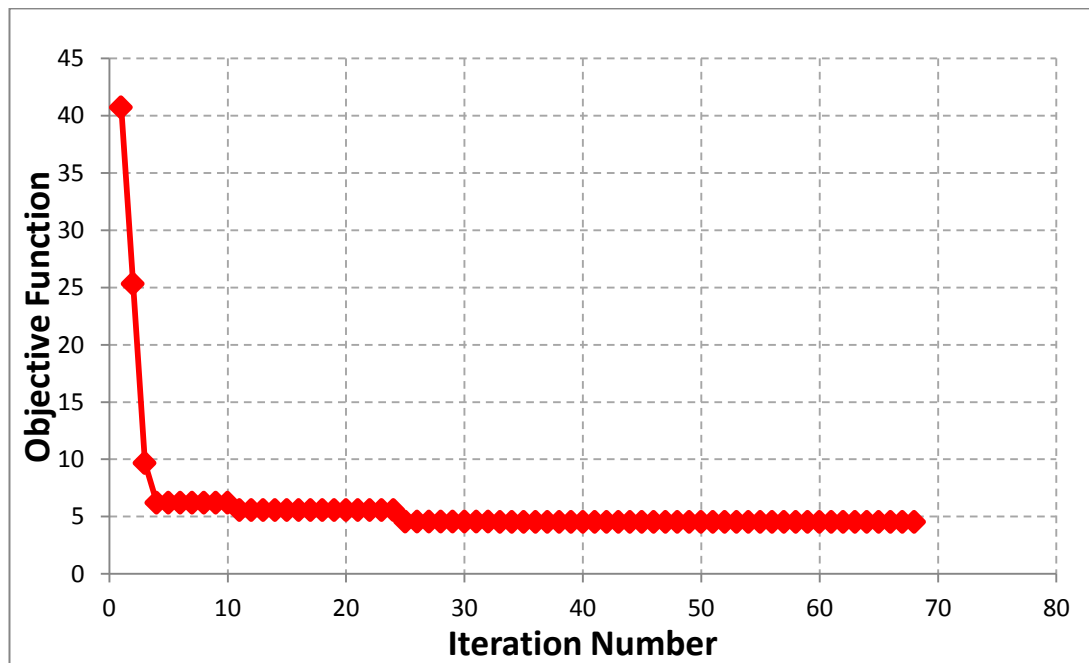
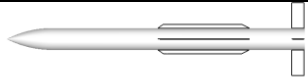
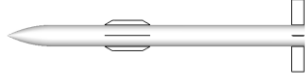


Figure B.1 The change of the objective function during DATCOM PSO iterations

The change of the objective function during PSO iterations is shown in the above figure. The change of the geometrical parameters during optimization iterations are given in the Figures Figure B.2 through Figure B.4. The comparison of the optimum

geometry obtained by CFD inside PSO code and Missile DATCOM 2009 inside PSO code is shown below:

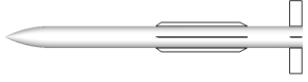
Table B.1 The comparison of the geometric parameters of the optimum configurations obtained by PSO using CFD and PSO using Missile DATCOM 2009

Aerodynamic Tool inside PSO	Chord Length (cm)	Span Length (cm)	Leading Edge Location (cm)	Optimum Geometry Plot (45° rotated)
DATCOM	239.76	6.00	144.8	 <p>MDBEST</p>
CFD	70.86	6.73	146.37	 <p>CBEST</p>

The optimum geometry obtained by the PSO code using Missile DATCOM to evaluate aerodynamic coefficients is given name “MDBEST”, and the optimum geometry obtained in Chapter 3 by the PSO code using CFD to evaluate aerodynamic coefficients is named as “CBEST” for simplification.

The CFD solution was also performed for the MDBEST configuration. The CFD results obtained for MDBEST configuration are compared with Missile DATCOM 2009 results in the table below.

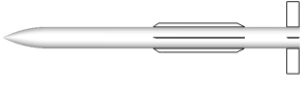
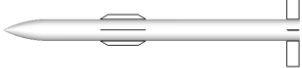
Table B.2 The comparison of the aerodynamic parameters obtained by CFD and Missile DATCOM 2009 for the MDBEST configuration

Configuration	Aerodynamic Tool	ΔCM_{β}	Static Margin [d]	Geometry Plot (45° rotated)
MDBEST	CFD	7.48	1.76	
MDBEST	DATCOM	2.12	1.2	

As seen in Figure B.2 there is a large difference between the Missile DATCOM 2009 results and CFD results.

The aerodynamic parameters calculated by using CFD results for the MDBEST and CBEST configurations are given in the table below:

Table B.3 The comparison of the aerodynamic parameters of the MDBEST and CBEST configurations by CFD analysis

Configuration	Aerodynamic Tool	ΔCM_{β}	Static Margin [d]	Geometry Plot (45° rotated)
MDBEST	CFD	7.48	1.76	
CBEST	CFD	2.57	1.13	

According to the CFD results, the MDBEST configuration is a misleading solution for our objective function presented in Chapter 3.

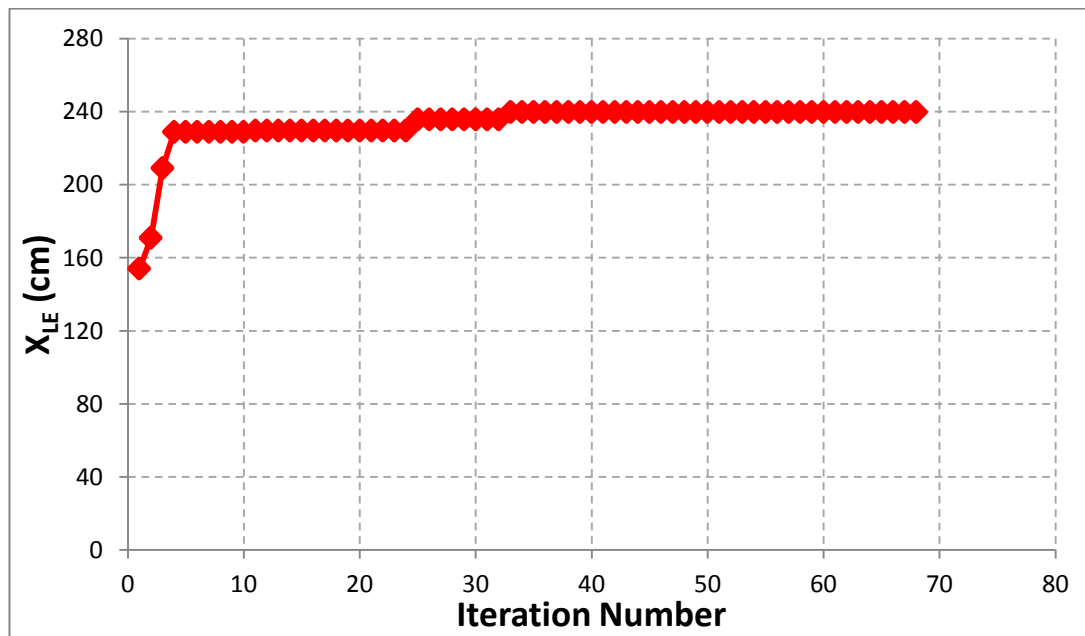


Figure B.2 Variation of the leading edge location of the strake during DATCOM inside PSO iterations

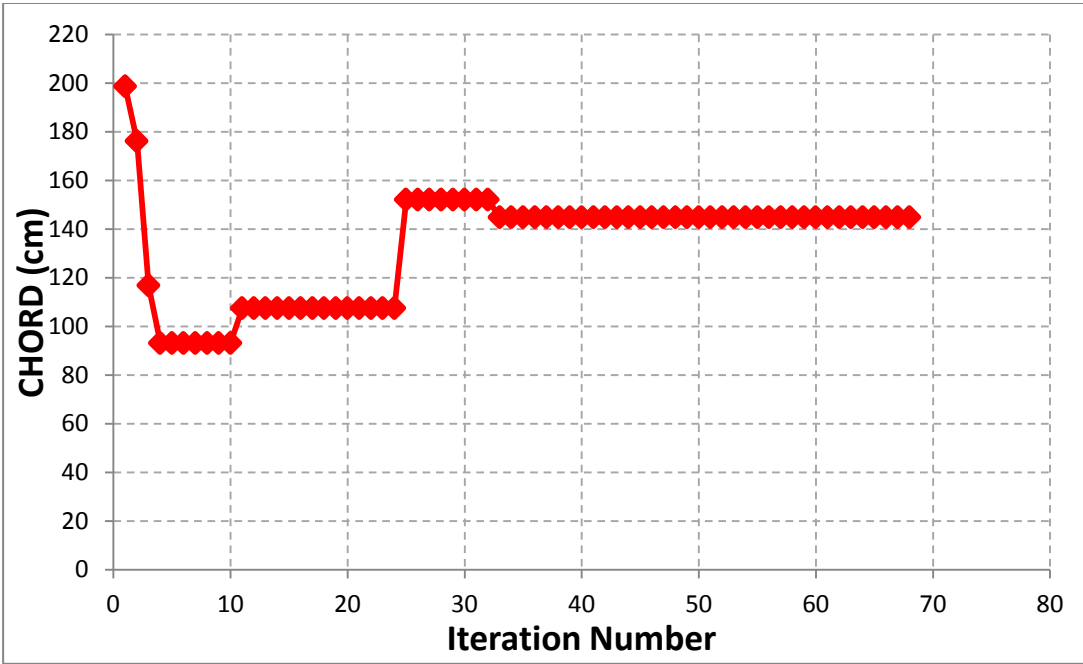


Figure B.3 Variation of the chord length of the strake during DATCOM inside PSO iterations

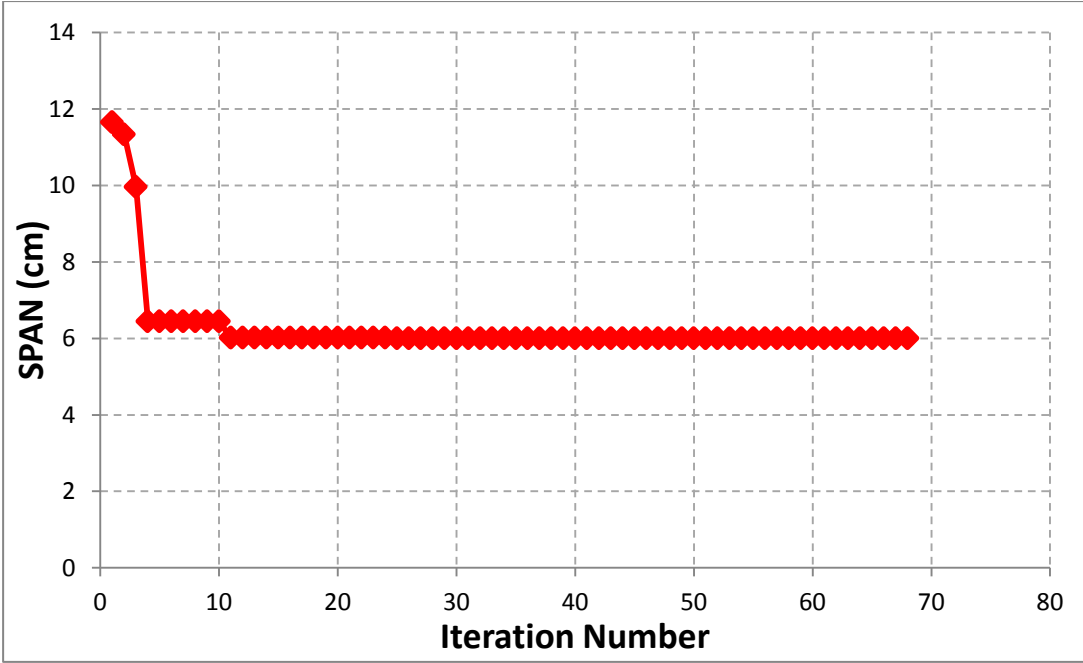


Figure B.4 Variation of the span length of the strake during DATCOM inside PSO iterations